NONDESTRUCTIVE EVALUATION OF AN ENVIRONMENTALLY FRIENDLY CONVERSION COATING FOR MAGNESIUM ALLOYS USING OPTICAL MEASUREMENT TECHNIQUES

A Thesis

by

DAVID ZUNIGA

Submitted to the Office of Graduate Studies of
Texas A&M University
in partial fulfillment of the requirements for the degree of

MASTER OF SCIENCE

August 2006

Major Subject: Mechanical Engineering

NONDESTRUCTIVE EVALUATION OF AN ENVIRONMENTALLY FRIENDLY CONVERSION COATING FOR MAGNESIUM ALLOYS USING OPTICAL MEASUREMENT TECHNIQUES

A Thesis

by

DAVID ZUNIGA

Submitted to the Office of Graduate Studies of
Texas A&M University
in partial fulfillment of the requirements for the degree of

MASTER OF SCIENCE

Approved by:

Chair of Committee,	Richard B. Griffin
Committee Members,	Andreas Holzenburg
	Won-jong Kim
Head of Department,	Dennis O'Neal

August 2006

Major Subject: Mechanical Engineering

ABSTRACT

Nondestructive Evaluation of an Environmentally Friendly Conversion Coating for Magnesium Alloys Using Optical Measurement Techniques. (August 2006)

David Zuniga, B.S., Texas A&M University

Chair of Advisory Committee: Dr. Richard B. Griffin

Magnesium alloys have one of the highest specific strengths of all construction metals used. Specifically, magnesium alloy castings are used in the aerospace industry to reduce the weight of aerospace vehicles. Coating systems must be employed to prevent corrosion of these magnesium alloys as they are also the most corrosion prone construction metals. The use of chromium is employed for the conversion coating which forms the foundation of many of these coating systems. In an effort to phase these harmful chromates out of the coating system and continue to use magnesium alloys, an environmentally friendly conversion coating has been developed. This paper explores the best types of methods used to evaluate the thickness and coating coverage of the environmentally friendly conversion coating. Destructive and nondestructive techniques are developed to examine the thickness and surface coverage of this environmentally friendly coating. Specifically an eddy current measurement technique, light, confocal, scanning electron and transmission electron microscopy techniques are used to determine the coating thickness of the environmentally friendly coating through destructive evaluation. Three nondestructive evaluation techniques, including polarized light microscopy, infrared spectroscopy (Fourier Transform and Raman) and an infrared proximity sensor are used to determine surface coverage of the environmentally friendly coating.

To my mother and father for giving me all that I ever needed to succeed,
amor vincit omnia,
and my deepest friends, Amanda and my brother, for your love and support.

ACKNOWLEDGEMENTS

A special thanks goes to my committee chair, Dr. Richard B. Griffin, for giving me a fighting chance and for not ever dismissing an obviously wrong solution too quickly. His patience and open mind have helped open my mind and imagination so that I could learn how to plot my own road map to discovery. I would like to thank my committee members Dr. Andreas Holzenburg and Dr. Won-jong Kim for their critical review and enthusiasm to help push for the best within me. Thanks must be given to my fellow researchers: Mohammad Satter for always entertaining a philosophical discussion on research, Pranay Asthana for his enthusiasm mind and Tim Pendley for always being willing to help in the machine shop.

I would like to thank the Microscopy and Imaging Center (MIC) Staff for their tremendous help with the various data I collected with their equipment. Special thanks go to Rick Littleton and Dr. Stanislav Vitha for always having time to answer my questions and providing everything I needed to continue my research.

I would like to thank the Materials Characterization Facility (MCF) for allowing me to work with a pioneering piece of equipment to provide some meaningful data to my research. Thanks to Dr. Orla Wilson for her patience, her guidance and willingness to help. Thanks to Dr. Viktor Hadjiev for his expertise and enthusiasm.

Thanks to the Mechanical Engineering staff at Texas A&M University. Thanks go to Mike Walker for helping me to learn the foundations of machining, a skill that will help me through life. Thanks to Jim Sajewski and Brian Bachmeyer for their never ending help in setting up a new experiment, giving me new ideas and providing the equipment that I desperately needed. Their help was crucial and greatly appreciated.

I would also like to thank Professor Buddy Bollfrass for his support, guidance, review of my work and his willingness to always help. Thanks go to the Academic Center for Aging Aircraft for sponsoring this project and providing avenues for me to continue my research. Much of this research was not possible without the help of Dr. William Gorman and Earl Woosley. Their willingness to share information, materials and expertise was essential in this research.

I would like to thank a few of my past teachers who provided me with the solid initial foundation for conducting this research with sound scientific principle investigation. Thank you Jerry Workman, John Barfield and Barbara Scown at Pecos High School in Pecos, Texas, for your teachings and valued support. Last but not least, thank you Dr. Anna M. Spagnuolo for your encouragement and the sound foundation you provided for the pursuit of a continued education and research.

TABLE OF CONTENTS

Page

Page

LIST OF FIGURES

Page

Page

Page

Page

Page

Page

Page

LIST OF TABLES

Page

BACKGROUND AND INTRODUCTION

Engineers and technical staff at the Corpus Christi Army Depot facility in Corpus Christi, Texas encountered several challenges regarding the H-60 helicopter when supporting an aging aircraft initiative. These challenges include, repeated corrosion of the H-60 rotor gearbox housing leading to gearboxes being classified as beyond economical repair (BER), adhering to current environmental and health regulations regarding chromate conversion coating used to prevent corrosion on the H-60 rotor gearbox housing[1] and implementing a non chromate containing conversion coating in place of the current chromate containing conversion coating for the H-60 gearbox housing.

A team at Texas A&M University, the Academic Center for Aging Aircraft (ACAA) was charged with addressing these problems. Specifically, the team provided data that would examine fatigue, fluid, adhesion, salt fog and hydrogen embrittlement resistance properties of the non chromate containing conversion coating to be employed for use with the magnesium alloy used in the design of the H-60 rotor gearbox housing, ZE41A.

H-60 Helicopter Description

Functional Environment

The H-60 helicopter platform is a platform that is used to make various helicopters such as the blackhawk, seahawk and medivac helicopters.[2] These helicopters

---

This thesis follows the styled of the Journal of Applied Physics.

are used in a variety of capacities that expose them to a variety of environments. Because the H-60 is a helicopter that was designed to be extremely mobile and functional in all regions of the world, it is most likely designed to meet the most stringent requirements outlined by MIL-STD 810F which is the latest revision of a set of environmental criteria that most aircraft must meet.[3] It outlines high and low temperatures, humidity, salt fog exposure and vibrational requirements that must be met for any design that uses this set of criteria. If the H-60 is designed to meet these requirements, Table 1 lists the specific requirements that must be met during the design phase of this aircraft.

Table 1: Selected MIL-STD 810F Environmental Criteria for Aircraft.

Environmental Criteria	Requirement
Temperature	Max Temp. = 160 ^{o}F, Min. Temp. = -65^{o}F
Humidity (Relative %)	100 %
Salt Fog	48 hrs at 5 ±1% Salt Solution
Vibration/Shock	Based on Material

These requirements set the stage for the tests conducted to examine the feasibility of replacing the existing chromate containing coating with a non chromate containing conversion coating (referred to as environmentally friendly conversion coating in this document) for the ZE41A gearbox housing.

H-60 Helicopter Gearbox Housing

The H-60 gearbox housing provides protection to the power transmission components that lead from the main engines to the main rotor, vertical stabilizing rotor

and two auxiliary power units. The gearbox contains fluid to provide lubrication to the gears which interface the main engine drives to the rotors and auxiliary power units.[4]

The H-60 gearbox housing tested in this document is magnesium alloy ZE41A. It should be noted that there are four major features to be considered in the naming strategy used for magnesium alloys. Magnesium alloy designations begin with a two letter sequence describing the two major constituents of the alloy. In the case of AZ91E-T6, the two major alloying elements are aluminum designated by the capital letter A and zinc, designated by the capital letter Z. The next two digits are two numbers that represent the respective weight percents of each major alloying element. In the instance of AZ91E – T6, the 9 represents an atomic weight percent of 9 for aluminum while the 1 represents that an atomic weight percent of 1 for zinc exists in the alloy. The next component of this designation refers to the revision of the alloy. In the case of AZ91E – T6, this is the fifth alloy to be alloyed with 9 percent by atomic weight of aluminum and 1 percent by atomic weight of zinc. It also gives insight into the corrosion resistance of the alloy relative to subsequent letter designations of the alloy. Most magnesium alloys are revised to improve corrosion resistance. For instance, AZ91E – T6 is more corrosion resistant than AZ91C – T6. The final portion of this designation is the temper designation. Table 2 provides a list of temper designations for magnesium alloy ZE41A which shows that ZE41A is composed of four percent by atomic weight zinc and one percent by atomic weight rare earth metals such as cerium and misch metals.

Table 2: Temper designation and heat treatments for different Mg. alloys.[5]

Alloy	Final temper	Aging (a)			Solution treating (e)					Aging after solution treating		
		Temperature		Time, h	Temperature		Time, h	Maximum temperature		Temperature		Time, h
		°C, ±6 (b)	°F, ±10 (b)		°C, ±6 (b)	°F, ±10 (b)		°C	°F	°C, ±6 (b)	°F, ±10 (b)	
Magnesium-aluminum castings (d)												
AM100A	T5	232	450	5	…	…	…	…	…	…	…	…
	T4	…	…	…	424 (e)	795 (e)	16-24 (e)	432	810	…	…	…
	T6	…	…	…	424 (e)	795 (e)	16-24 (e)	432	810	232	450	5
	T61	…	…	…	424 (e)	795 (e)	16-24 (e)	432	810	218	425	25
AZ63A	T5	260 (f)	500 (f)	4 (f)	…	…	…	…	…	…	…	…
	T4	…	…	…	385	725	10-14	391	735	…	…	…
	T6	…	…	…	385	725	10-14	391	735	218 (f)	425 (f)	5 (f)
AZ81A	T4	…	…	…	413 (e)	775 (e)	16-24 (e)	418	785	…	…	…
AZ91C	T5	168 (g)	335 (g)	16 (g)	…	…	…	…	…	…	…	…
	T4	…	…	…	413 (e)	775 (e)	16-24 (e)	418	785	…	…	…
	T6	…	…	…	413 (e)	775 (e)	16-24 (e)	418	785	168 (h)	335 (h)	160 (h)
AZ92A	T5	260	500	4	…	…	…	…	…	…	…	…
	T4	…	…	…	407 (i)	765 (i)	16-24 (i)	413	775	…	…	…
	T6	…	…	…	407 (i)	765 (i)	16-24 (i)	413	775	218	425	5
Magnesium-zinc copper castings												
ZC63A (j)	T6	…	…	…	440	825	4-8	445	835	200	390	16
Magnesium-zirconium castings												
EQ21A (j)	T6	…	…	…	520	970	4-8	530	985	200	390	16
EZ33A	T5	175	350	16	…	…	…	…	…	…	…	…
QE22A (j)	T6	…	…	…	525	980	4-8	538	1000	204	400	8
QH21A (j)	T6	…	…	…	525	980	4-8	538	1000	204	400	8
WE43A (j)	T6	…	…	…	525	980	4-8	535	995	250	480	16
WE54A (j)	T6	…	…	…	527	980	4-8	535	995	250	480	16
ZE41A	T5	329 (k)	625 (k)	2 (k)	…	…	…	…	…	…	…	…
ZE63A(l)	T6	…	…	…	480	895	10-72	491	915	141	285	48
ZK51A	T5	177 (m)	350 (m)	12 (m)	…	…	…	…	…	…	…	…
ZK61A	T5	149	300	48	…	…	…	…	…	…	…	…
	T6	…	…	…	499 (n)	930 (n)	2 (n)	502	935	129	265	48
Wrought products												
ZK60A	T5	150	300	24	…	…	…	…	…	…	…	…
AZ80A	T5	177	350	16-24	…	…	…	…	…	…	…	…
ZC71A (j)	T5	180	355	16	…	…	…	…	…	…	…	…
ZC71A (j)	T6	…	…	…	430	805	4-8	435	815	180	355	16

(a) Aging to the T5 temper is done from the as-fabricated (f) condition. (b) Except where quoted differently. (c) After solution treatment and before subsequent aging, castings are cooled to room temperature by fast fan cooling, except where otherwise indicated. Use carbon dioxide, sulfur dioxide, or 0.5 to 1.5% sulfur hexafluoride in carbon dioxide as a protective atmosphere above 400°C (750°F). (d) For solution treating, Mg-Al-Zn alloys are loaded into the furnace at 260°C (500°F) and brought to temperature over a 2-h period at a uniform rate of temperature increase. (e) Alternative treatment to prevent germination (excessive grain growth): 6h at 413 ± 6°C (775 ± 10°F), 2h at 352 ± 6°C (665 ± 10°F), 10h at 413 ± 6°C (775 ± 10°F). (f) Alternative treatment: 5h at 232 ± 6°C (450 ± 10°F). (g) Alternative treatment: 4h at 216 ± 6°C (420 ± 10°F). (h) Alternative treatment: 5 to 6h at 216 ± 6°C (420 ± 10°F). (i) Alternative treatment to prevent germination (excessive grain growth): 6h at 407 ± 6°C (765 ± 10°F), 2h at 352 ± 6°C (665 ± 10°F), 10h at 407 ± 6°C (765 ± 10°F). (j) Quench from solution-treating temperature either in water at 65°C (150°F) or in other suitable medium. (k) This treatment is adequate for development of satisfactory properties; it may be followed by 16h at 177 ± 6°C (350 ± 10°F) to provide very slight improvements in mechanical properties. (l) Alloy ZE63A must be solution treated in a special hydrogen atmosphere because its mechanical properties are developed through hydriding of some of its alloying elements. Hydriding time depends on section thickness; as a guide, 6.4 mm (1/4 in.) sections require approximately 10h, and 19 mm (3/4 in.) sections require about 72h. Following solution treatment, ZE63A should be quenched in oil, water spray, or air blast. (m) alternative treatment: 8h at 218 ± 6°C (425 ± 10°F). (n) Alternative treatment: 10h at 482 ± 6°C (900 ± 10°F).

Environmental Exposures

The H-60 gearbox housing is not directly exposed to the same environmental conditions that the external components of the aircraft are exposed to but must meet the same stringent requirements as outlined by MIL-STD 810F. In addition to these requirements, the gearbox housing is also exposed to aviation fluids such as Jet Petroleum 8 (JP8), Royco 555 aviation hydraulic fluid and Royco 787 turbine lubricating oil.[4] The risk of corrosion increases as the exposure time and temperature increase as the coating breaks down at elevated temperatures. The ZE41A's mechanical properties begin to deteriorate at temperatures exceeding 160^{o}C.

Magnesium Alloys

Mechanical Properties

Magnesium alloys are used in many applications where reducing weight, is a critical factor in design. Many industries ranging from energy to transportation enjoy the benefits of the lightweight to high strength capabilities of magnesium alloys. Magnesium alloys have the lowest density of all construction materials.[6] The average density of a magnesium alloy is about 1.8 g/cm^3, that is approximately two-thirds the density of aluminum and approximately one-fourth the density of steel.[7] Magnesium alloys also possess a relatively high tensile strength with respect to construction materials giving them a high specific strength. In addition to a high specific strength, magnesium alloys also benefit from high damping capacity, lower cost in machining in terms of less tool wear due to the soft nature of magnesium alloys, high dent resistance, low susceptibility to crocking (wear by sliding) and low thermal neutron cross section.[8]

Table 4 lists a summary of mechanical properties exhibited by several magnesium alloys. Although these characteristics are desirable characteristics in a construction material, the benefits that are provided by these characteristics may be out weighed by the undesirable nature of this material's propensity to corrosion.

Corrosion Properties

Thus far, properties of magnesium have shown that this construction material is lightweight and exhibits high strength properties. However, Table 3, the standard EMF series shows one of the major drawbacks to using magnesium as a construction material. This table shows that magnesium is the most active construction material relative to the other construction materials listed.

Table 3: Standard reduction potentials.[10]

Electrode	Reaction	Potential V
Li, Li^+	$Li^+ + e^- \rightarrow Li$	-3.02
K, K^+	$K^+ + e^- \rightarrow K$	-2.92
Na, Na^+	$Na^+ + e^- \rightarrow Na$	-2.71
Mg, Mg^{2+}	$Mg^{2+} + 2e^- \rightarrow Mg$	-2.37
Al, Al^{3+}	$Al^{3+} + 3e^- \rightarrow Al$	-1.71
Zn, Zn^{2+}	$Zn^{2+} + 2e^- \rightarrow Zn$	-0.76
Fe, Fe^{2+}	$Fe^{2+} + 2e \rightarrow Fe$	-0.44
Cd, Cd^{2+}	$Cd^{2+} + 2e^- \rightarrow Cd$	-0.4
Ni, Ni^{2+}	$Ni^{2+} + 2e^- \rightarrow Ni$	-0.24
Sn, Sn^{2+}	$Sn^{2+} + 2e^- \rightarrow Sn$	-0.14
Cu, Cu^{2+}	$Cu^{2+} + 2e^- \rightarrow Cu$	0.34
Ag, Ag^+	$Ag^+ + e^- \rightarrow Ag$	0.8

Table 4: Nominal compositions and typical room-temperature mechanical properties of magnesium alloys.[9]

Alloy	Composition, %						Tensile Strength		Yield Strength						Elongation in 50 mm (2 in.), %	Shear strength		Hardness, HRB (e)
									Tensile		Compressive		Bearing					
	Al	Mn(a)	Th	Zn	Zr	Other (b)	MPa	Ksi	MPa	ksi	MPa	ksi	MPa	Ksi		MPa	Ksi	
Sand and permanent mold castings																		
AM100A-T61	10.0	0.1	…	…	…	…	275	40	150	22	150	22	…	…	1	…	…	69
AZ63A-T6	6.0	0.15	…	3.0	…	…	275	40	130	19	130	19	360	52	5	145	21	73
AZ81A-T4	7.6	0.13	…	0.7	…	…	275	40	83	12	83	12	305	44	15	125	18	55
AZ91C- and E-T6(d)	8.7	0.13	…	0.7	…	…	275	40	145	21	145	21	360	52	6	145	21	66
AZ92A-T6	9.0	0.10	…	2.0	…	…	275	40	150	22	150	22	450	65	3	150	22	84
EQ21A-T6	…	…	…	…	0.7	1.5 Ag, 2.1 Di	235	34	195	28	195	28	…	…	2	…	…	65-85
EZ33A-T5	…	…	…	2.7	0.6	3.3 RE	160	23	110	16	110	16	275	40	2	145	21	50
HK31A-T6	…	…	3.3	…	0.7	…	220	32	105	15	105	15	275	40	8	145	21	55
HZ32A-T5	…	…	3.3	2.1	0.7	…	185	27	90	13	90	13	255	37	4	140	20	57
K1A-F	…	…	…	…	0.7	…	180	26	55	8	…	…	125	18	1	55	8	…
QE22A-T6	…	…	…	…	0.7	2.5 Ag, 2.1 Di	260	38	195	28	195	28	…	…	3	…	…	80
QH21A-T6	…	…	1.0	…	0.7	2.5 Ag, 1.0 Di	275	40	205	30	…	…	…	…	4	…	…	…
WE43A-T6	…	…	…	…	0.7	4.0 Y, 3.4 RE	250	36	165	24	…	…	…	…	2	…	…	75-95
WE54A-T6	…	…	…	…	0.7	5.2 Y, 3.0 RE	250	36	172	25	172	25	…	…	2	…	…	75-95
ZC63A (j)	…	0.25-0.75	…	6.0	…	2.7 Cu	210	30	125	188	…	…	…	…	4	…	…	55-65
ZE41A-T5	…	…	…	4.2	0.7	1.2 RE	205	30	140	20	140	20	350	51	3.5	160	23	62
ZE63A-T6	…	…	…	5.8	0.7	2.6 RE	300	44	190	28	195	28	…	…	10	…	…	60-85
ZH62A-T5	…	…	1.8	5.7	0.7	…	240	35	170	25	170	25	340	49	4	165	24	70
ZK51A-T5	…	…	…	4.6	0.7	…	205	30	165	24	165	24	325	47	3.5	160	23	65
ZK61A-T5	…	…	…	6.0	0.7	…	310	45	185	27	185	27	…	…	…	170	25	68
ZK61A-T6	…	…	…	6.0	0.7	…	310	45	195	28	195	28	…	…	10	180	26	70
Die castings																		
AM 60A- and B-F(e)	6.0	0.13	…	…	…	…	205	30	115	17	115	17	…	…	6	…	…	…
AS21X1	1.7	0.4	…	…	…	1.1 Si	240	35	130	19	130	19	…	…	9	…	…	…
AS41A-F(f)	4.3	0.35	…	…	…	1.0 Si	220	32	150	22	150	22	…	…	4	…	…	…
AZ91A, B, and D-F(g)	9.0	0.13	…	0.77	…	…	230	33	150	22	165	24	…	…	3	140	20	63
Extruded bars and shapes																		
AZ10A-F	1.2	0.2	…	0.4	…	…	240	35	145	21	69	10	…	…	10	…	…	…
AZ21X1-F(h)	1.8	0.02	…	1.2	…	…	…	…	…	…	…	…	…	…	…	…	…	…
AZ31 B and C-F(i)	3.0	…	…	1.0	…	…	260	38	200	29	97	14	230	33	15	1330	09	49
AZ61A-F	6.5	…	…	1.0	…	…	310	45	230	33	130	19	285	41	16	140	20	60
AZ80A-T5	8.5	…	…	0.5	…	…	380	55	275	40	240	35	…	…	7	165	24	82
HM31A-F	…	1.2	3.0	…	…	…	290	42	230	33	185	27	345	50	10	150	22	…
M1A-F	…	1.2	…	…	…	…	255	37	180	26	83	12	195	28	12	125	18	44
ZC71-F	…	0.5-1.0	…	6.5	…	1.2 Cu	360	52	340	49	…	…	…	…	5	…	…	70-80
ZK21A-F	…	…	…	2.3	0.45(a)	…	260	38	195	28	135	20	…	…	4	…	…	…
ZK40A-T5	…	…	…	4.0	0.45(a)	…	276	40	255	37	140	20	…	…	4	…	…	…
ZK60A-T5	…	…	…	5.5	0.45(a)	…	365	53	305	44	250	36	405	59	11	180	26	88
Sheet and plate																		
AZ31B-H24	3.0	…	…	1.0	…	…	290	42	220	32	180	26	325	47	15	160	23	73
HK31A-H24	…	…	3.0	…	0.6	…	255	37	200	29	160	23	285	41	9	140	20	68
HM21A-T8	…	0.6	2.0	…	…	…	235	34	170	25	130	19	270	39	11	125	18	…
PE(j)	3.3	V	V	0.7	…	…	…	…	…	…	…	…	…	…	…	…	…	…

(a) Minimum. (b) RE, rare earth: Di, didymium, (a mixture of rare-earth elements made up chiefly of neodymium and praseodymium). (c) 500 kg load, 10 mm ball. (d) Properties of C and E are identical, but AZ91E castings have maximum containment levels of 0.005% Fe, 0.0010% Ni, and 0.015% Cu. (e) Properties of A and B are identical, but AM60B castings have maximum contaminant levels of 0.005% Fe, 0.002% Ni, and 0.010% Cu. (f) Properties of A and XB are identical, but AS41XB castings have maximum contaminant levels of 0.0035% Fe, 0.002% Ni, and 0.020% Cu. (g) Properties of A, B, and D are identical, except that 0.30% max residual Cu is allowable in AZ91B, and AZ91D castings have maximum contaminant levels of 0.005% Fe, 0.002% Ni, and 0.030% Cu. (h) For battery applications. (i) Properties of B and C are identical, but AZ31C has 0.15% min Mn, 0.1% max Cu, and 0.03% max Ni. (j) Photoengraving grade

Magnesium is the most corrosion prone construction material used in design.[9] However, magnesium alloys can be protected using various schemes ranging from coating protection systems to mechanical design modifications such as drain holes or insulators that prevent galvanic coupling in the presence of an electrolyte on the casting. In fact, magnesium alloys can form a surface film that naturally protects the alloys in both rural and urban atmospheres. However, if chlorides, sulfates and other foreign material are present on the surface or in the environment, corrosion is likely to occur. One of the most common methods of corrosion in magnesium alloys is the entrapment of salt water in areas that allow the water to act as an electrolyte in a galvanic coupling mechanism.

Corrosion Tests

Salt water conditions usually present the most corrosive types of environments. As such, there is a commonly employed test method to evaluate the corrosion resistance of materials in saline environments. ASTM B117, commonly referred to as a salt fog test, was developed as a general test that allows investigators to develop data that is useful in determining a material's corrosion resistance. The test sets a benchmark for saline environments by testing the materials corrosion resistance to a 5% saline solution over a known period of time. Based on the materials application, the period of time which the material begins to exhibit signs of corrosion varies. The investigators can determine the extent of corrosion that will occur for a particular material in a salt water environment for a given amount of time. ASTM B117 does not detail the method used to determine the extent of corrosion that will occur for a particular material in a salt water environment for a given amount of time, however this corrosion rate can be expressed in

terms of MPY (mills penetration per year) using the following relationship between weight loss in milligrams, density in grams per cubic centimeter, area in square inches and time in hours.[11]

$$MPY = \frac{534W}{DAT}$$

Other tests exist for testing various materials in various applications for salt water corrosion. One such test that is geared toward the automotive industry is GM9540. This test sets similar criteria to ASTM B117 with more applied testing scenarios. For instance, GM9540 and ASTM B117 are applied to a ZE41A gearbox in the H60 helicopter. GM9540 is a more stringent salt fog test than ASTM B117 in that the test is performed using higher saline concentrations for harsh salty conditions that exist on roads during the winter months in the northern United States.

Corrosive Environments

In fresh water, magnesium alloys do not corrode because they rapidly form a protective film, $Mg(OH)_2$. Magnesium alloys can form the following films which are determined by the environment they are exposed to:[6]

- $Mg(OH)_2$ (magnesium hydroxide)
- $3MgCO_3 * Mg(OH)_2*3H_2O$ (hydromagnesite)
- $MgCO_3 * 3H_2O$ (nesquehonite)
- $MgCO_3 * 5H_2O$ (lansfordite)
- $MgCO_3 * 5Mg(OH)_2 * 2Al(OH)_3 * 4H_2O$ (hydrotalcite), if aluminum is present
- $MgSO_4$ (magnesium sulphate)
- $MgSO_4 * 7H_2O$ (epsomite)

If trace amounts of salts or heavy metals exist in the solution, corrosion will start. Magnesium alloys do not corrode in stagnant fresh water but will begin corroding in fresh water that is agitated because of the solubility limit impact of $Mg(OH)_2$. When the water is agitated, $Mg(OH)_2$ cannot reach its solubility limit; therefore a protective film cannot form, allowing corrosion to begin.

Conversely, in saltwater solutions, severe corrosion may occur when transition metals such as iron, nickel and copper are present. The chloride in the salt water solutions help to break down the protective film on magnesium while the transition metals act as cathodes on the anodic magnesium surface for these instances. It is important to note that chromates, vanadates, phosphates are film forming and help to retard corrosion, except at elevated temperatures. An example of the effects of impurities such as iron, nickel and copper in magnesium alloys can be seen in Figure 1.

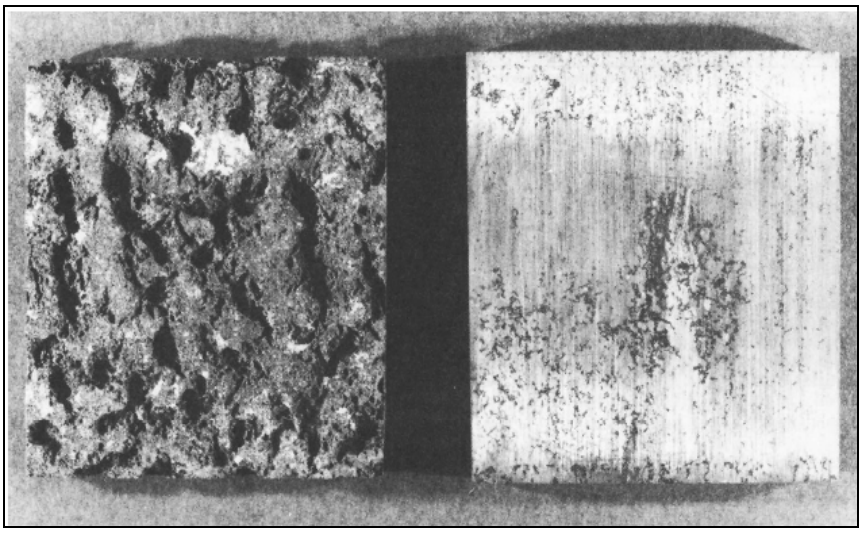

Figure 1: Effects of Iron, Nickel and Copper in Magnesium Alloys. Courtesy of ASM Metals Handbook Volume 13[7]

Magnesium is attacked by most acids with the exception of hydrofluoric acid (HF). Fluorides are known to form insoluble films on magnesium alloys. In the case of

HF and magnesium alloy interactions, an insoluble magnesium fluoride film forms, thereby protecting the magnesium from attack. With respect to organic compounds, "aliphatic and aromatic hydrocarbons, ketones, ethers, glycols, and higher alcohols are not corrosive to magnesium and its alloys."[9] However, fuels that have water contents that exceed 0.25% are more prone to cause corrosion. In addition, ethylene glycol solutions do not cause corrosion even when galvanically coupled to steel unless temperatures exceed 115^{o}C. With respect to gases, magnesium alloys do not corrode in the presence of dry gases. However, when water is added to the gas in terms of vapor, corrosion is likely to occur. It should be noted that cerium, lanthanum, calcium and beryllium reduce the oxidation rate below that of pure magnesium at elevated temperatures when included as alloy constituents for magnesium alloys. Magnesium alloys do not corrode in nonsaline soils.[10]

One of the underlying themes behind mechanisms of corrosion as they apply to magnesium in the corrosive environments listed above is that water is present. This is not a coincidence. Magnesium normally forms a passive layer with hydroxide. However, when water is added, this hydroxide layer is broken down. The following series of chemical reactions shows how this breakdown occurs beginning with the reaction of the formation of a magnesium hydroxide passive layer.

$$Mg + 2OH^{-} \rightarrow Mg(OH)_2 + 2e^{-}$$

When water is added, the following reaction occurs.

$$2H_2O + 2e^- \rightarrow 2OH^- + H_2$$

Finally, when exposed to an aqueous solution containing chloride, sulfide, etc. (with the exception of fluoride ions), the following reduction reaction results.[6]

$$Mg + 2H^+ \rightarrow Mg^{+2} + H_2$$

It should be noted that this reaction applies for pure magnesium. In the case of magnesium alloys, the reduction reaction becomes more important during the design and manufacturing stages of the alloy. When designing a magnesium alloy for an environment that contains a high degree of chlorides, sulfides, etc, the alloy must avoid containing elements such as iron, copper and nickel that would act as catalysts for the reduction reaction. Typically, elements with high solubility and a low electropotential deviation from magnesium are used. However, during the manufacturing stages, poor or less stringent manufacturing techniques that allow impurities to enter the material as it is being cast can significantly affect the corrosion resistance of the alloy. The potential uses for magnesium alloys as a lightweight high strength material were realized as early as the early to mid nineteen hundreds. However, it was also noticed that magnesium does experience significant corrosion in salt water conditions that put limits on structural applications. In fact, Hanawalt, Nelson and Peloubet of DOW Chemical Company noticed that "all researchers worked with base metal in which metallic impurities varied in uncontrolled amounts." This led the research team to conclude that the most significant contribution of corrosion is impurities within the alloy and not external

factors.[5] Furthermore, a paper by Aghion and Bronfin presented at the Third International Mangesium Conference indicates that a corrosion rate that is directly related to the amount of impurities in a casting can be calculated. The equation they developed from their experimental results is as follows where mass fractions are represented in percentages for each elemental species:[12]

$$CR, MPY = 4\%Mg - 54\%Al - 16\%Zn - 206\%Mn + 24\%Si + 28 \times 10^3 \%Fe + 12.15 \times 10^4 \% Ni + 11.7 \times 10^3 \%Cu$$

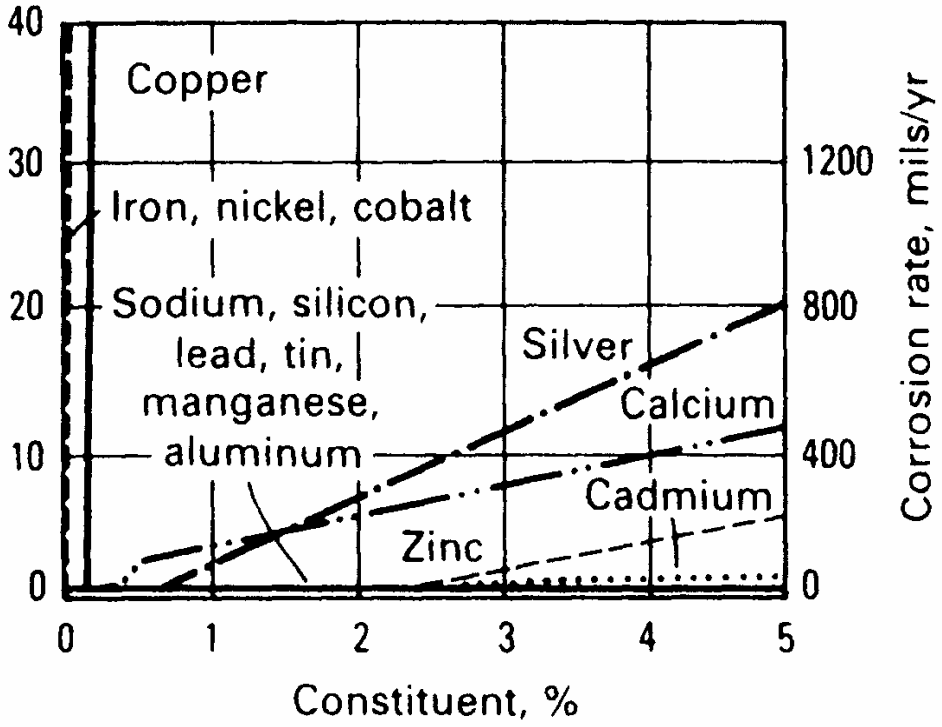

Figure 2: Effect of alloying and contaminant metals on the corrosion rate of magnesium as determined by alternate immersion in 3% NaCl solution.[10]

This relationship reinforces the idea that heavy metals such as iron, copper and nickel have a significant influence on corrosion for magnesium alloys. In addition, this

relationship shows that silicon is a major contributor to corrosion in magnesium alloys. Figure 2 shows the effect that impurities have on corrosion rates for magnesium alloys.

Modes of Corrosion

There are several common distinct modes of corrosion that occur for magnesium alloys. Pitting, stress and galvanic corrosion are some of the most common modes of corrosion observed in magnesium alloys.

Pitting

Pitting usually occurs in the instance of an inhomogeneous crystal structure in magnesium alloys. Galvanic potentials can be created between the alloy and impurities within the material. These galvanic potentials result in oxidation and corrosion which lead to material loss in these local areas. This is not classified as galvanic corrosion because the passive layer on the alloy surface is not broken.[6]

Stress Corrosion Cracking

Stress corrosion cracking is caused when tensile stresses combine with a corrosive medium to cause brittleness due to entrapped hydrogen evolved during the reduction process in a crack tip. In general, SCC (stress corrosion cracking) in magnesium alloys occurs more prominently in alloying systems that contain more aluminum and zinc. Studies, tests and analysis have been performed to determine factors that contribute to SCC susceptibility in magnesium alloying systems. These studies examined the following groups of factors when considering SCC:

- Alloying compositions and metal strengthening mechanisms
    - Product form and microstructure

    - Cold working
    - Heat treatmenting
- Effects of the environment
    - Air environments
    - Waterenvironments
        - Saline environments
        - Non-saline envrionments
- Effects of temperature
- Effects of strain rate and stress

Although these factors have been investigated and linked to SCC, there is only one observation from this list that has consistently been observed to promote SCC susceptibility, alloying compositions. Each factor except for alloying compositions have a set of observations that show cases where the factor has contributed to SCC susceptibility and the converse case. This section will summarize the findings for each of these factors.

Alloying Compositions and Condition

Aluminum containing magnesium alloys have the highest SCC susceptibility when compared to other magnesium alloys. The effective peak for SCC behavior in an aluminum-magnesium alloy is shown to occur at a 6% aluminum alloying content. Figure 3 and Figure 4 show the effect of aluminum content on a stress versus time to failure plot demonstrating the effective peak for SCC behavior in aluminum-magnesium alloys.

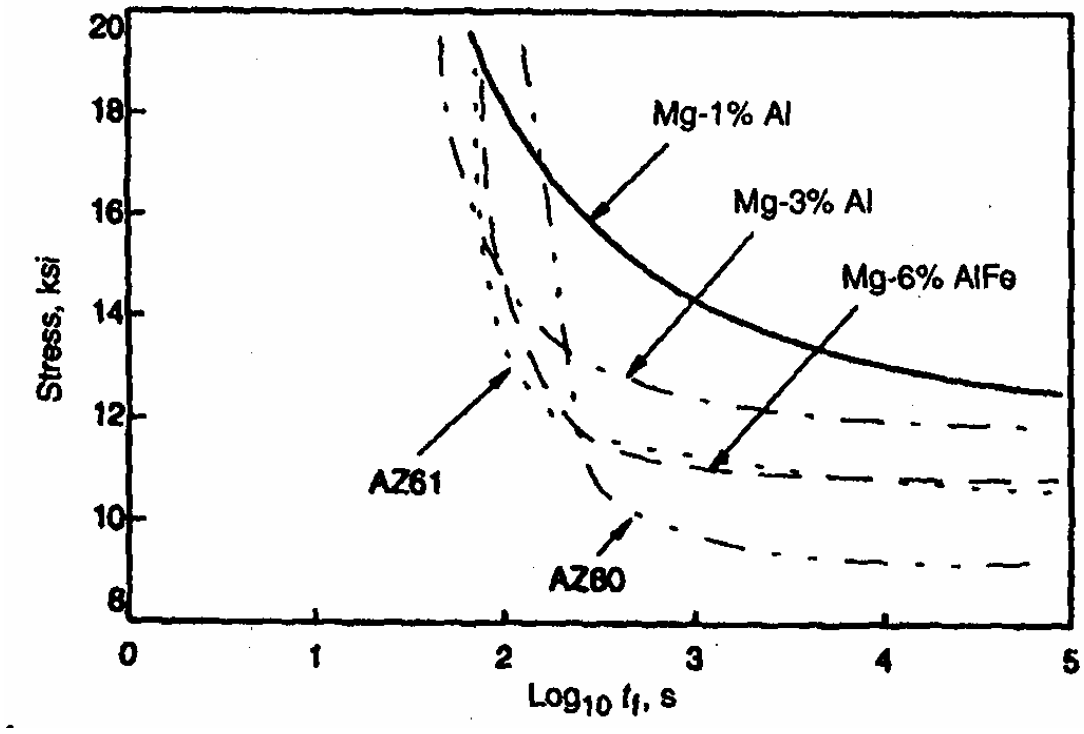

Figure 3: Stress versus time to failure (t_f) for magnesium-aluminum alloys in aqueous 40 g/L NaCl + 40 g/L Na_2CrO_4.

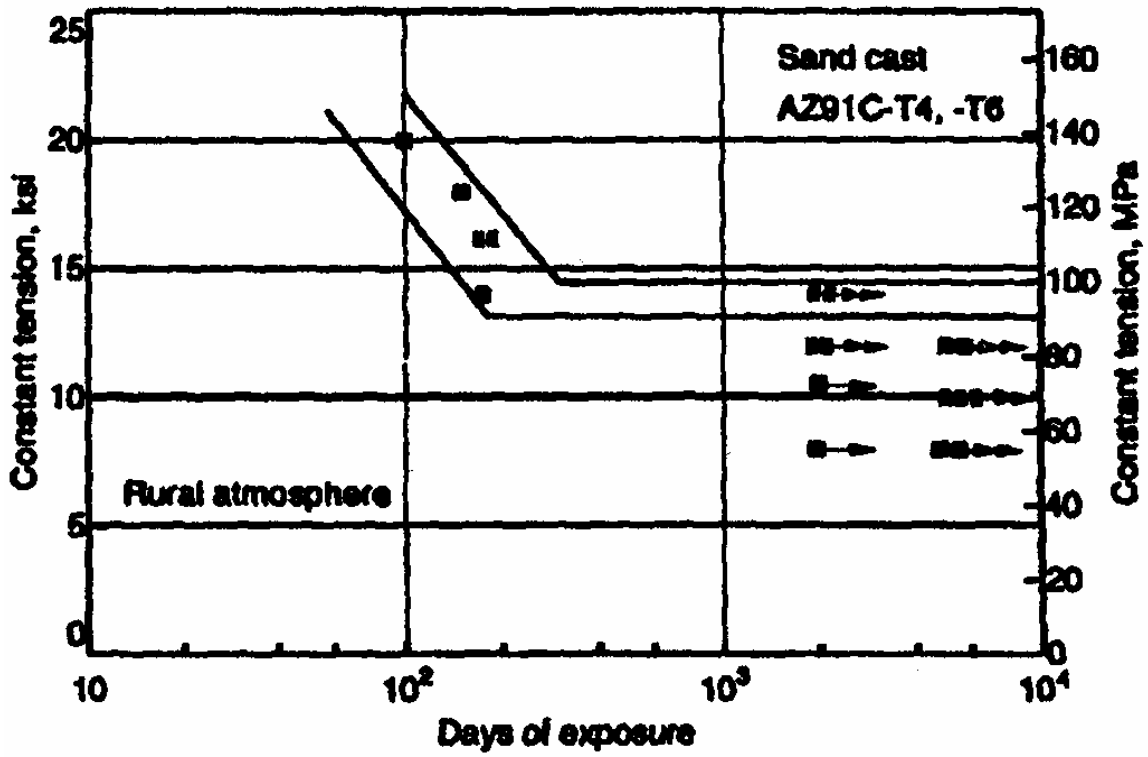

Figure 4: Stress corrosion of sand-cast AZ91C 9(T4 and T6) in rural atmosphere.

Zinc also promotes SCC susceptibility in magnesium alloys. Therefore it can be concluded that the most commonly used magnesium alloys, the AZ alloys have the greatest susceptibility to SCC. Magnesium-zinc alloys that contain zirconium or rare earths such as the ZK or ZE series exhibit intermediate SCC behavior that can occur in atmospheric environments with stresses that are at 50% of the material's yield strength. Figure 5 demonstrates ZK60A's intermediate SCC behavior when compared to the AZ system shown in Figure 4.

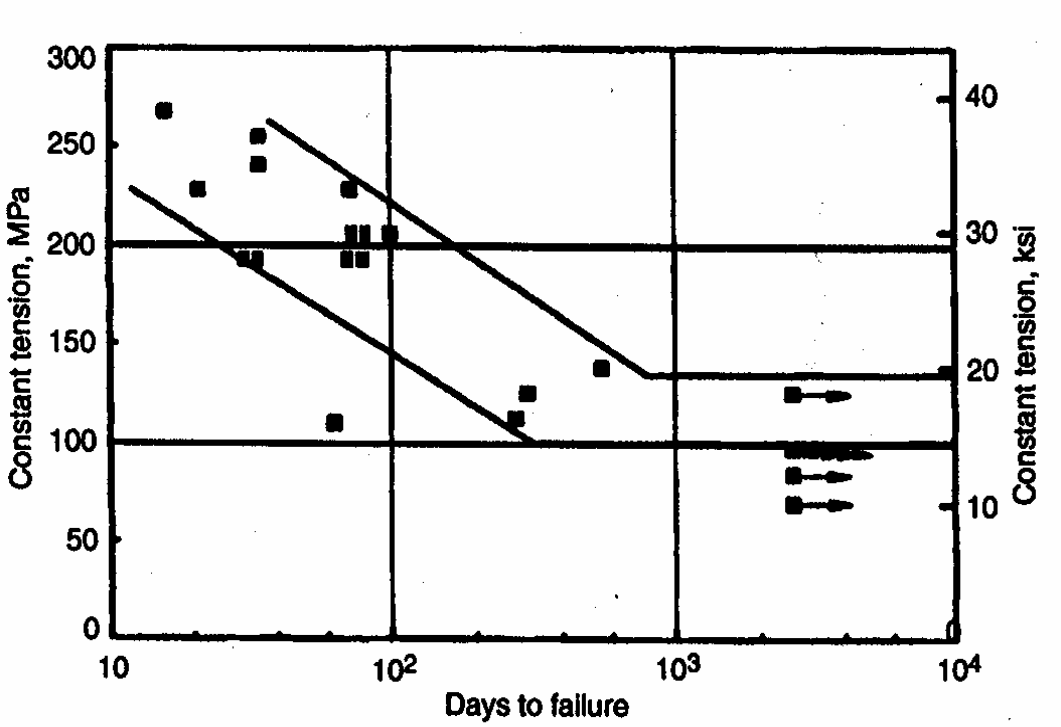

Figure 5: Stress corrosion of ZK60A-T5 extrusion in rural atmosphere.

It follows that magnesium alloys that do not contain aluminum or zinc, in general are the most SCC resistant. Manganese-magnesium alloys have the highest corrosion susceptibility, however QE22 also are significantly resistant to SCC while exhibiting 70 to 80% of its yield strength in rural atmosphere environments.[5]

Other elements such as iron in magnesium alloys have been shown to promote SCC behavior; on the other hand, studies also show that iron has little to no effect on SCC behavior. The effects of elements other than iron have not been studied well enough to determine if they significantly contribute to SCC susceptibility.[5]

Product Form and Microstructure

However, investigators have shown that rapid solidification, hydrogen and repassivation contribute to transgranular SCC as a result of hydrogen embrittlement.

Intergranular SCC has been linked to localized galvanic attack. This type of corrosion has been shown to produce a stress concentration that ruptures protective surface film thereby causing SCC.

Heat Treatment

Low-temperature stress relief heat treatments are standard methods of relieving residual stresses and SCC. However, heat treatments have not been found to be effective or ineffective in relieving residual stresses for magnesium alloys. Various aging treatments were also found to have no effect on relieving residual stresses or SCC.

Effects of Environment

When magnesium is exposed to environments that promote corrosion such as salt water, rural and industrial conditions, SCC susceptibility is also observed. However, it has not been shown to increase as moisture in the atmosphere increases. In addition, laboratory tests have shown that SCC behavior is observed only when indoor air conditions where at 85% to 98% relative humidity. Oxygen and carbon dioxide where shown to reduce this threshold.

Observations have shown that dissolved oxygen, distilled water and salt water promote SCC similarly. However, deaeration and an environmental pH greater than 12 inhibit SCC. It should be noted that "…no accelerated laboratory test has been developed that adequately predicts service life or the relative susceptibility of different [magnesium] alloys."[5]

Effects of Temperature

An increase in temperature under stress has been shown to increase the resistance to SCC in atmospheric environments such as water, H_2SO_4 + NaCl solution. Temperature has also been shown to affect creep behavior which may help to reduce SCC.

Effects of Strain and Stress

It is generally recommended that designers apply a 30% to 50% yield strength limit to magnesium alloys exhibiting SCC behavior. However, there have been cases where a component held to as little as 23% of its yield strength for 9 months has exhibited SCC. The 0.2% yield strength is generally measured for these cases. In the case of AZ91, the 30% yield strength limit is recommended. There have been studies that found strain rate to be an important factor in SCC susceptibility for magnesium alloys.[5]

Galvanic Corrosion

Galvanic corrosion occurs in many cases because the nature of corrosion mechanisms in magnesium alloys renders conventional protection schemes ineffective. Galvanic corrosion usually occurs between dissimilar metals. When using magnesium for structural applications, the interfaces must be considered carefully since magnesium will be the most anodic metal in any interface. Magnesium acts as an anode to any metallic interface so a galvanic potential between the two dissimilar materials will cause oxidation and reduction in the presence of an electrolyte as discussed in the corrosive environments section of this paper. A common environmental electrolyte with

detrimental corrosive effects is salt water. Common fastener materials include steel because of their high strength and availability. However, in many aircraft applications, aluminum is also used because of its high strength and lightweight. In both cases, if coupled with magnesium in the presence of salt water, corrosion will occur. The figures below show the results due to galvanic corrosion in a bolt and washer interface with a magnesium alloy.

Figure 6: Galvanic corrosion on a magnesium alloy automotive engine block.[6]

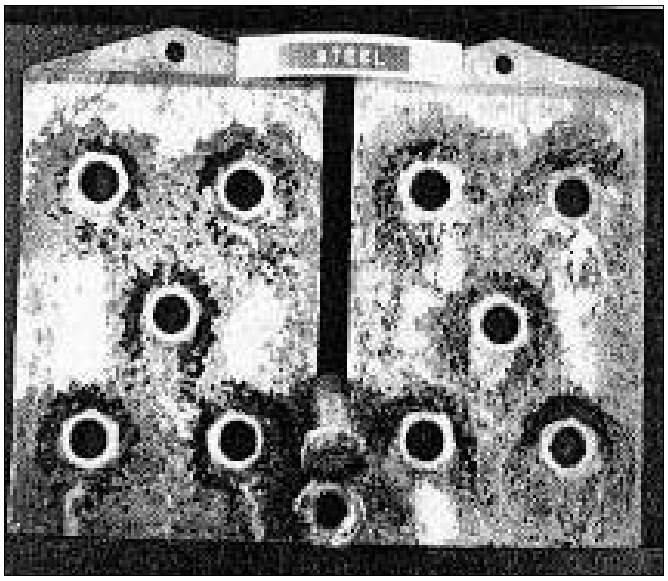

Figure 7: Galvanic corrosion of AZ91D with steel bolts.[10]

Magnesium Alloy Corrosion Prevention

There are several methods used to protect against and prevent corrosion. Using high purity alloys, coating systems that prevent electrolytic paths and mechanical design techniques to minimize electrolyte accumulation are the most commonly and effective used methods to prevent corrosion.

High Purity Alloys

The importance of using high purity alloys has been discussed in some of the aforementioned sections. However, re-emphasis is necessary to highlight its importance. High purity alloys reduce the effects of a galvanic couple within the material. Hanawalt, Nelson and Peloubet presented a definition of high purity magnesium alloys in their paper "Corrosion Studies of Magnesium and Its Alloys," that define purified magnesium alloys. Pure magnesium is defined to be 99.8% pure with the following allowances for impurities.[5] The following table provides this information.

Table 5: Contaminant levels in purified magnesium.[12]

Element	Fe	Ni	Al	Ca	Cu	Na	Mn	Pb	Si
Percent	<0.001	<0.0001	<0.001	<0.001	<0.0001	0.002	<0.0005	<0.01	<0.001

High purity magnesium alloys also reduce the tendency of the initial naturally formed passivating layer from breaking down. The naturally formed passivating layer is an important part of a magnesium alloy's defense against corrosion. In fact, it is the first and only line of defense magnesium alloys have. If this layer breaks down then corrosion

is eminent. Designers of this alloy have the opportunity to allow the material defend itself if high purity alloys are used.

Reducing Electrolytic Path

Coating Systems

An important defense against corrosion attack for magnesium alloys is accomplished by eliminating the electrolytic path between the magnesium alloy and free ions which may attach to the magnesium alloy; chemically combine and corrode the surface. In the case of magnesium alloys, it's often beneficial to employ a series of coatings which amount to a coating system to eliminate this electrolytic path. A coating system as opposed to a single coating is used because a single coating has not yet been developed to provide both adhesion and corrosion protection to the surface of magnesium alloys.

Magnesium alloys must first be coated with a conversion coating to provide adequate adhesion for subsequent coatings. The conversion coating helps to chemically convert the surface of the magnesium alloy so that subsequent coatings may adhere to this surface. The next layer which is to be applied on top of the conversion coating is a sealant coating. Since the conversion coating alone cannot provide corrosion resistance to the magnesium alloy in corrosive environments, the sealant provides the third line of defense, behind the sealant and top coat. Sealant coatings are typically made of epoxy resin, phenolic or epoxy silicone systems. It must be applied with three coats onto the conversion coating as specified by MIL-M-3171C to form an adequate seal for the conversion coating and magnesium alloy.[13] The third layer to be applied on top of the sealant coating is the primer. In many cases, strontium or zinc are incorporated into the

primer as pigment inhibiting agents. These primers have the ability to release chromate ions to retard corrosion in the event that the top coating is compromised. Last but not least, the top coat is applied. Some of the top coat's main functions include: resistance to water, resistance to hydrocarbons, resistance to acid, resistance to accelerated weathering, Resistance to chemical agents.[14]

The top coat is the first line of defense in preventing an electrolyte from being in contact with the magnesium alloy. In the case of the alloy and application discussed in this document, a coating system composed of the coatings layered to protect the H-60 rotor gearbox is shown in Figure 8.

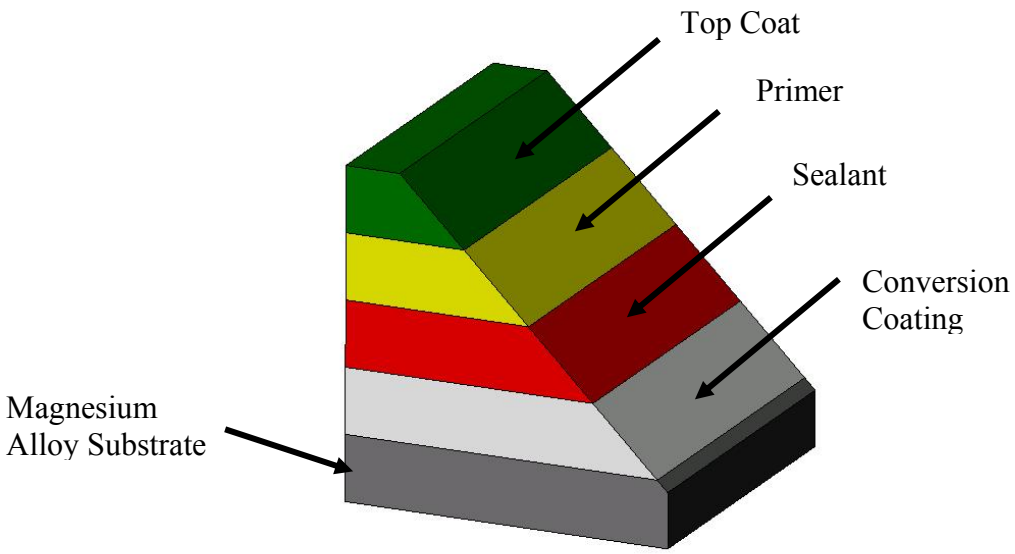

Figure 8: Layers of coating system used to protect ZE41A in the H-60 helicopter.

The focus of this research is to be directed toward the conversion coating shown between the sealant and ZE41A in Figure 8. Currently, magnesium alloy conversion coatings contain chromates. Because chromates are shown to cause significant health

problems such as kidney failure, liver damage, blood disorders and even death[1] an initiative is moving toward non chromate containing conversion coatings, e.g. environmentally friendly coatings.

Mechanical Design Schemes

Last but not least, mechanical design of the casting is an important consideration when developing a magnesium alloy for a particular application. As mentioned throughout this paper, one of the driving mechanisms behind corrosion on magnesium alloys is the presence of an electrolyte. If the presence of an electrolyte can be removed, then the effect of galvanic corrosion between dissimilar metals can be removed. Even if the presence of an electrolyte can be minimized, corrosion rates can be lowered to acceptable levels.

Classic mechanical design methods that involve the removal of an electrolyte operate behind the principle that prevents an electrolyte such as salt water from collecting in areas that would allow it to couple two dissimilar metals together. A relatively simple solution in avoiding the collection of liquid in areas where liquid can collect is the implementation of drain holes. Drain holes at the very least would minimize the concentration and electrolytic path between dissimilar metals. Another relatively feasible mechanical design feature that can be incorporated is some form of a buffer or spacer that helps to separate materials that would normally be coupled in an electrolytic solution. Spacers help to minimize events where electrolytes might bring the two dissimilar materials in question into contact. Figure 9 demonstrates scenarios where drain holes and spacers provide the most use.

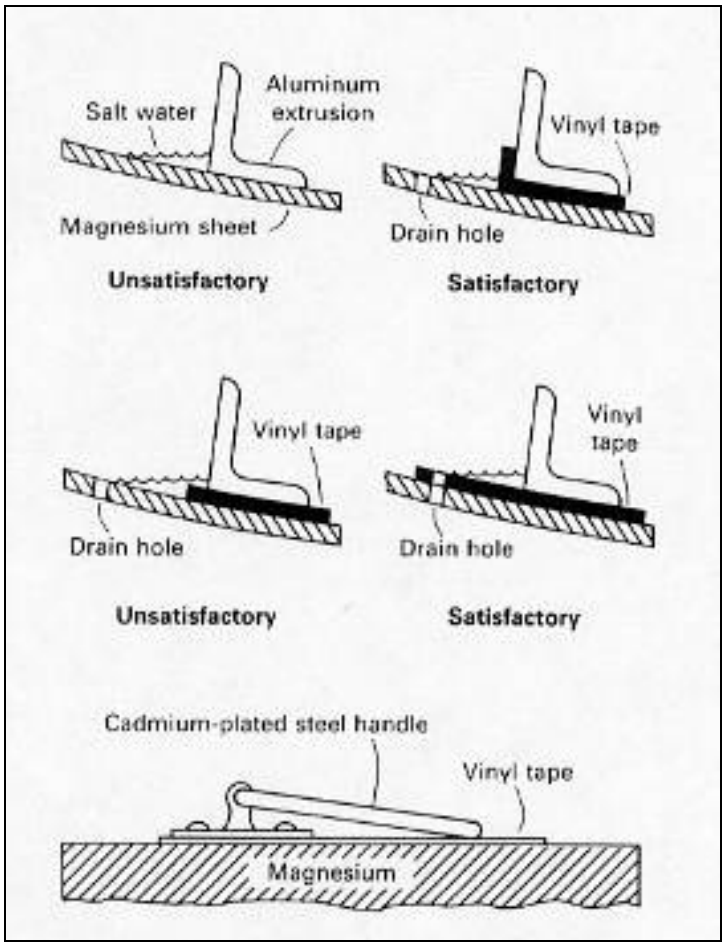

Figure 9: Mechanical design methods useful in the prevention of corrosion in magnesium alloys.[10]

The Environmentally Friendly Conversion Coating Measuring Problem

To implement a replacement coating for the currently chromate containing coating, the existing coating requirements must be met. The requirement categories are: fatigue properties, adhesion properties, fluid resistance properties, salt fog resistance properties, hydrogen embrittlement resistance properties, thickness of coating.[15]

A need for an environmentally green coating with consideration from the above requirements can be summarized as follows:

A need exists to prevent the loss of H-60 gearbox housings due to beyond economical repair (BER) criterion through corrosion prevention. The corrosion prevention methods in place do not conform to current environmental regulations due to the presence of hazardous chromates in the conversion coating used in the corrosion prevention coating system. A non-chromate containing replacement conversion coating must be tested to confirm that fatigue, fluid resistance compatibility, hydrogen embrittlement, salt fog and thickness properties to adhere to the requirements met by the current conversion coating.

This need is addressed by a company through a Small Business Innovation Research Program (SBIR) where an environmentally green substitute for the chromate conversion coating was developed. The coating is tested for the requirements listed in the need by the ACAA at Texas A&M University where the environmentally green coating met the same requirements that the chromate containing coating met.[16] However, thickness measurements recorded by the company could not be deemed as thickness measurements that could be published for the environmentally friendly coating. A Defelsko Corporation Poistest DFT eddy current measurement device is used to measure the environmentally friendly conversion coating. Coating thicknesses obtained from a series of measurements are between 0.02 and 0.22 mils or 0.508 to 5.588 microns. However, the error associated with this particular measurement device, ±0.1 mils + 3% error or ± 2 microns + 3% error, exceeded the measurements in some cases. This led to the pursuit of finding a more accurate method to determine the thickness of this environmentally friendly conversion coating.

Thickness Versus Coverage

Several well known techniques are used to find the thickness of the environmentally friendly coating and include the following: eddy current measurement, profilometry, optical microscopy, scanning electron microscopy, transmission electron microscopy, and confocal microscopy.

Of the five techniques listed above, only one provides results that give a clear and definitive thickness. Transmission electron microscopy proves to be the most useful method when finding thickness. However, sample preparation proved to be extremely difficult and is a destructive process. Alternatively, scanning electron microscopy may be possible with improved sample preparation but involves a sample destruction process. The eddy current measurement technique is useful because the sample being measured is not destroyed. This measurement technique makes it possible to measure samples for feasible quality assessment in the field but ultimately is ruled out as an option because of the error associated with the instrument. Because the conversion coating is one of the most important components in a successful corrosion protection scheme, quality is a paramount feature for the successful life of this component.[17] This fact makes it clear that a new method must be developed to assess the quality in the field.

Focused Research Need

A directed research need is developed to address this situation and provide directed research in this area.

A need exists to develop a cost effective, mobile, nondestructive evaluation technique to aid in the quality measurement of an environmentally green coating for magnesium

alloys. The technique should be applicable to a variety of magnesium alloy parts without altering the current repair coating time and effort.

Objectives

The specific objectives developed from this research need are listed below:

1) Show through development that defining coating coverage is more important than thickness measurements of the environmentally friendly coating.
2) Develop testing techniques to show that nondestructive evaluation techniques can be developed to determine coating coverage for the environmentally friendly conversion coating.
3) Provide data and analysis to support testing techniques developed to evaluate coating coverage.
4) Provide results that clearly summarize the data and analysis developed in objective 3.
5) Provide clear, concise conclusions of the results provided in objective 4.
6) Provide future plans of improvement in design of tests, additional testing and hardware implementation for nondestructive evaluation.

EXPERIMENTAL METHODS AND PROCEDURES

Several experiments are performed in this body of work to characterize both the thickness and surface coverage area of the environmentally friendly conversion coating. Some of the methods and procedures used for these experiments are standard experiments. However, some experiments are specifically developed for the purpose of gathering data for this particular application.

Thickness

Thickness measurements are gathered to meet the original need stated in the introduction section of this document. The idea behind gathering thickness data for the environmentally friendly coating is to establish that the coating is uniformly coated. Thickness measurements also help to determine a measurable parameter necessary to establish a quality baseline. This data is gathered using a combination of nondestructive, destructive, optical and non optical evaluation techniques. The experiments conducted to find thickness are: eddy current measurement, profilometry, optical microscopy, confocal microscopy, scanning electron microscopy and transmission electron microscopy.

Eddy Current Measurement

In general eddy current measurement techniques promote eddy currents in the metal which of the coating being evaluated through magnetic induction. As the coating thickness changes, the current that is promoted in the metal also changes. This change in current is measured through a magnetic inductor which acts a pickup to receive the change in the induced current in the metal. The instrument is calibrated to measure this

change in induced current as a change in vertical displacement of the instrument from the metal surface. This vertical displacement from the instrument is then interpreted as a coating thickness.[18]

Experiment Setup and Procedure

The eddy current measurement technique is conducted using a Defelsko Positest DFT detector. This experiment required almost no sample preparation. Four samples were tested for thickness. The first sample tested is a sample prepared by the coating developer with a base magnesium alloy, ZE41A substrate and an RMS < 125. This sample is the first sample tested before any other controlled samples are machined. These measurements can be considered preliminary in a sense.

The coating preparations are proprietary but are controlled by voltage, current and the amount of silicate and hydroxides that are added to the electrolytic bath. There are nine thickness measurement locations which are chosen on the sample. These locations are chosen based on an equally spaced grid pattern over an area approximately 4.6 by 12.4 centimeters. Twelve data points are measured using the Defelsko Positest DFT. The Figure 10 shows the location of the test points acquired for the first sample.

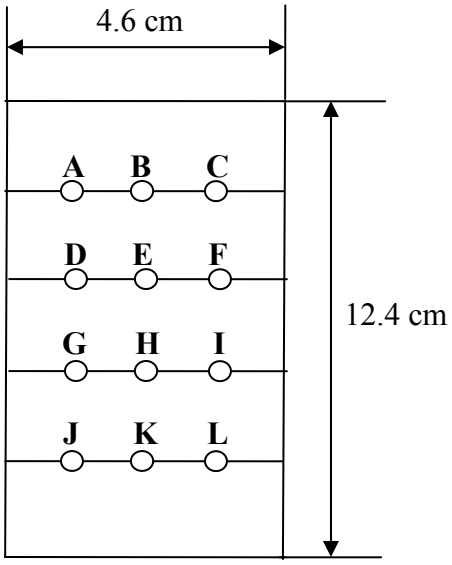

Figure 10: Location of data points collected for the eddy current measurement experiment.

Three more ZE41A samples coated with different coating conditions are measured with the Defelsko Positest DFT. The first of these samples is heavily coated with the environmentally friendly coating, the next sample is partially coated and last sample is lightly coated. Ten circular areas with an approximate diameter of one centimeter are marked as data point collection areas. These areas are to be used for other experiments performed in the body of this work. Three areas from each sample are chosen as data collection areas for this particular experiment. Data is collected from areas one, ten and between four and eight for the heavily coated sample as shown in Figure 11.

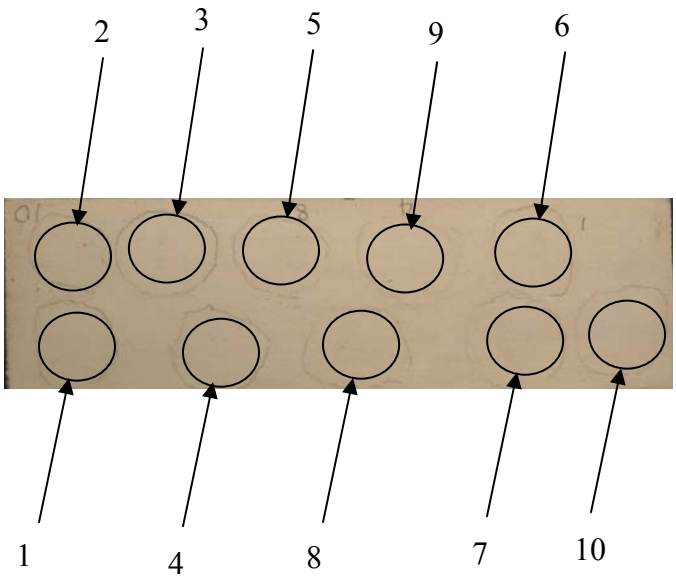

Figure 11: Sample areas for a ZE41A magnesium alloy sample heavily coated with the environmentally friendly conversion coating.

Data is collected from areas one, seven and three for the partially coated sample as shown in Figure 12.

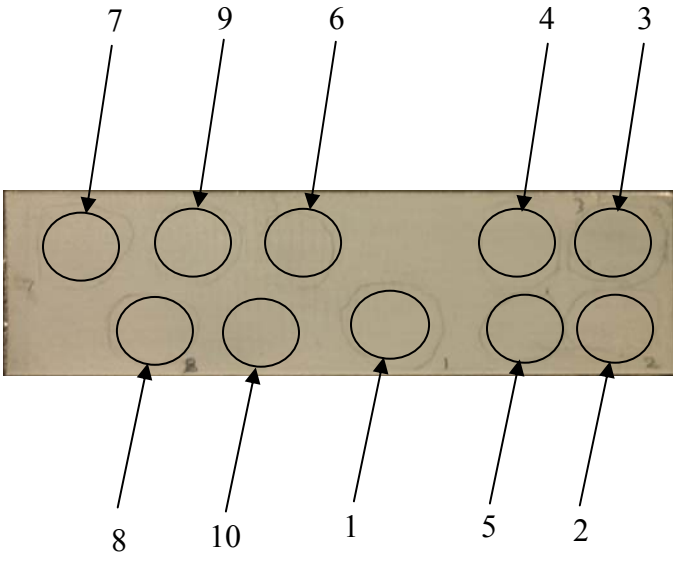

Figure 12: Sample areas for a ZE41A magnesium alloy sample partially coated with the environmentally friendly conversion coating.

Last but not least, data is collected in areas seven, one and three for the lightly coated sample as shown in Figure 13. Measuring thickness for these three conditions of coatings may help to provide more in depth information regarding the coating thickness.

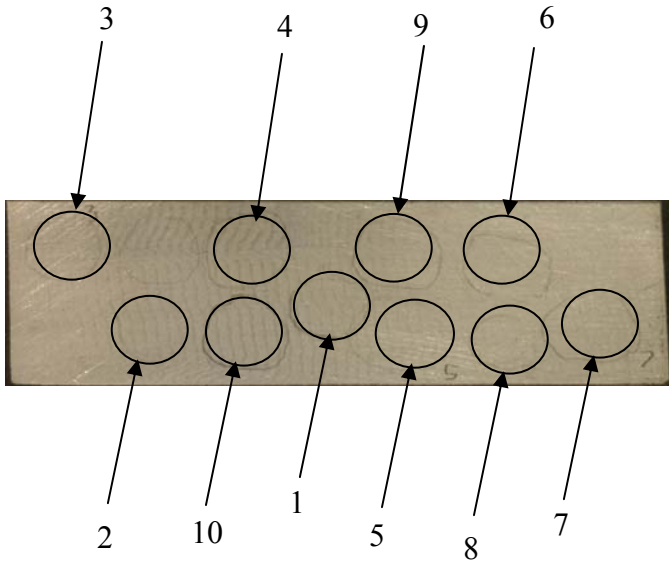

Figure 13: Sample areas for a ZE41A magnesium alloy sample lightly coated with the environmentally friendly conversion coating.

The coating thickness is measured by pressing the end of the Positest DFT firmly in contact with the coating and substrate (ZE41A) surface as shown in the Figure 14. The thickness measurement is then displayed in the digital output lcd screen of the Positest DFT.

Figure 14: Eddy current measurement technique.

Before taking measurements, the Positest DFT must be calibrated for proper readings. The Positest DFT is calibrated by taking random sample readings from an uncoated ZE41A test coupon, the control. The readings must produce a result of zero since no coating has been applied to this control surface. If the reading does not produce a zero result, the Positest DFT is zeroed using the zeroing function. A reading is then taken from a fabricated shim of known thickness. If the reading differs more than five percent, the instrument is zeroed again by measuring the uncoated surface. This process is repeated for five shims of known thickness 24, 53, 133, 250 and 534 microns.

Experimental Error

Because a real system is being studied, areas of variability in the experiment being conducted may exist. Possible sources of variability for the results of this

experiment may be attributed do to the following possible variables in the experimental setup:

- Roughness of test coupon
- Angle of Positest DFT at the interface between the Positest DFT and the coating

The roughness of the test coupon could possibly affect the readings of the recorded results for this experiment. Sources of variances in the roughness of the sample could come from uneven coating or an uneven substrate surface. An exaggerated view of this situation is shown in the Figure 15.

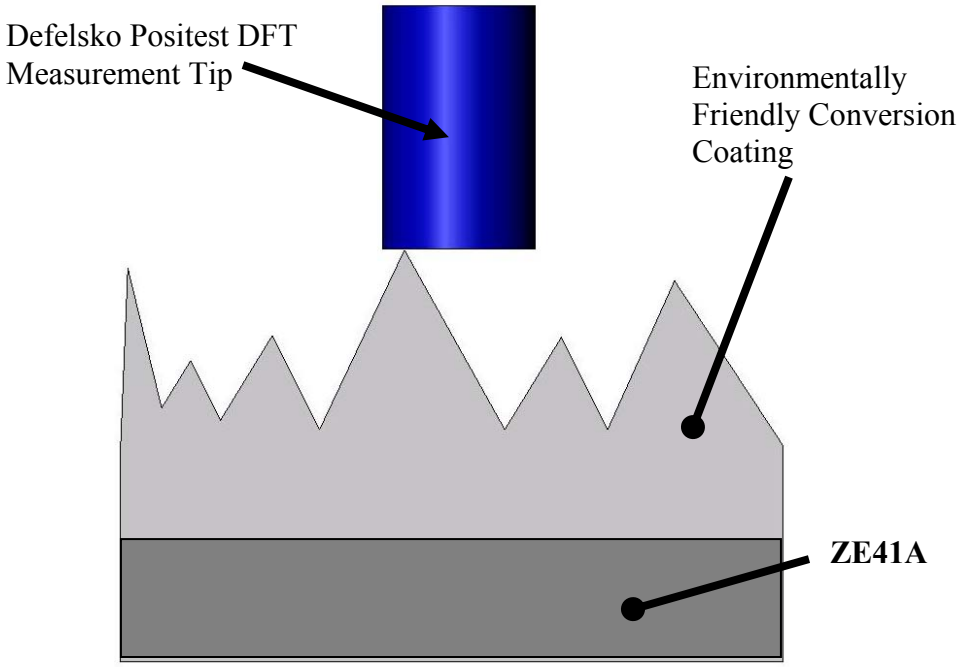

Figure 15: Exaggerated view of the environmentally friendly conversion coating surface which could lead to error in the eddy current measurement experiments.

To determine whether these variables affect the results, profilometry measurements are taken at each eddy current measurement location to determine the

flatness of the measured location. A three dimensional rendering of the surface of an area where a step is created is shown in Figure 17 is created from a two dimensional image shown in Figure 16 to give an illustration of the coating surface characteristics. The illustration in Figure 17 helps to verify the type of data to be expected from profilometry measurements.

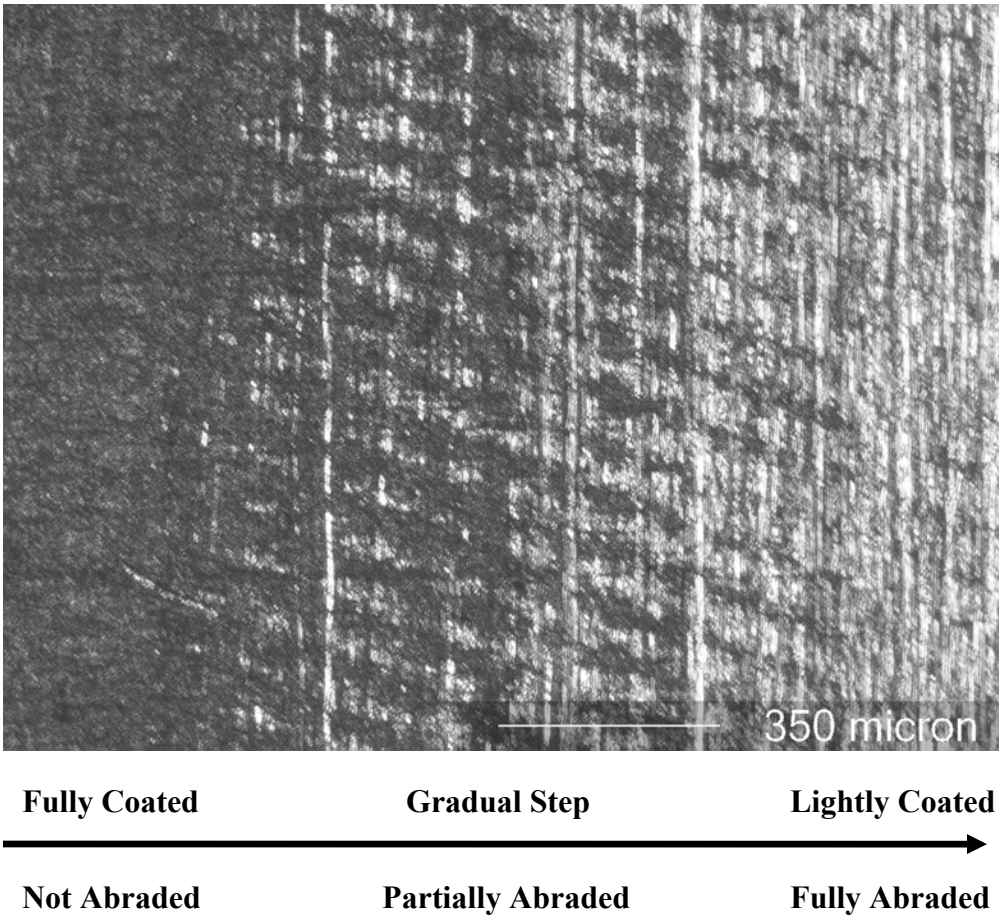

Figure 16: Transition between a coated and uncoated ZE41A surface created using Scotch Brite abrasive pads. A Zeiss Epiphot at 5X magnification with a 0.1 numerical aperture is used for image acquisition.

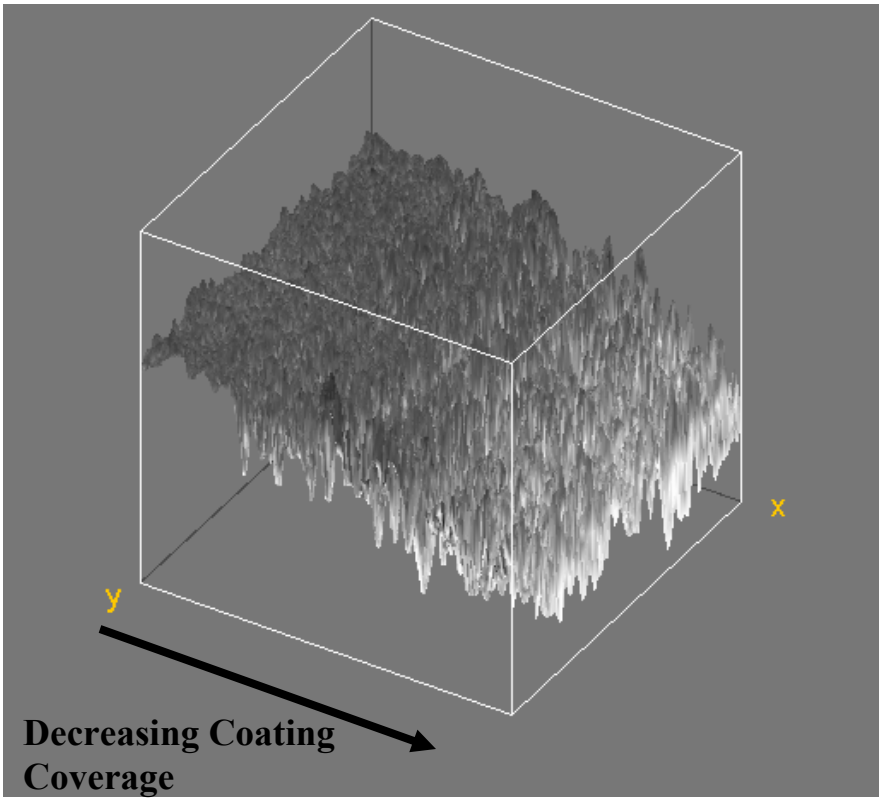

Figure 17: Three dimensional rendering of Figure 16 using Image J Volume J 3-D volume rendering plug-in. Image should be used for illustration purposes only.

The second variable in the experimental setup for consideration is the angle at which the Positest DFT to coating/substrate interface makes during the measurement recording process. If the experimenter does not take measurements that are parallel to the surface, error could result. An exaggerated view of this scenario is illustrated in the Figure 18.

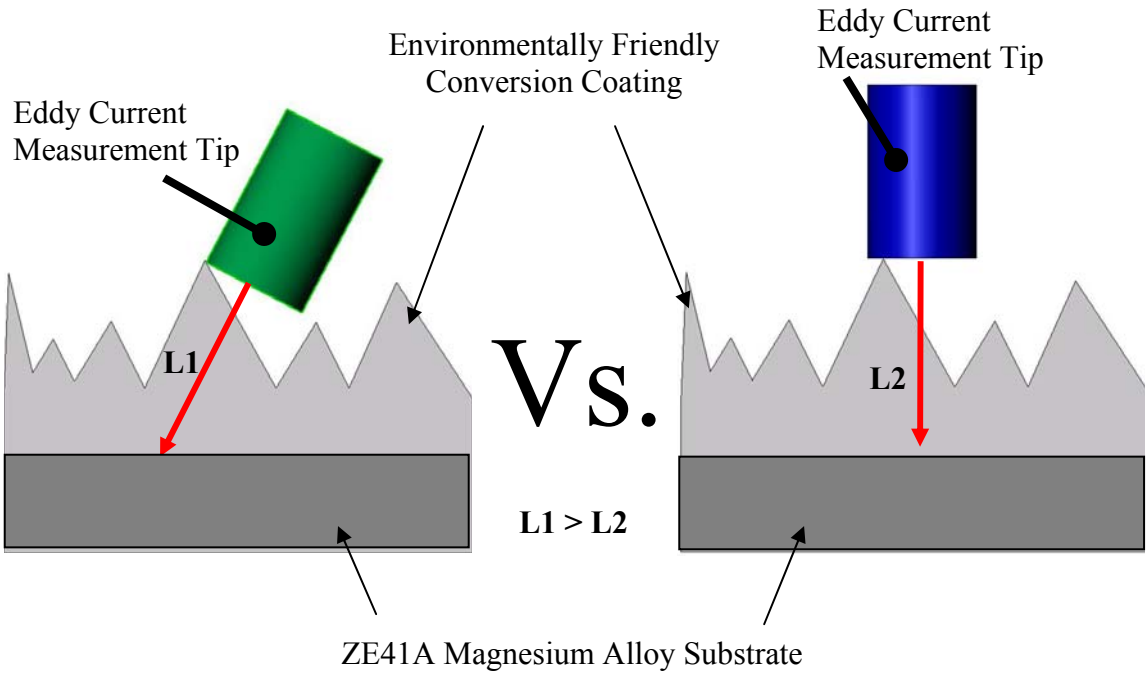

Figure 18: Scenario where the eddy current measurement tip may measure coating at an undesired angle. It should be noted that the coating height relative to the measurement instrument in this illustration is greatly enhanced.

Defelsko has considered this variable in the design of the Positest DFT and compensated for it by making a shoulder large enough for the instrument to rest at an almost perfectly parallel distance to the surface of the sample being measured. The error due to this scenario is negligible due to the ability of Defelsko's sholder diameter to span across many peaks as shown in the illustration in Figure 19.

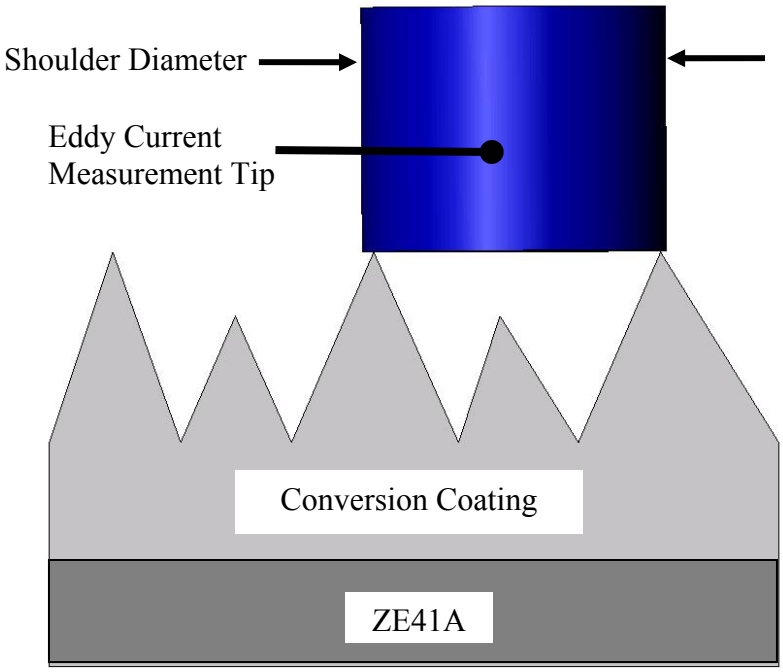

Figure 19: Illustration of eddy current measurement shoulder at the tip measurement area.

Profilometry

The next experiment performed to determine the environmentally friendly coating thickness is conducted using a Federal Surfanalyzer 5000 profilometer. A profilometer is used to measure the surface roughness or flatness of a sample by measuring the height change in a stylus tip which is pulled across the surface of the sample. The Federal Surfanalyzer 5000 has a resolution of approximately one micron.

Experimental Setup and Procedure

The sample must have a flat surface to interface with a granite block to obtain accurate results. The sample is placed onto a granite block surface underneath the stylus tip. The horizontal length of travel for the tip is positioned on the profilometer in the area of interest. The instrument is then calibrated by taking a reading of the desired area and

adjusting the mean value between ± 125 microns, ± 25 microns and ± 5 microns sequentially. The instrument is then ready for data acquisition.

Since this experiment is designed to only show roughness measurements i.e. changes in height of the sample, thickness measurements cannot be determined directly. To determine thickness measurements, an artificial "step" is created to show the elevation change between a coated surface and a non coated surface in the same sample. This step can be created by chemically etching a portion of the coating away from the ZE41A substrate. Therefore a step between a coated and uncoated area is created as shown in Figure 20.

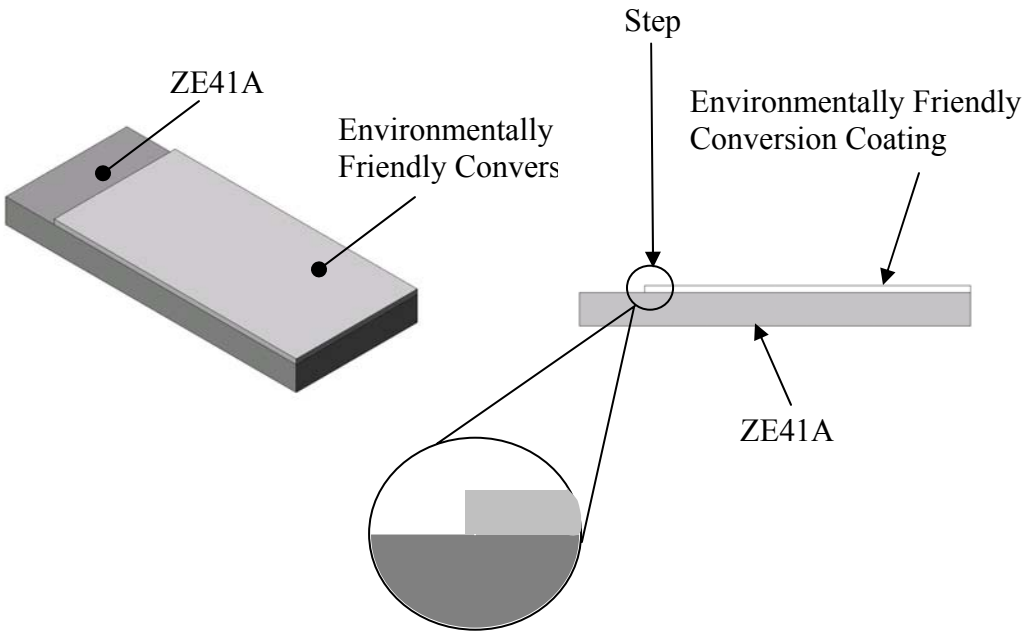

Figure 20: Illustration showing a step created by acid etching.

Most acids etch magnesium alloys with the exception of hydrofluoric acid.[9] Because of the difficulty associated in working with hydrofluoric acid an alternative means in producing this step is necessary.

Another method for producing this step is through a simple mechanical process. The step is produced by masking a piece of the magnesium alloy with masking tape and coating the entire surface of the sample, masked and unmasked in the usual form. The masked and unmasked regions of the sample are coated and illustrated in Figure 21.

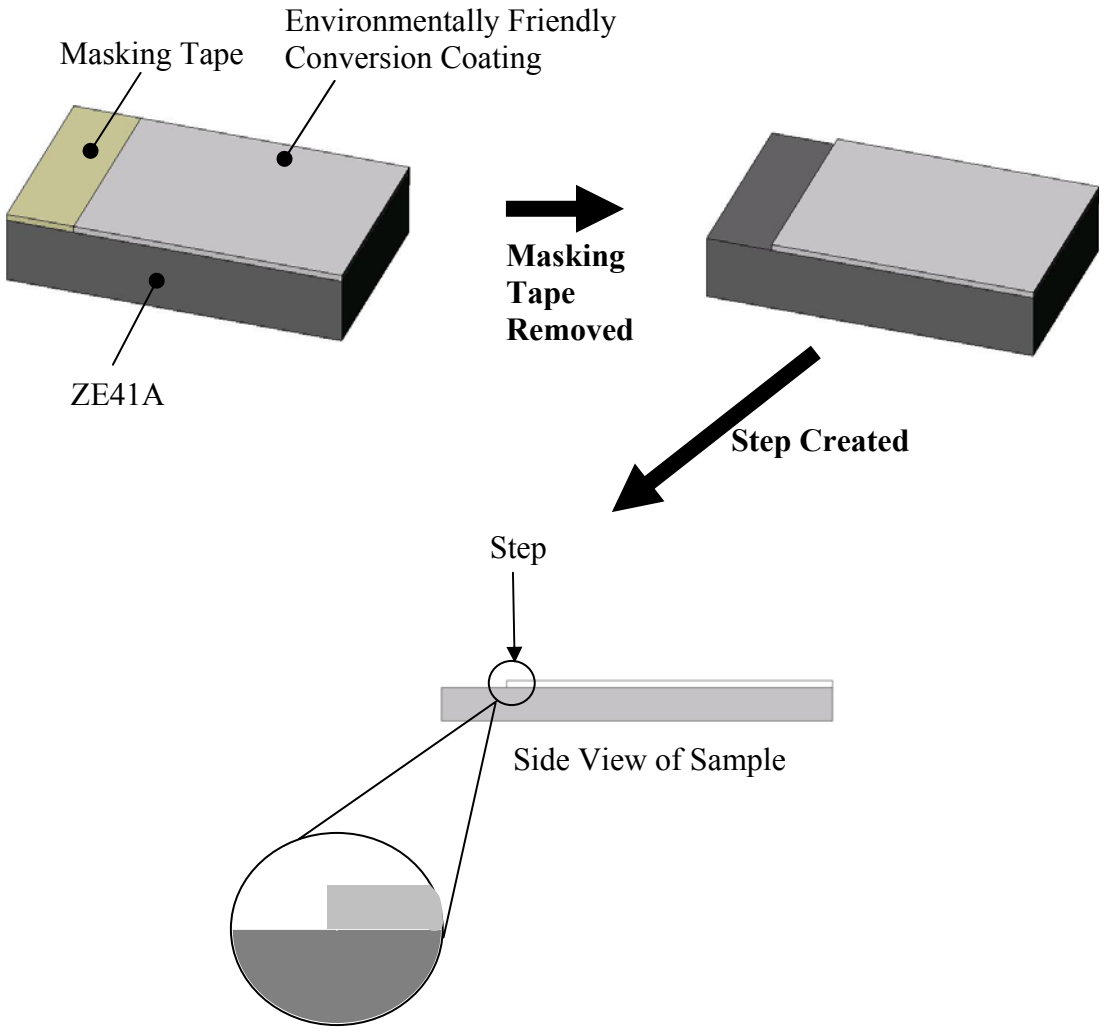

Figure 21: Coating on masked and unmasked regions of the ZE41A test coupon.

The transition between these two areas yields the step between an uncoated area and a coated area after the mask is removed. The profilometer tip is pulled across this step or transition and measurements are recorded. A step response in the data illustrating the coated to uncoated transition is expected.

Experimental Error

The variables in this experimental setup perceived to have an effect on the results of this experiment are: the coating step built up edge effect, flatness of the sample, resolution of the profilometer.

The coating step built up edge effect is a ridge of coating that could be built up on the tape that masks the area to remain uncoated during the coating process. This ridge of coating could solidify and act as an artifact in the profilometry measurement as illustrated in Figure 22. The possible error in the results due to this effect is not known.

The next possible source of error could be attributed to the flatness of the sample. Any variations in the sample flatness add or lessen to the effect of high or low points in the data. The measured root mean squared (RMS) value of the data for each sample is less than the largest step observed in the data indicating that sample flatness for each data set taken did not lead to error in the results.

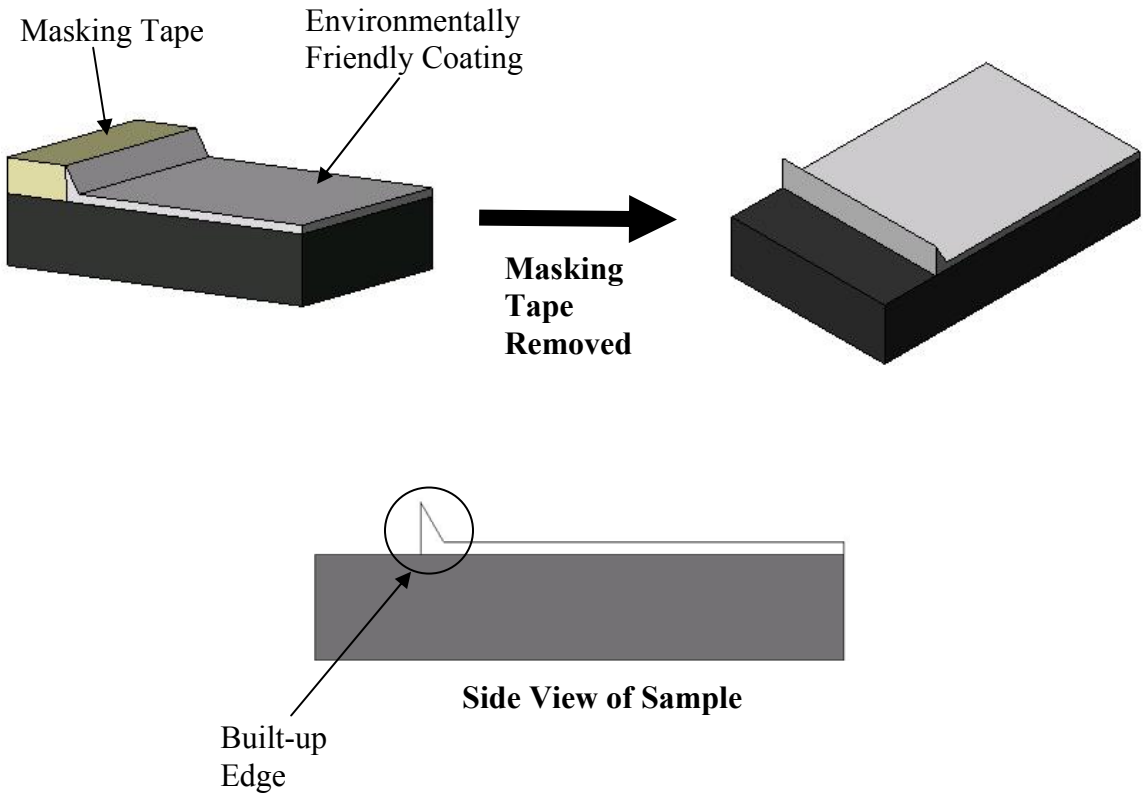

Figure 22: Illustration of a built edge due to coating a masked region and removing the mask.

The last possible source of error in this experiment is the resolution associated with the profilometry instrumentation. The resolution of the Federal Surfanalyzer 5000 is ±1 approximately micron. Since the expected thickness of the coating is between one half and one micron, the measurements are not expected to detect the step because it could appear to be noise in the data.

Optical Light Microscopy

Experimental Setup and Procedure

Reflected light microscopy is the first of two optical methods discussed for measuring the environmentally friendly conversion coating thickness. A Zeiss Epiphot

compound microscope is used in reflected light mode to evaluate the thickness of the coating by examining the cross-sectional view of the sample. The sample is cut so that the cross-sectional area of the coating is seen as shown in the Figure 23, Figure 24, Figure 25 and Figure 26.

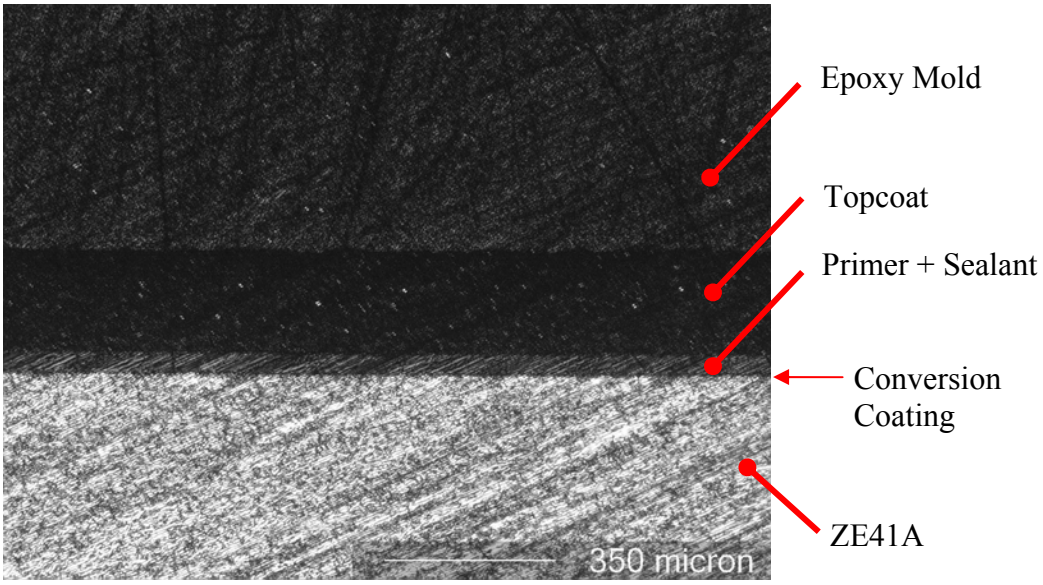

Figure 23: Image of the cross-sectional view of the corrosion protection coating system for ZE41A using a Zeiss Epiphot microscope with a 5X magnification, 0.1 NA objective.

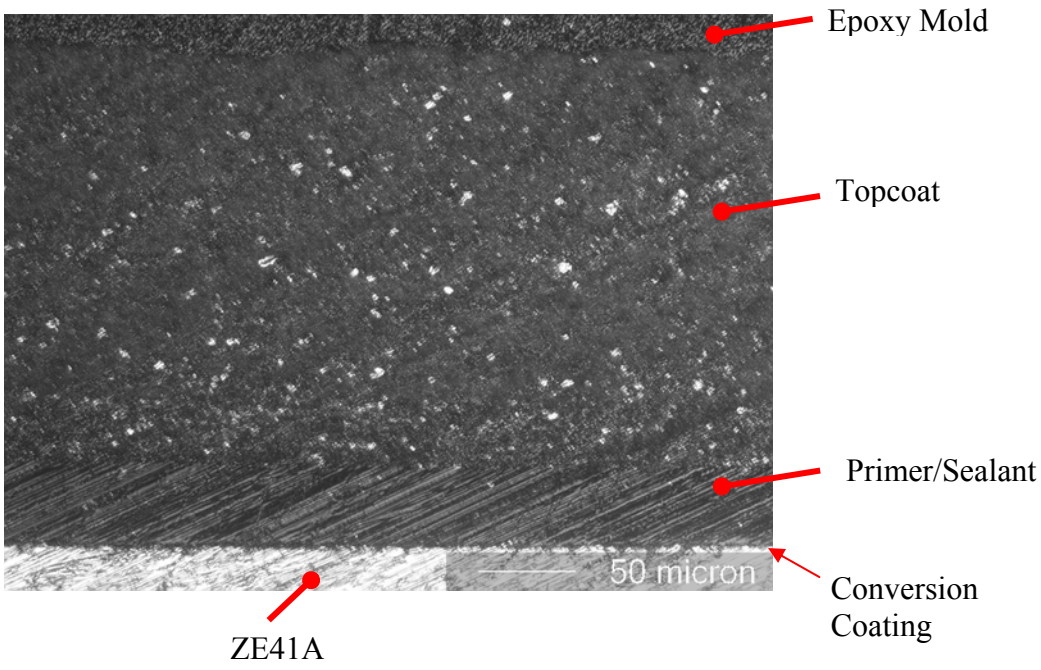

Figure 24: Image of the cross-sectional view of the corrosion protection coating system for ZE41A using a Zeiss Epiphot microscope with a 20X magnification, 0.40 NA objective.

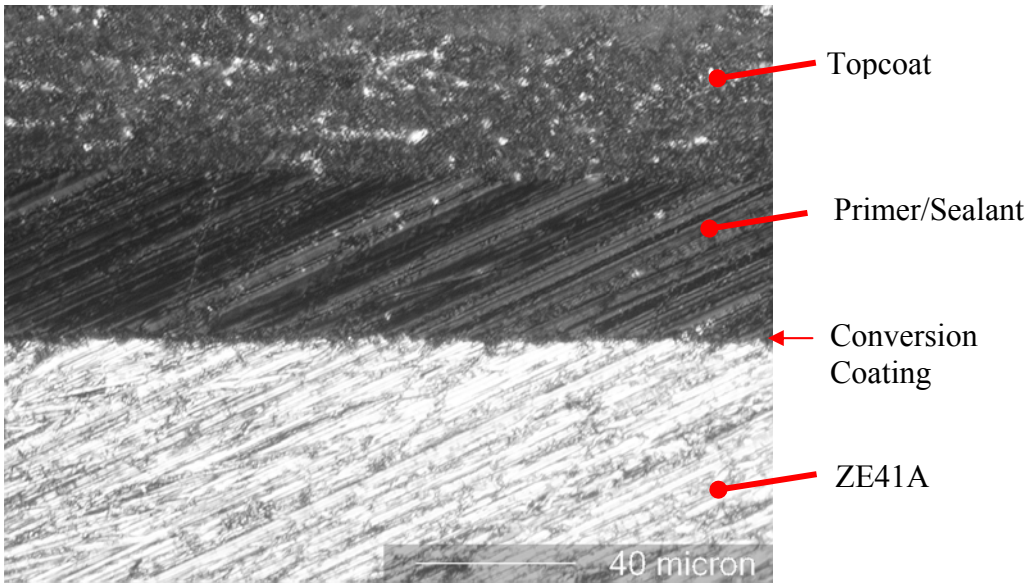

Figure 25: Image of the cross-sectional view of the corrosion protection coating system for ZE41A using a Zeiss Epiphot with a 40X magnification, 0.65 NA objective.

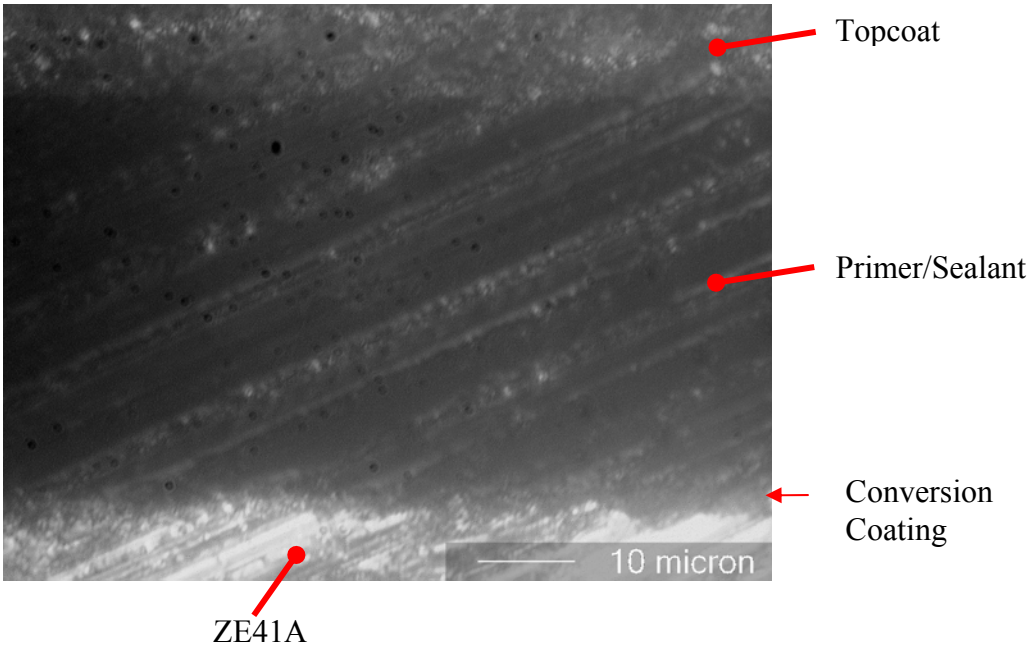

Figure 26: Image of the cross-sectional view of the corrosion protection coating system for ZE41A using a Zeiss Epiphot with a 100X magnification, 0.90 NA objective.

The sample is cut from a three by five by one quarter of an inch ZE41A test coupon. The rough cut of this test coupon is made using a Buehler Isomet Low Speed Saw. The sample is cut into approximately a one half by two by one quarter of an inch sample. A piece of cardboard is placed on top of the test coupon to ensure that the coating is not disturbed. The coupon is then placed into a Buehler Isomet Low Speed Saw with a diamond blade and cut into approximately a one half by one half by one quarter of an inch sample.

Experimental Error

The variables in this experiment arise from sample preparation and optical resolution. The diamond cut process for the unsupported coating produces a smearing

and crumbling effect. This effect tends to enhance or distort the cross-sectional structure of the coating. If cold mount is used to support the sample, it is possible to support the environmentally friendly conversion coating with the ZE41A substrate on one side of the cross-sectional interface but support is left to a porous epoxy filler on the other side of the interface as shown in Figure 27. The porous epoxy filler does not have the strength to support and prevent such a smearing effect from occurring.

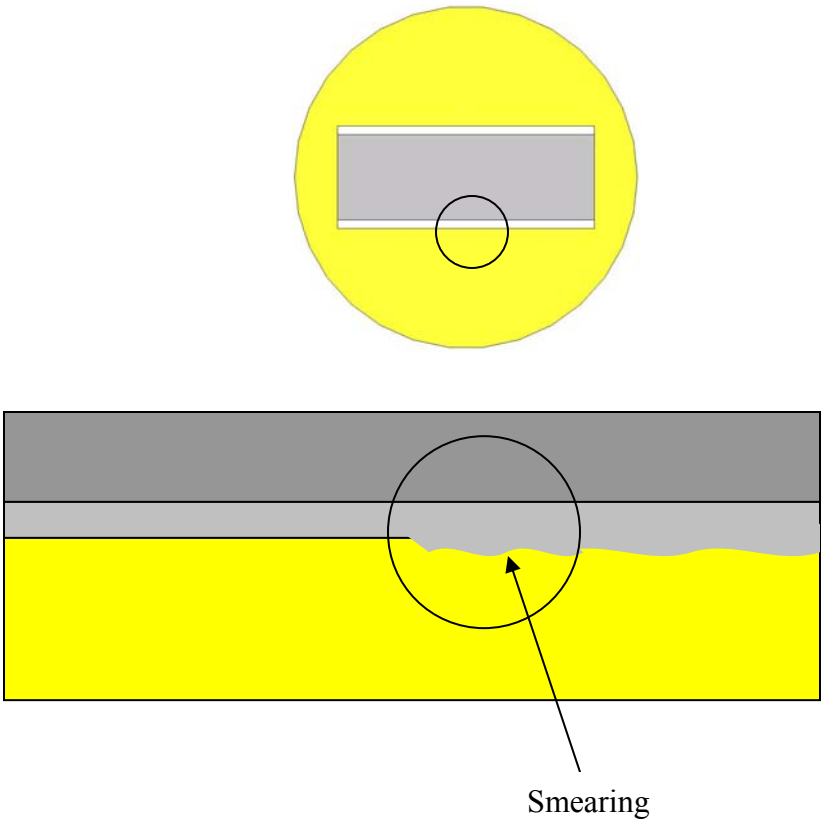

Figure 27: Illustration of smearing effect due to unsupported environmentally friendly conversion coating.

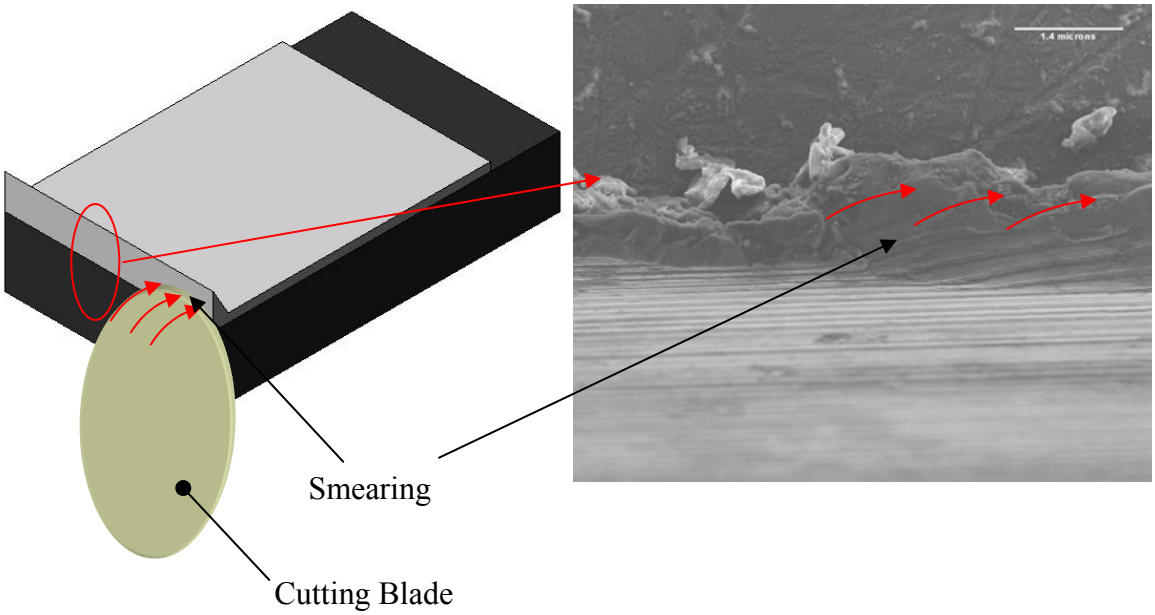

Figure 28: Figure of smearing effect observed in cross-section of ZE41A coated with the environmentally friendly coating in the un-mounted sample.

The second possible source of variables in results may occur from the resolution of the microscope. The resolution of the Zeiss Epiphot is limited to approximately 0.35 microns in the x, y plane with a 100X magnification and numerical aperture of 0.95 assuming that a 550 nanometer wavelength is used in the following calculation.

$$res = \frac{1.22 * \lambda}{2 * NA} = \frac{1.22 * 550nm}{2 * 0.95} = 353.15nm = 0.35\mu m$$

where,

λ = wavelength

NA = numerical aperture

Scanning Electron Microscopy

Experimental Setup and Procedure

Scanning electron microscopy is the first of two electron microscopy measurement techniques discussed in this document used to determine the thickness of the environmentally friendly conversion coating. A JEOL JSM-6400 is used to conduct this experiment. The basic principle behind a scanning electron microscope involves an electron beam directed toward the sample and the collection of inelastically scattered electrons. The electron beam in this case is directed toward the cross-sectional area in the same sample prepared for the light microscopy experiment.

Experimental Error

The same metallographic polishing technique is used and is exposed to the same possible error as in the light microscopy case, smearing or crumbling of the conversion coating. However, since the resolution limit of the JEOL JSM-6400 is less than 5 nanometers, resolution is not a cause of variability for this set of results. Photographs of the experimental setup and sample in the sample holder are shown in the Figure 29 and Figure 30.

Figure 29: JEOL JSM-6400 scanning electron microscope.

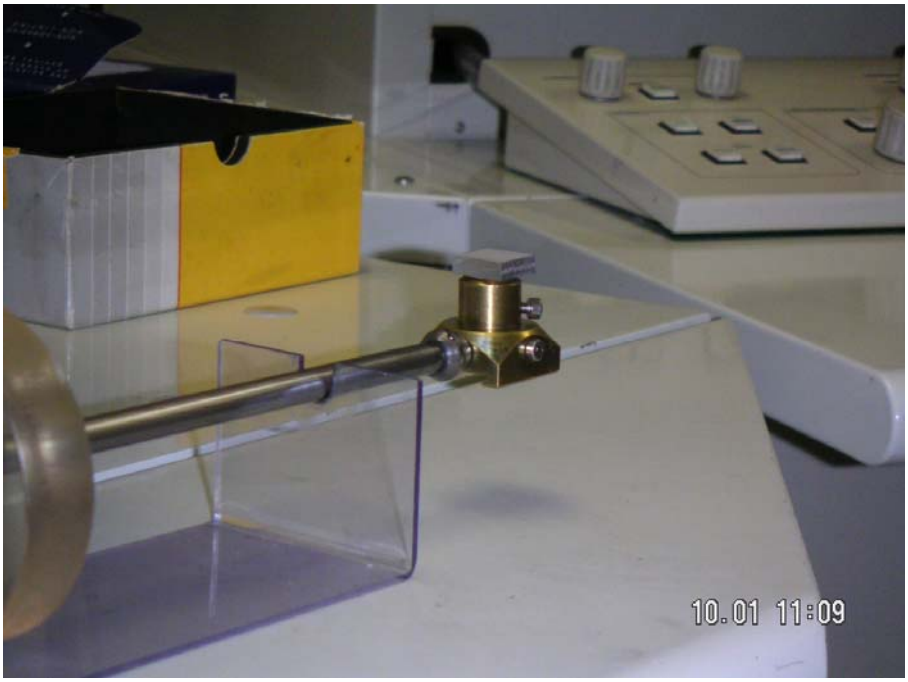

Figure 30: JEOL JSM-6400 sample holder with sample.

Transmission Electron Microscopy

Experimental Setup and Procedure

The transmission electron microscope used for this experiment is the JEOL 2010 TEM operating at an accelerating voltage of 120 volts. The TEM electron gun assembly directs electrons toward the sample and collects elastically scattered electrons passing through the sample on a fluorescent screen. The sample in this case must allow the passage of electrons so must be very thin. The cross-sectional area of this sample must also be examined. In this case, a traditional known sample preparation technique must be used due to the configuration of the TEM and is illustrated with the following sequence of figures in Figure 31 and Figure 33. Figure 33 (a) shows two samples of the environmentally friendly coated ZE41A being joined together with Varian Torr Seal Epoxy. The two samples are joined together such that the coating is joined to itself between the two ZE41A substrates in a ZE41A coating sandwich. The sandwich is then machined into a cylinder using a 120V, 4.5 amp Black & Decker power drill providing circular motion to the piece and a Dremel Multi Pro model 395 power rotary to aid in cutting. The Dremel cutter used in the Dremel Multi Pro model 395 is a Dremel #115 cutter. After the cylinder is machined into a diameter of that fits the inner diameter of a standard steel sleeve specimen with a diameter of approximately three microns, it is placed into the sleeve and held in place with Varin Torr Seal epoxy. The length of the cylinder machined must be long enough for the user to handle with ease, at least one quarter of an inch. The steel sleeve/cylinder assembly is then sliced into thin sections with a Buehler Isomet 1000 diamond saw cutter as shown in Figure 31 (c). Next, these sections are made into thinner sections through polishing with a Buehler Ecomet 3

polisher, dimpled at the center with a Dimpler Model D-500 and ion milled at the center with a Fishion Low Angle Ion Milling Machine. The thinning procedure makes the sample thin enough for an appropriate dimple to be made. The dimple is necessary to thin the center of the sample so that an ion mill may penetrate and produce a hole at the dimpled area which is the center of the sample. These results are shown in Figure 31 (d). Because the TEM samples are difficult to machine in reality, an alternate method for preparation is needed. The most difficult portion of the ideal sample preparation outlined in Figure 31 is step (b). Difficulty in machining a cylinder formed from two samples pressed together and joined by epoxy as shown in Figure 31 (b) is the most difficult procedure due to the complexity of machining a long slender cantilever beam scenario with a less than three millimeter diameter. An alternative method for obtaining a sample that fits into a steel sleeve with approximately three millimeter inner diameter is developed and shown in Figure 33. The only difference in the sample preparation sequence between those shown in Figure 31 and Figure 33 is step (b). In Figure 33 (b), the sample is machined into a rectangle with the longest length of one side of the cross-sectional face being less than three millimeters as shown in Figure 32. The processes to follow the alterative step in Figure 33 (b) are the same as the steps shown Figure 31 (c) and (d).

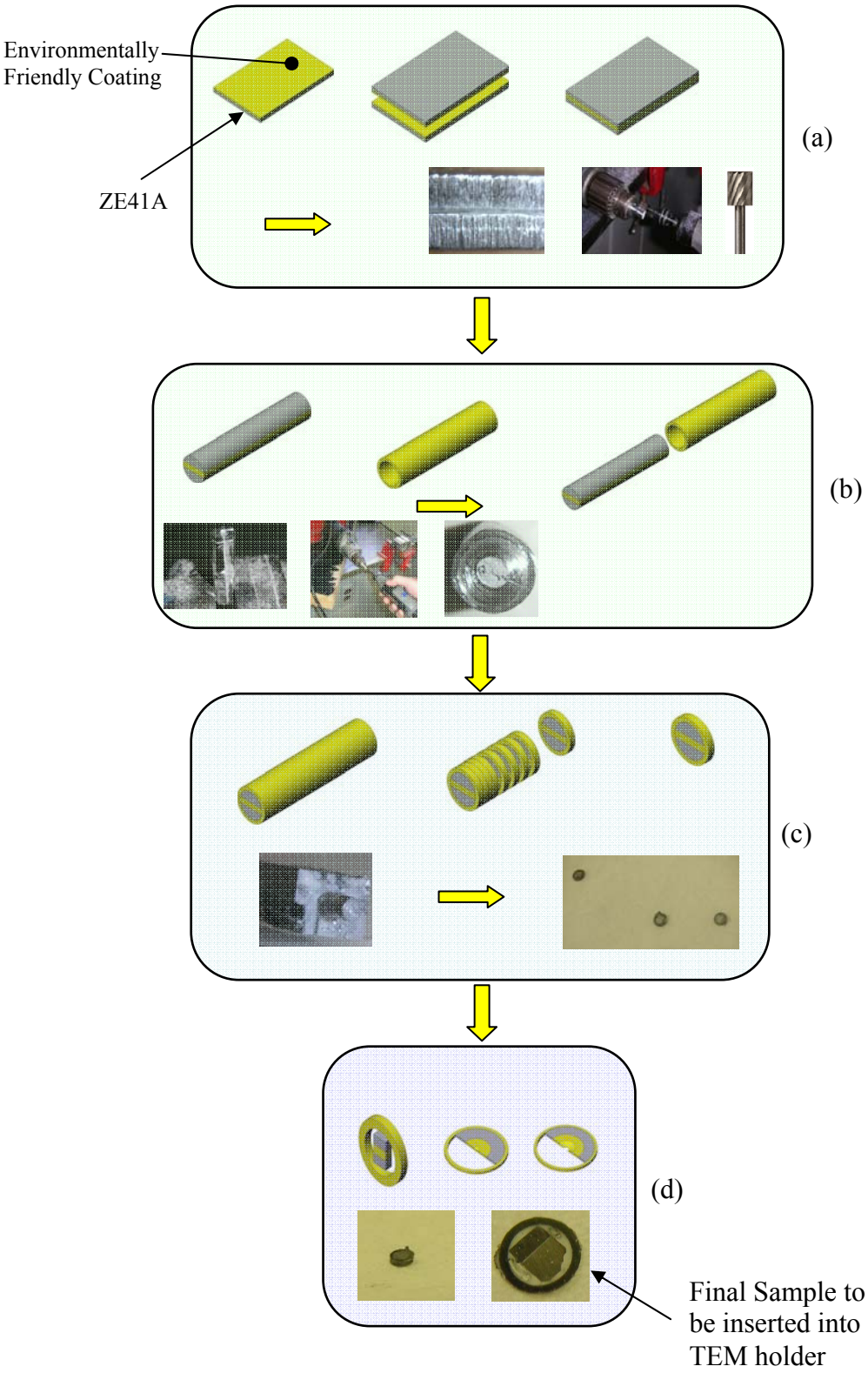

Figure 31: Ideal sample preparation sequence for thin film TEM samples.

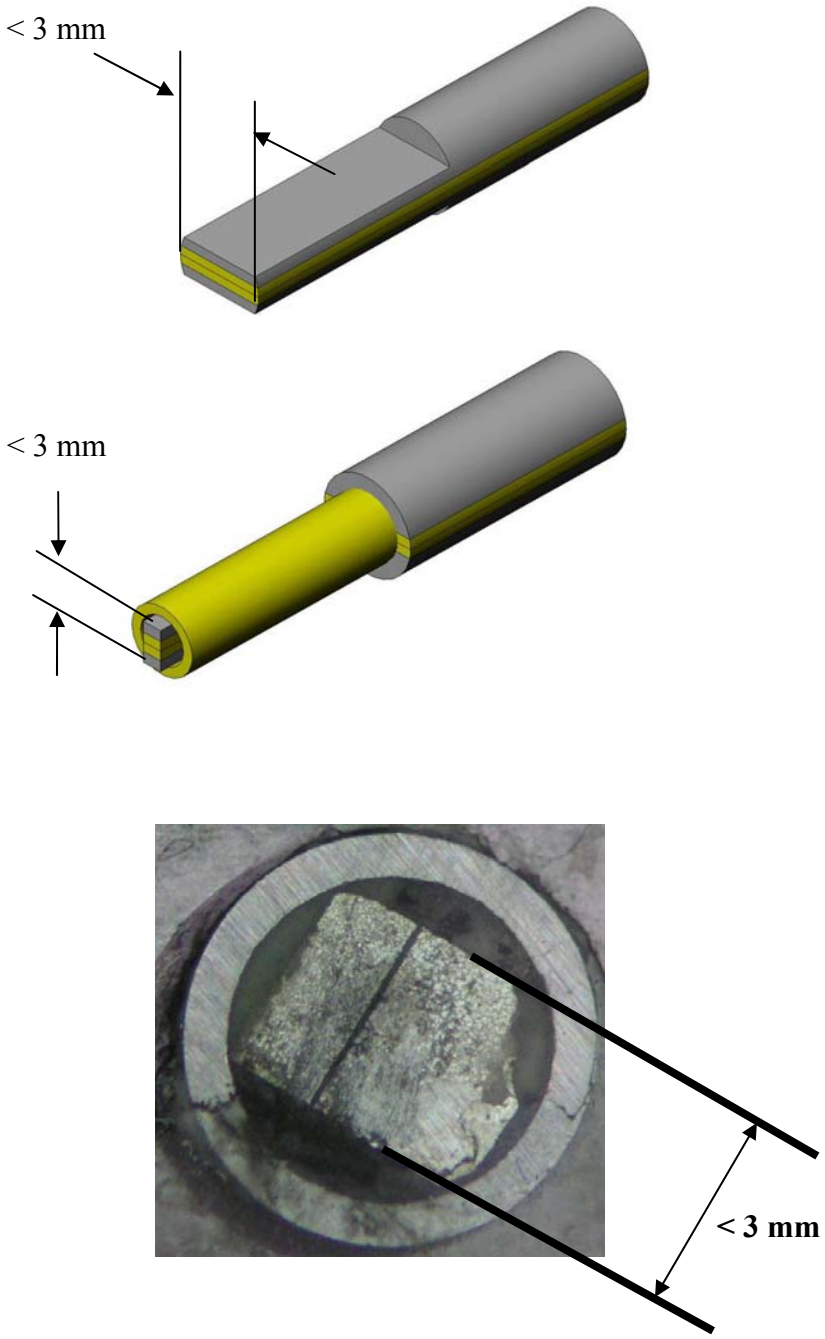

Figure 32: Illustration and image of sample machined into a rectangle with its longest side measuring less than 3 mm.

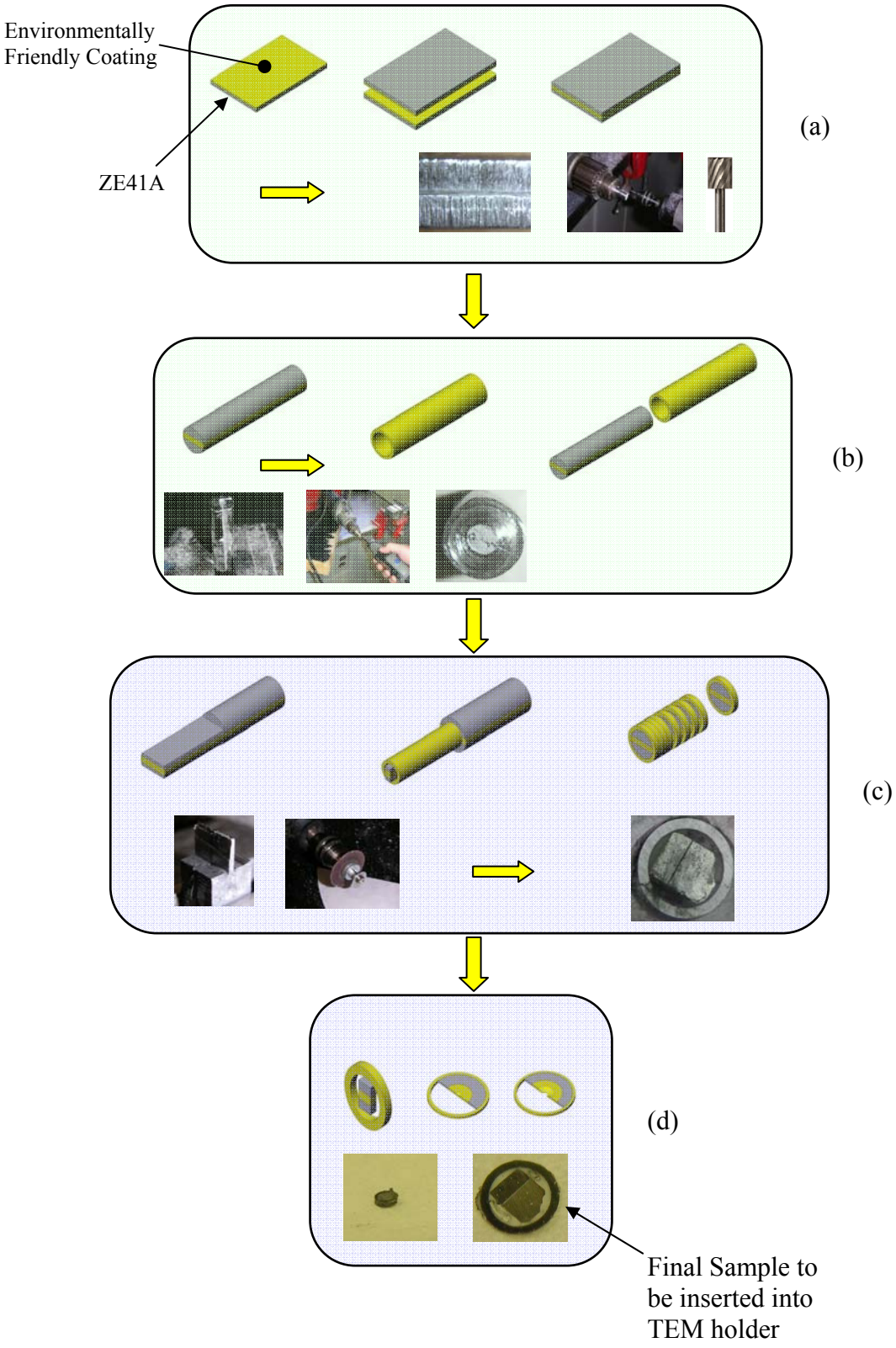

Figure 33: Actual sample preparation technique for coated ZE41A TEM sample.

Experimental Error

Because the sample preparation in this experiment is complicated and must be prepared with great precision for significant results there are only small sources of possible error in the results due to sample preparation. One key area to be addressed for possible concern is the step where the joined sample shown in is machined into a square as shown in Figure 33 (c). If the block is machined improperly, Figure 34 shows that the wrong region of interest on the sample can be machined with the ion mill.

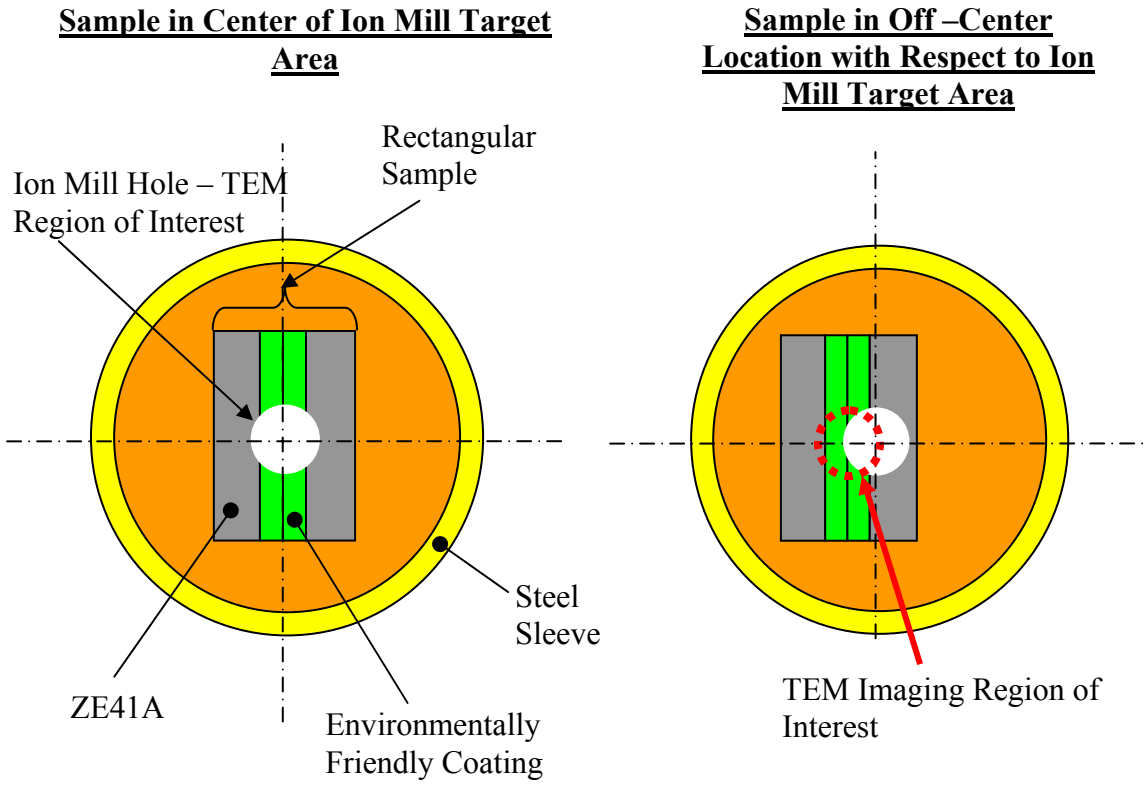

Figure 34: Cross-section view of off-center sample yielding possible error in TEM image region of interest.

The possible end result is that a hole is not machined in the center of the sample, but in an off-center location. If this occurs, the correct region of interest may not be imaged and false results are possible.

The second source of possible error in the experiment is chemical identification. When gathering chemical information for the sample using the JEOL 2010's EDS system, the EDS detector failed. Chemical identification and more data is attempted in a subsequent session but did not prove to be useful as the sample oxidized in the five month repair period of the detector. Therefore, no chemical information is provided for this sample. This may leave room as error in the interpretation of these results.

Confocal Microscopy

Experimental Setup and Procedure

The confocal microscope used in this experiment is the Olympus FV1000 confocal microscope. In general, a confocal microscope operates on the principle of monochromatic laser emission from an external light source onto the sample where a detector receives reflected or transmitted light depending on the sample examined. In many cases photo multiplier tubes, gather photons that can be processed into an image. The confocal microscope is useful when scanning the surface topology of a sample, in this case, the step referenced in the profilometer experiment. The confocal microscope is used to scan the surface of the environmentally green conversion coating and the surface of the non coated ZE41A. Both the uncoated and coated conditions exist on one sample to provide a step as noted in the profilometer experiment. However, the sample preparation technique used in this differs from the profilometer experiment in that the coating is removed from one portion of the coated sample through mechanical polishing

using an abrasive Scotch Brite pad. This modification is made to prevent the built up edge effect as a variable in experimental results described in the profilometer experiment.

Half of an approximately two by three by one quarter of an inch sample is covered by another sample of a similar size. While being held into place on a table, The uncovered portion of the sample is mechanically polished by hand using an abrasive Scotch Brite pad until the coating appears to be completely removed from the ZE41A surface. This removal technique is recommended by the coating developer as a sufficient means of coating removal.

The sample is cut into a smaller size approximately one half by one half by one quarter of an inch. This sample is then mounted onto a slide using crystal bond so that it can be placed in a hanging position for the confocal microscope stage as shown in the Figure 35.

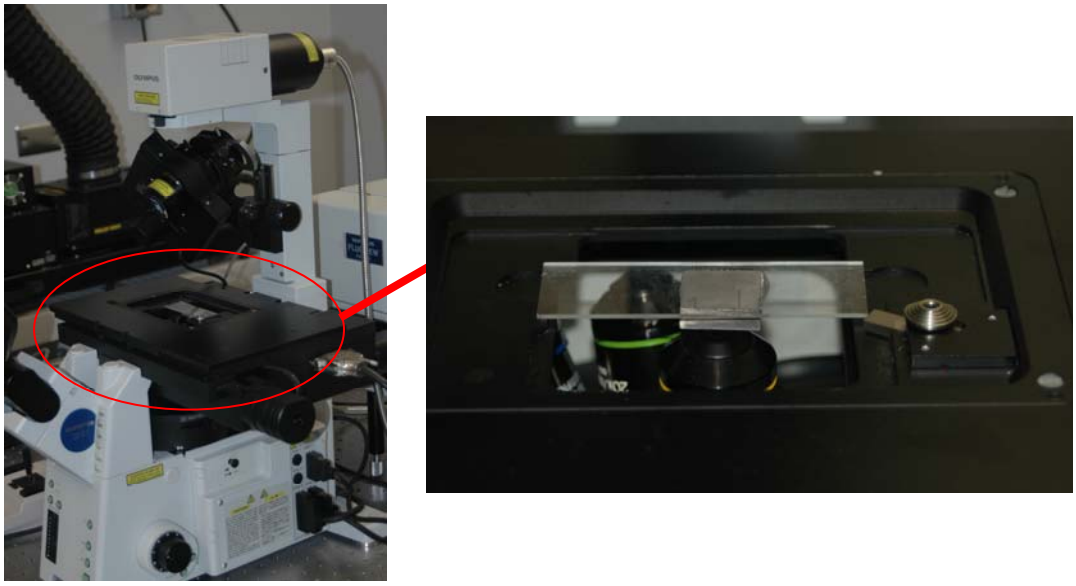

Figure 35: Sample mounted on slide using Crystal Bond shown in hanging position for confocal imaging.

This sample is then scanned using the 488 nanometer wavelength laser. To develop the surface topology measurements, an initial axial coordinate is chosen at the lowest focal point of the sample. A final, stopping point axial coordinate is chosen at the highest focal point of the sample. The confocal microscope then steps from the initial point to the final point in three micron increments. Three micron steps were chosen because this is the axial resolution for the Olympus FV1000 confocal microscope with a 10X magnification objective and 0.4 numerical aperture. The surface is scanned in both the lateral and axial directions to produce a three dimensional image with axial or depth information.

Experimental Error

The variables that existed in this experiment reside in sample preparation, flatness of sample and resolution of the confocal microscope. The sample preparation variable in this case lies within the bonding technique used to attach the sample to the glass slide. Crystal bond is heated and melted between the glass and the ZE41A sample for adhesion. However, constant pressure is not applied in squeezing the ZE41A sample and glass slide together until the crystal bond is almost completely cured. Pressure is applied in squeezing the sample and glass slide together for less than a minute. This could cause error in the results by creating an angle α between the glass slide surface and ZE41A sample as shown in Figure 36.

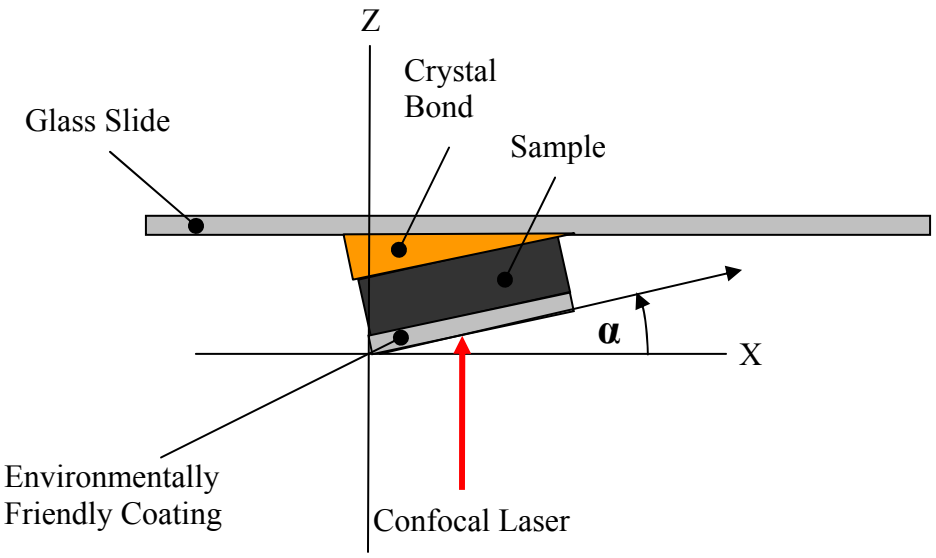

Figure 36: Cross-sectional illustration of glass slide and sample showing possible error in depth information (z-direction) from confocal microscopy image due to angle created by crystal bond.

This angle could reflect a false height change in the surface of the sample in the z-direction since the step created in this case is more of a gradual change between the coated and uncoated area of the sample.

The second source of error in this test originates from the flatness of the sample. Data was not recorded regarding the flatness of the sample. If the flatness of the sample varies more than the expected height change between a coated and non coated area on the sample, approximately 0.5 microns, then this factor could significantly affect the results.

The third source of possible error arises from the resolution of the Olympus FV1000 confocal microscope. The axial resolution of the Olympus FV1000 confocal microscope with a 10X magnification objective and 0.4 numerical aperture is approximately 1.48 microns. Since the expected range of the environmentally friendly conversion coating thickness is approximately 0.4 to 0.6 microns, aliasing is a concern

for the results of this experiment and is therefore labeled as a possible source of error in the results.

Coverage

Finding surface coverage area for a coated sample requires a different set of experiments to be performed. Finding the surface coverage area for this coating involves measuring areas were coating is exists on the ZE41A sample surface and areas where coating does not exist on this same surface. There are two schools of thought for measurement acquisition in this task, macroscopic vs. microscopic measurement. In the first case, macroscopic measurements are taken over relatively large areas so that the more amounts of data can be collected when compared to smaller sample collection areas. In microscopic measurement, less data is collected because the data collection area is confined to a smaller area when compared to macroscopic measurement. Macroscopic measurement is beneficial in that more data is collected. However, macroscopic measurement can also be unproductive in that more sources of error causing a less clear data set can occur when compared to a smaller sample size. Microscopic measurement can be beneficial in that small data sets can lead to less sources of error. Microscopic measurement can also be more specific and preferred when a controlled test with many variables exist. However, microscopic measurement can also be unproductive in that less data is examined and therefore less of a trend might be detectable. Both macroscopic and microscopic measurement techniques are used for the evaluation of surface coverage area.

In accordance with the macroscopic school of thought, a general observation of the environmentally friendly coating on the ZE41A surface shows the coating appears to

be fairly visible. That is, an uncoated surface is distinguishable from a coated surface. The coating appears to give a white to gray appearance and is distinctly different from the shiny metallic surface of the uncoated ZE41A. However, the coating also seems to appear to contain patches that indicate that the coating is not uniform. Some areas seem to be lighter than others. In some cases, the brushing process that is used to apply the coating can be seen in terms of streaking patterns. The coating appears to be intact but also appears to be non uniform. The non uniformity seems to occur because of the way light interacts with the flat sample surface. At a macroscopic scale, it is difficult to determine that light interaction is the only cause of this non uniformity. However, because no other source of non uniformity such as visible change in coating thickness or changes in surface roughness are noticeable through sight or touch, optical properties of the coating are examined more closely.

Each experiment performed in the coverage section uses three samples prepared specifically for these tests. The samples are ZE41A magnesium samples coated with the environmentally friendly coating. Each sample is coated with a different condition of the coating. The first sample is coated with “light” coat, the second with a “partial” coat and the third with a “heavy” coat of the environmentally friendly coating. These three coating conditions were determined through experience with the coating. Mass compositions of the components in these coatings may not be exactly the same amounts used in the initial coating measured in the thickness section of this paper. The parameters to yield these three different conditions are not known but the resulting conditions are the most important factor and are determined by the coating developer through experience with this coating.

These three samples are initially in approximately three by five by one quarter to one fifth plates received by the coating developer. They are then machined using a Bridgeport Mill into smaller sizes replicating slides used in a microscope so that they can also be used in each microscope system with minimal compromise to depth of focus and magnification. The heavily coated sample is machined to the dimensions seen in the Figure 37.

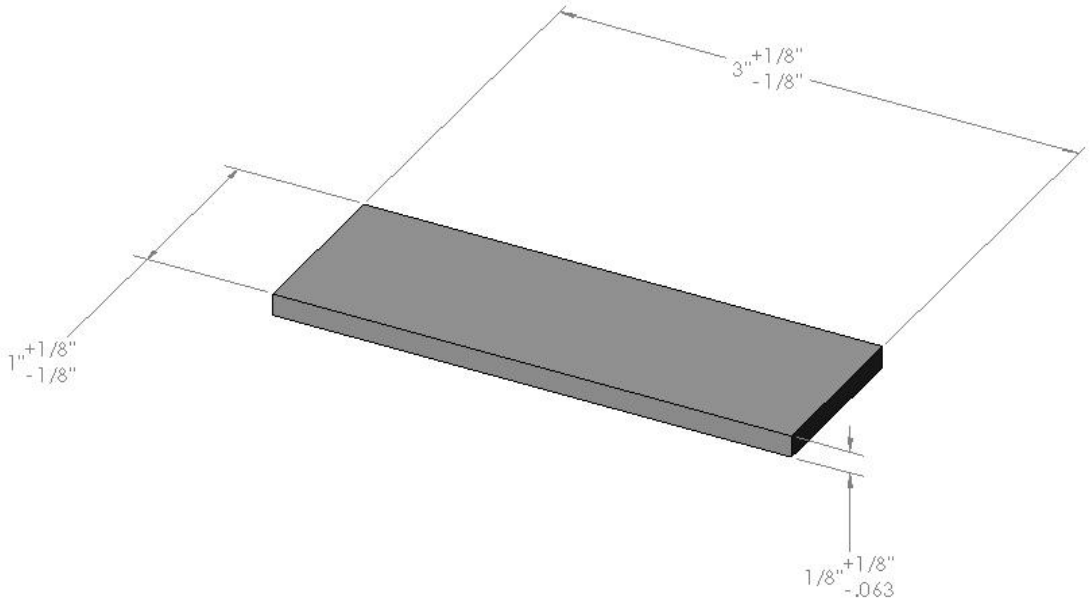

Figure 37: Machined sample dimensions for heavily, partially and lightly coated ZE41A to be used in coating coverage experiments.

Since the samples are so thin, machining is difficult and residual stress due to uneven heating is a problem. Each sample is originally designed to be machined within 0.005 inches, but the tolerance became relaxed as the physical limitations of machining such a piece becomes apparent. A representation of one of the most important dimensions, the cross sectional dimension is associated with each dimensional drawing to

show a more accurate representation of the resulting machined sample. The partially coated sample is machined to the dimensions shown in Figure 37. The lightly coated sample is also machined to the dimensions Figure 37.

The cross sectional errors are noted and discussed more thoroughly in the results and discussion section of this document. Figure 11, Figure 12 and Figure 13 show the areas chosen at random to be sampled by each of the tests. Ten areas per sample are selected and marked with pencil and noted. All ten areas on each sample are used for the polarized light microscopy experiments. Three sample areas for each sample are measured for the infrared proximity sensor, FTIR and Raman experiments for practicality in data collection. These areas are: lightly coated sample areas 7, 1, 3, partially coated sample: areas 1, 2 , 3 and heavily coated sample: areas 1, 10 and between areas 4 and 8. The sample areas are chosen at random.

Infrared Proximity Sensor

Experimental Setup and Procedure

The first optical technique arises through an observation in an unrelated project using an infrared proximity sensor. The Sharp GP2D12 infrared proximity sensor is typically used to measure the distance of an object from the infrared sensor. The sensor contains an emitting diode and a position sensitive diode (PSD) for detection. The emission wavelength of the diode is 850 ± 70 nanometers[19]. The IR proximity sensor is used in conjunction with a PIC16f877 and Microchip 2840 development board. The analog signal produced by the IR proximity sensor is processed into a digital signal by the Microchip PIC16f877 and sent via RS232 to a computer where the data is displayed continuously as live data on the monitor. An observation using this sensor shows that a

difference in digital output between a coated and uncoated surface exists. Since the PIC16f877 has a 10-bit analog to digital conversion capability, the digital output is displayed with a number from 0 to 1024. This corresponds to a voltage between zero and five volts. A precision test setup is designed and built to mount the sensor, coated and uncoated samples. This experimental test setup is designed as frame to perform controlled experiments and is shown in the Figure 38.

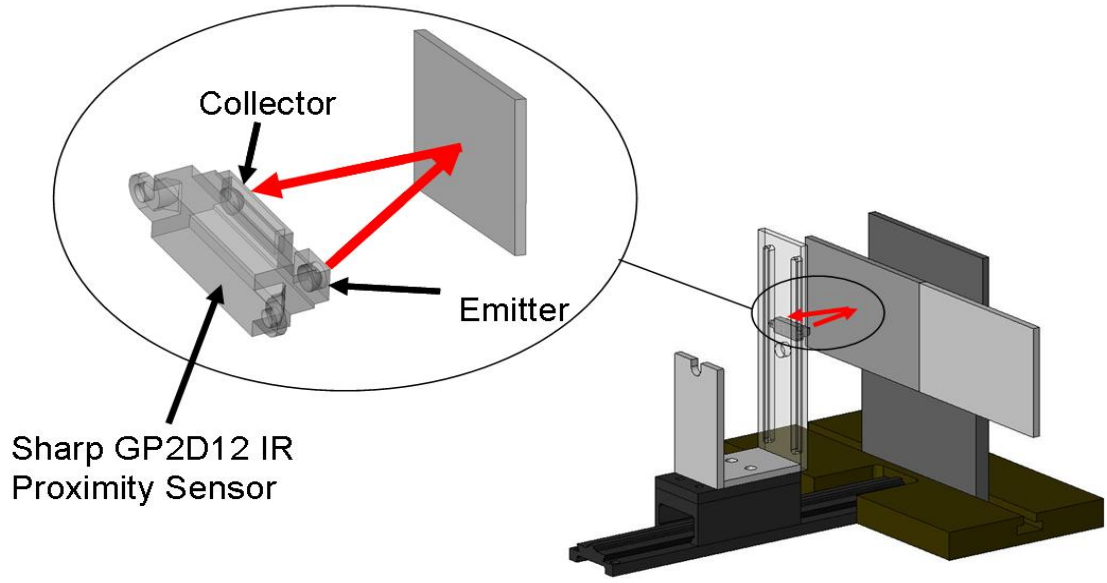

Figure 38: Test fixture assembly used for Sharp GP2D12 IR proximity sensor experiments.

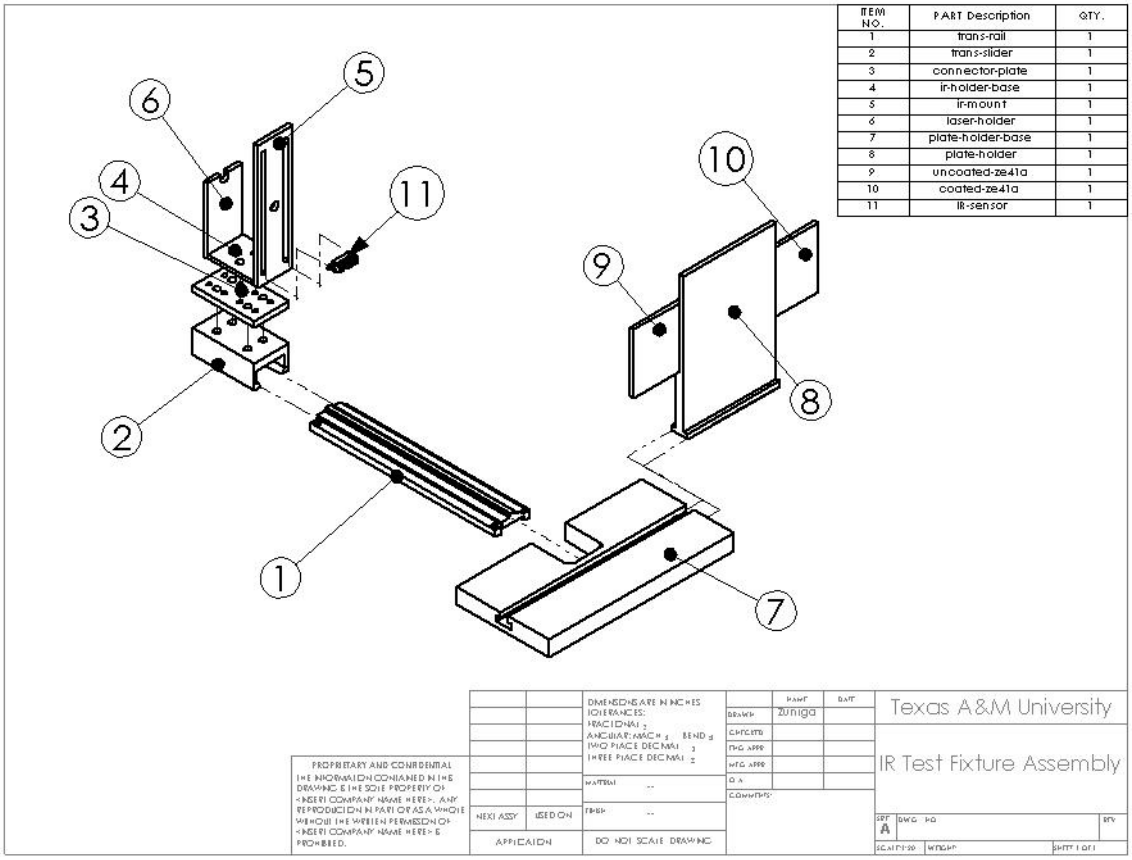

Figure 39: Test fixture exploded view.

There are a few key parameters that must be controlled when designing this experiment based on the two featured components of this experiment, the Sharp GP2D12 IR proximity sensor and the ZE41A test coupons coated with the environmentally friendly coating and uncoated ZE41A test coupon. The Sharp GP2D12 IR proximity sensor must be able to record measurements for each test coupon, coated and uncoated with the same testing conditions for controlled experimentation purposes. The sensor must remain parallel to the measured surface of the test coupon in the x and y directions as shown in Figure 40.

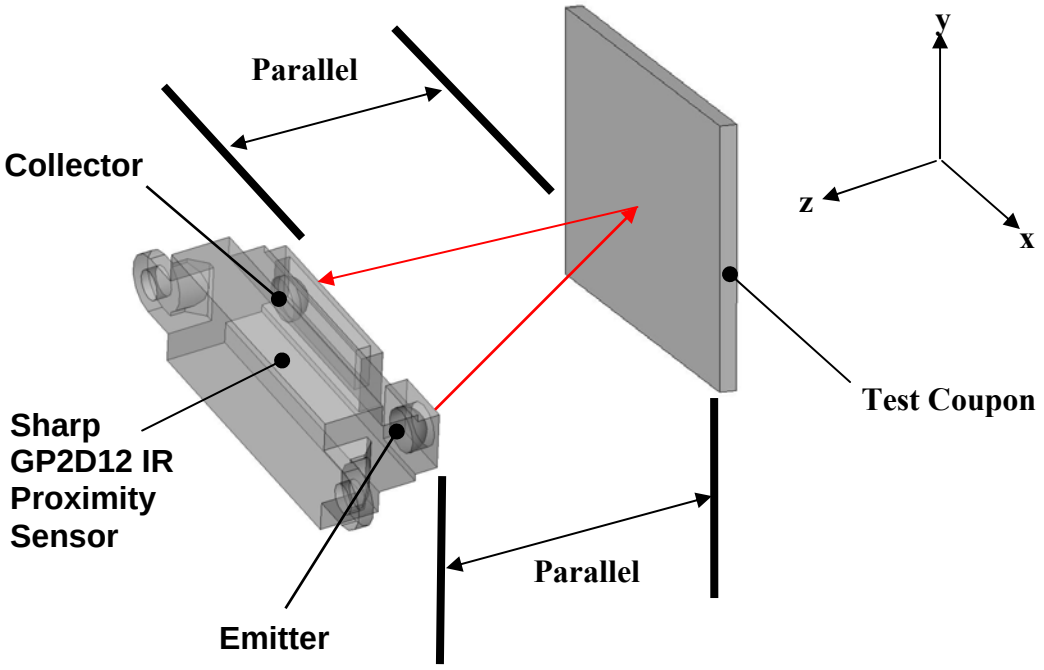

Figure 40: Illustration of parallelism to be maintained between the Sharp GP2D12 IR proximity sensor and sample.

The next important parameters to be controlled is the height of the sensor relative to the test coupons in the x, y and z directions marked in Figure 40. These parameters must be controlled and measurable. The parameters listed below are designed to be varied in a controlled and known fashion so that a controlled experimental (varying one parameter at a time) can be accomplished with the test frame shown in Figure 38.

- Parallelism between the IR proximity sensor and plate holder
- Height of IR proximity sensor
- Height of sample being examined
- Horizontal position of the sample

- Vertical Position of the sample
- Angle of the IR proximity sensor
- Distance between IR proximity sensor

To control the parallelism between the IR proximity sensor and plate holder, several factors are considered. One of the main factors is flatness of the plate holder. The plate holder must remain flat so that an unknown and uncontrolled angle between the plate holder and IR proximity sensor is not created. If an angle in due to a non flat surface on the plate holder exists, an unknown parameter is introduced into the experiment. To ensure that the plate is flat, the plate is first milled using a Bridgeport Textron Mill with a surface cutting operation that would keep the plate holder holding area to within five thousandths of an inch. The plate holder holding area is then ground to produce a smooth and even surface finish. As a quality check of flatness, a three point measurement setup is conducted. In this quality check, the plate are of interest (the holding area) is supported by three mechanical stands. These stands are positioned at the same height within one thousandths of an inch and are placed on top of a granite slab machined with high tolerances for flatness and roughness to ensure no sloping exists from the test setup. The height of the plate is measured at four different locations one at each corner of the plate while it is being supported by the stands as shown in Figure 41.

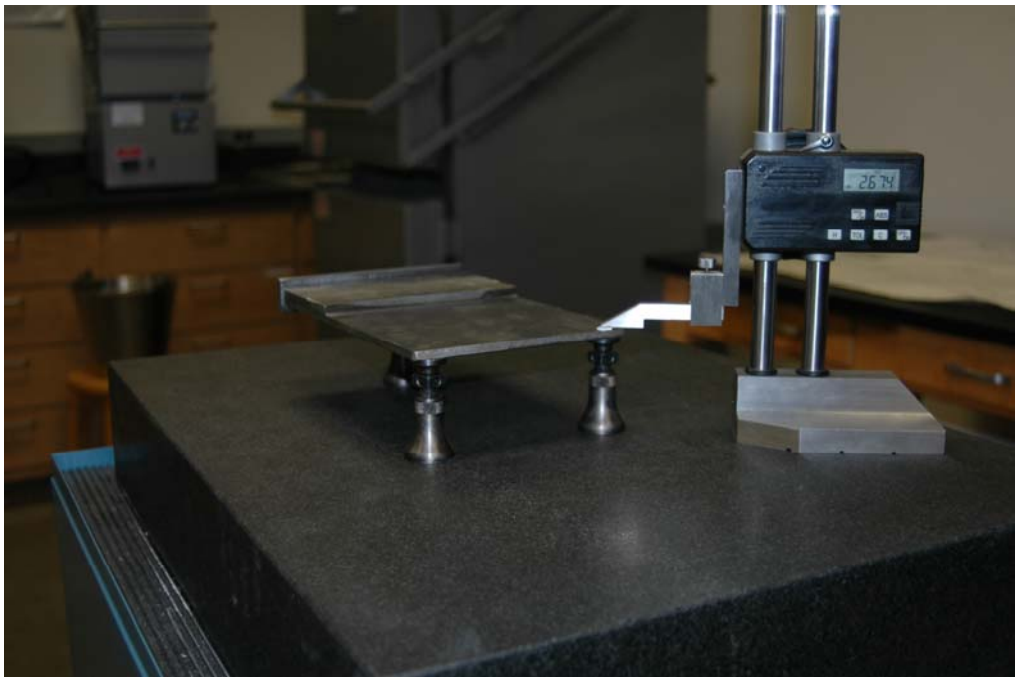

Figure 41: Photo of plate flatness measurements using linear height scale, granite block and calibrated stands for the test fixture plate holder piece.

The heights at each corner and the center are recorded and a map of the data is shown in Figure 42. The maximum change in height recorded is four thousandths of an inch giving a slope at a maximum of four thousandths of an inch over approximately five inches.

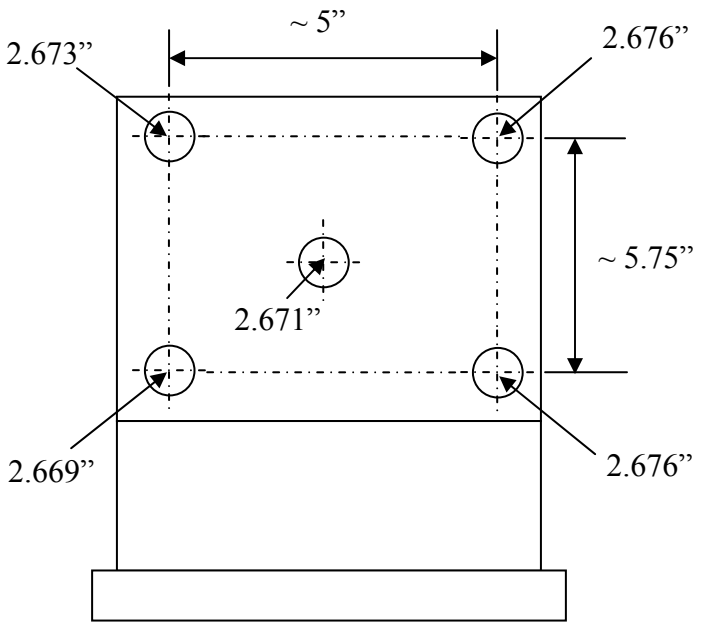

Figure 42: Top view sketch of plate holder measurements recorded for determining flatness of plate holder piece.

The flatness of the aluminum plate holding the IR proximity sensor is machined in the same manor with less variation in the x direction due to less machining operations and surface area.

Both the IR proximity sensor holder and sample holder are flat and have known variances in flatness so the parallel parameter is checked using a dial indicator to measure the effect of these small variances within one thousandths of an inch. The dial indicator is positioned orthogonally to the plate holder holding area back as shown in the Figure 43.

Figure 43: Quality check testing error in orthogonal distance between the IR proximity sensor and plate holder piece.

The plate holder is then pushed in the positive and negative x directions so that measurements of the dial indicator can be recorded. One of the larger errors in this test frame is measured in this quality check and is discussed in the experimental error section.

The next parameter controlled in the test frame is the height of the IR proximity sensor. The height of the IR proximity sensor is controlled in the z direction shown in Figure 38 by moving the sensor along the slots machined in the IR proximity sensor holder and fastening the two set screws joining the IR proximity sensor to the IR proximity sensor holder. The test frame allows movement in the z direction while keeping the x and y directions fixed. The IR proximity sensor height can be varied within any desired position between a height of half of an inch to seven inches relative to the bottom of the front face of the IR proximity sensor holder.

The IR proximity sensor projection on the plate is determined by placing a sheet of paper on the sample and moving the sheet of paper in the beam path until the digital output on the PC monitor changes when the linear track is positioned at 0.9 inches. When the digital output changes, the beam path has been breeched and one boundary of the beam projection onto the plate holder is determined. This procedure is repeated to find the x and y boundary for each side of the sensor projection. The emitted beam projection onto the sample is illustrated in the following Figure 44.

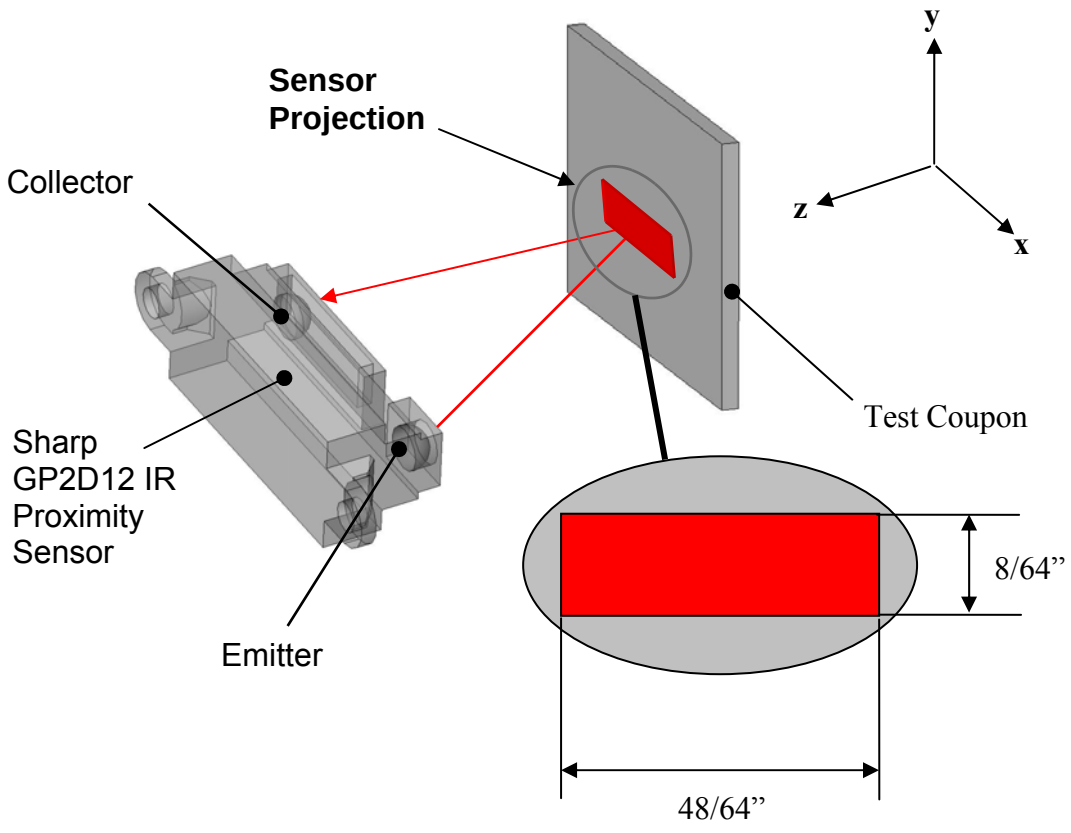

Figure 44: Projection of sensor onto test coupon at a linear track position of 0.9 inches. Detail shows dimensions of projected area on test coupon with respect to the x and y boundaries.

The variable horizontal position of the sample plate holder is a key parameter that allows the sample to be measured in the x direction while keeping the y and z coordinates fixed. This is achieved by a "T" slot machined in the plate holder base shown in Figure 45. The x direction of the plate holder can be varied within approximately seven inches from the center of the plate holder base in positive or negative x direction.

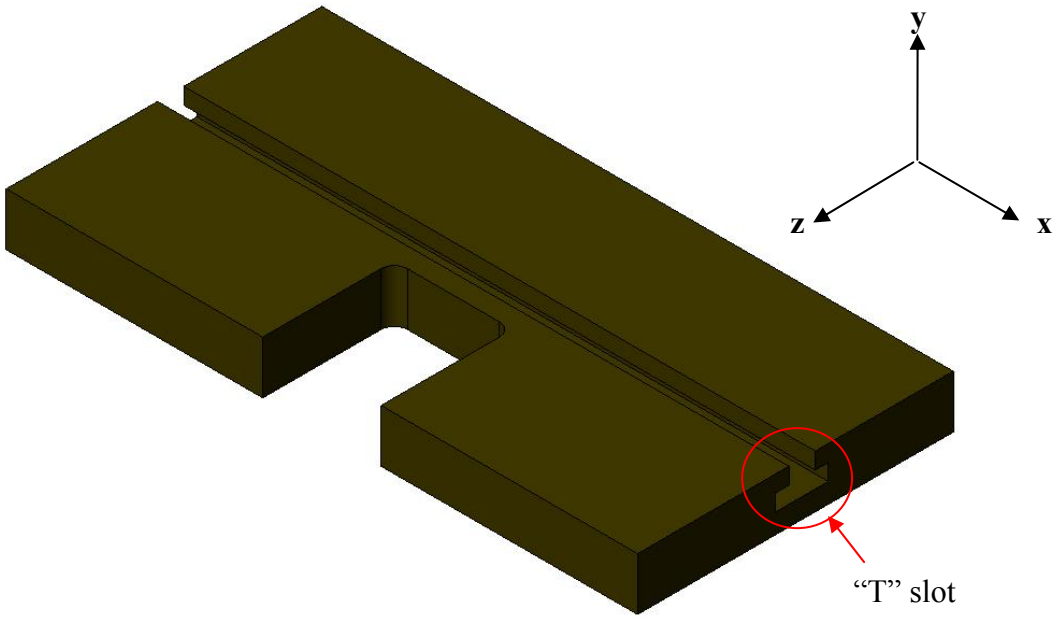

Figure 45: Plate holder base with "T" slot highlighted.

The vertical position of the sample is varied by placing the sample in any region of the five and a half by six inch plate holder area shown in Figure 46. This design feature helps to control the x and z directions of the sample.

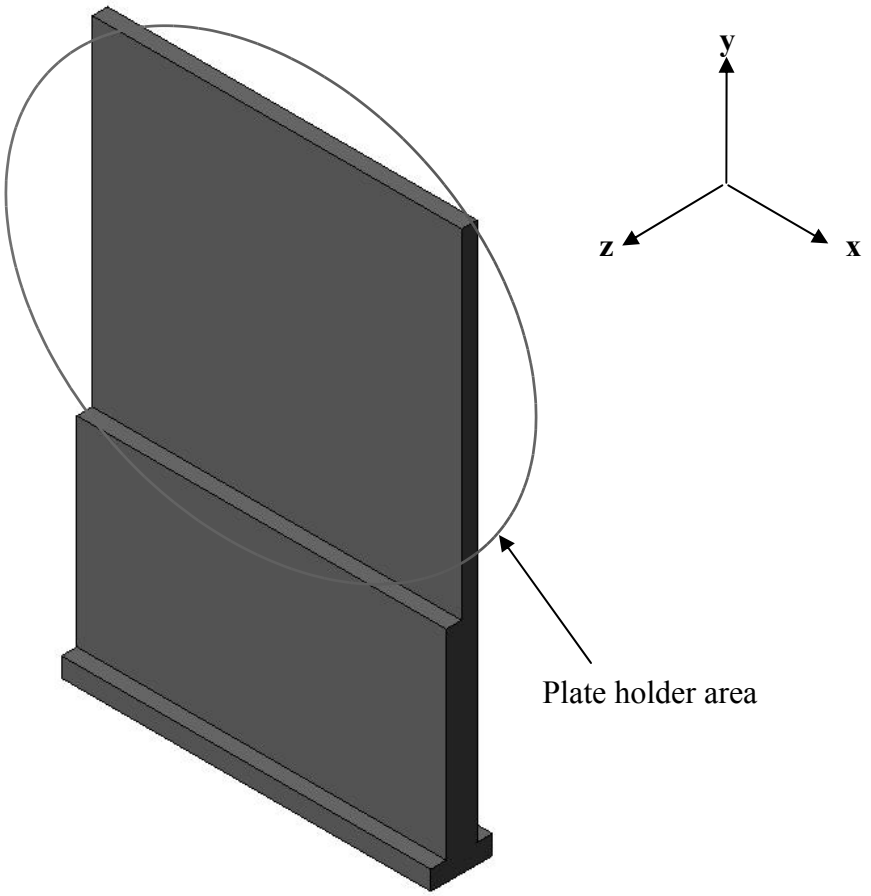

Figure 46: Plate holder with plate holding area identified.

The angle of the IR proximity sensor relative to the plate holder is controlled by a machine screw anchoring the base of the IR proximity sensor holder into the base of the linear positioning device. One of the two machine anchoring screws is removed and the IR proximity sensor holder is allowed to pivot about the other machine anchor screw as shown in Figure 47. The angle α is measured through geometric relations.

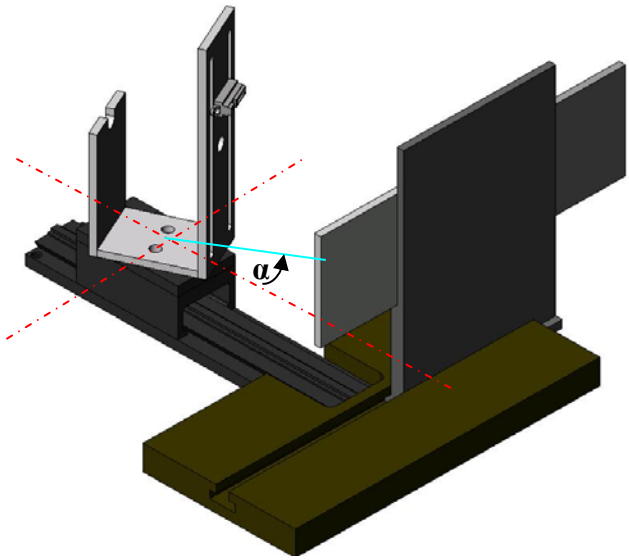

Figure 47: Variable angle function of test frame.

The final parameter that is variable while holding the other parameters constant is the orthogonal position of the IR proximity sensor from the plate holder or sample. The linear positioning varies the distance from the sensor to the sample by adjusting the positioning wheel on the side of the linear positioning track mount. The distance between the sensor and the plate holder can be controlled to within ± 1/100 using the linear positioning track.

A laser sighting hole is designed in the IR proximity sensor frame to give position on the sample relative to the IR proximity sensor center in the x direction. Vertical z direction is determined by measuring the height of the sensor and knowing the height of the spot on the sample relative to the sensor height as shown in Figure 38.

Preliminary tests include gathering data for both coated and uncoated samples during the first test run of the IR proximity sensors. To achieve this, both samples are mounted side by side on the plate holder using small C-clamps as shown in Figure 48.

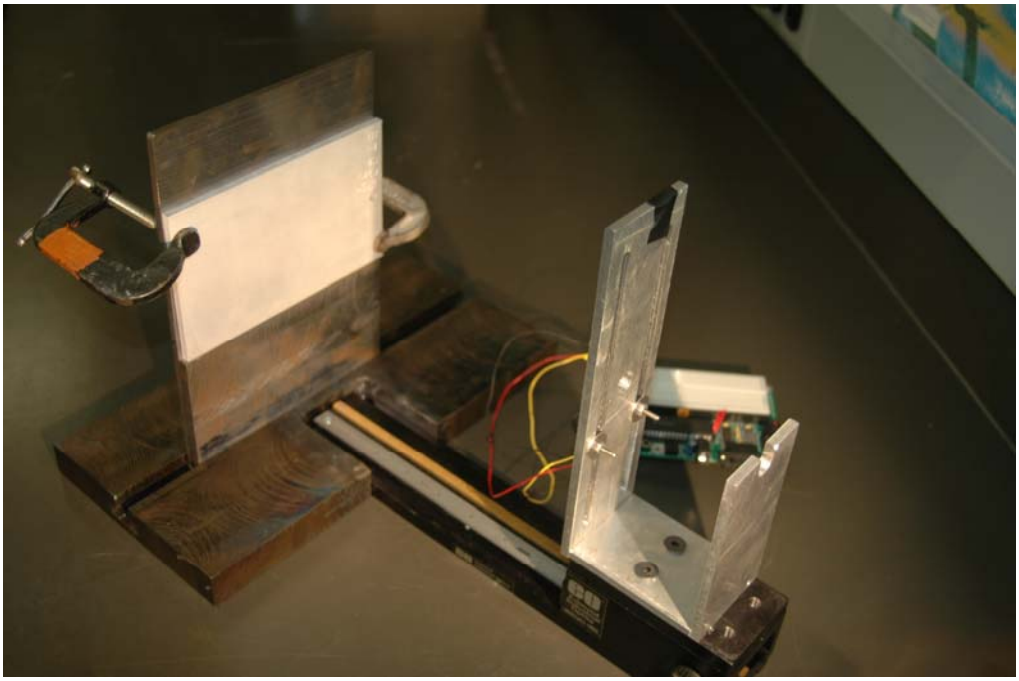

Figure 48: C clamps holding sample into plate holder piece in test frame assembly.

The samples are then pushed along the plate holder base "T" slot in the x direction. The IR sensor displays data from both the coated and uncoated plate depending on the plate which is placed in the IR sensors recording path.

Experimental Error

There are a few experimental variables in the test frame that could alter the results and cause error. The first source discussed in the previous section is the flatness of the plate holder holding area. The height of each corner is measured in the quality check test setup shown in Figure 41. The heights of the corresponding corners are listed in Figure 42. The plate height changes at most four thousandths of an inch, therefore has a slope of at most four thousandths of an inch over approximately 5.75 inches.

The second source of error is due to the combination of an interface mismatch at the "T" slot in the plate holder base and the base of the plate holder. These two areas were pieces that are designed as "made to fit." The plate holder base shown in the figure below is ground down using a grinding wheel until it slides through the slot. The grinding operation may have removed more material than necessary causing the plate holder base to lack the face to face contacts with the "T" slot walls necessary to hold the plate completely in place through the entire travel distance in the x direction. However, the error is more likely caused by a machining operation performed to cut the slot for the linear track positioning device after the "T" slot is machined. The slot for the linear track positioning device is cut using an acetylene torch which may have residual stresses in the slot causing an over machining operation to be necessary in the plate holder base. This causes a 0.050 inch error in the orthogonal distance from the sensor at any linear distance to the plate holder holding area when sliding the plate holder along the x direction. This 0.050 inch error occurs over a range of approximately four inches of travel along the x direction with respect to the center of the IR proximity sensor plate holder. This experimental error may affect the results.

Fourier Transform Infrared Spectroscopy

Experimental Setup and Procedure

A JY Horriba LabRAM Fourier Transform Infrared (FTIR) Spectroscopy setup is used to gather the data in four samples. For infrared adsorption to occur, two criteria must be met: 1) the frequency of the light must be equal to the frequency of vibration of the molecule and 2)a vibration must produce a change in the dipole moment.

For the purposes of this experiment, a multiwavelength light is used with an Attenuated Total Reflectance (ATR) objective. The FTIR spectrometer operates on the principle of detecting the absorption of evanescent light over a range of frequencies. Since a molecule can have a natural frequency that can be modeled by Hooke's law for simple cases and light contains an electric filed component; light can excite a molecule if the electric field component is the same wavelength as the natural frequency of the molecule. If absorption occurs at a particular wavelength of light then the absence of that particular wavelength of light at the detector indicates adsorption for that specific wavelength.[20]

The same samples analyzed in each of the coating evaluation experiments, lightly coated, partially coated and heavily coated are used in this experiment. The samples are placed on the FTIR LabRam stage and an ATR objective is used. Background data is collected and sample data is collected thereafter.

Experimental Errors

One source of experimental error in this experiment is the light focus on the sample. If the light source is not placed into intimate contact with the sample, then noisy data or no data can result. Background light can also be introduced into the data output resulting in hard to interpret data. In the case of this experiment, the data is actively checked using real time display before each measurement is recorded so no error due to improper laser focus is expected.

Raman Spectroscopy

Experimental Setup and Procedure

The Raman Spectrometer in this experiment is built onto a JY Horriba LabRam FTIR frame. The excitation laser in this experiment is 783.5 nanometers and is used in conjunction with a 100X lens magnification with a numerical aperture of 0.90. The Raman Spectrometer emits an excitation laser onto a sample. The sample then has the possibility of responding to this excitation laser through vibrational characteristics of the molecules being excited. The excitation laser excites the bonds in the molecules of the sample and inelestically scatters photons at a shifted frequency from the original excitation frequency. This shifted frequency is a virtual state of the photon emitted and is detected by a solid state device like gallium arsenide. The major function of Raman spectroscopy is for molecular identification. However, this experiment is being conducted determine if a signature of the coating exists due to particular bonding in the molecules of the coating and to determine if this signature changes between samples evaluated. There are four samples to be evaluated for this experiment. One sample is meant to provide baseline data for the following samples to be tested. Specifically, the baseline sample contains a well coated sample. This sample is expected to provide results that are characteristic of the coating. The next three samples are the same samples used for each of the coating evaluation experiments, heavily coated, partially coated and lightly coated samples. The sample is cleaned with a compressed air source or lint free cloth to avoid contamination. The instrument is calibrated using a silicon sample with a peak of 521 nanometers. The sample is placed under the 100X lens where the region of interest is focused the optical portion of the microscope frame. The laser is then focused

onto the sample surface. The parameters set in the software are the following for each measurement:

- Spectrometer: 750
- Acquisition Number: 5
- Exposure: 1
- Grating: 1800
- Objective: 100X
- Pin Hole: 250
- Neutral Density Filter: none
- Excitation Frequency: 783.5

The measurements are taken and data is output on the computer monitor. The files are saved and processed.

Experimental Error

Error due to the experimental test setup or experimental procedure is checked thoroughly for this experiment. Possible sources of error include: mismatching the software wavelength and the hardware configuration and not focusing the laser on the sample.

In the case of a mismatch between the software wavelength and hardware configuration, it is not know what the result would be. In this experiment the correct hardware configuration is verified before each experimental session and the software setting for wavelength to be used is set before each measurement. Therefore, no variations or errors in results are expected due to this possible source of error.

The second possible source of error is the laser focus. If the laser is not focused on the sample, the spectrum collected could possibly show some sort of noise, peaks due to ambient or atmospheric light interference or no data. However, since the laser is focused before each measurement taken, this possible source of error most likely does not contribute to error in the results.

Polarized Light Microscopy

Experimental Setup and Procedure

Polarized Light Microscopy is the last method tested but is one of the most powerful and revealing tests. Visual differences in the coating appearance are quantified by this simple and traditional microscopy technique used in combination with image processing software. Polarized light microscopy combined with imageJ can quantify light that is scattered in various directions due to the scratches observed on the ZE41A surface which changes the appearance of the coated surface. In this polarized light microscope setup, the light reflecting off of the samples becomes linearly polarized with the filter in plane between the sample and light source. When the sample or filter is rotated by 45^{o}, the light has maximum intensity due to the contribution of both the electric field and visible light source. This resultant vector produces the most intense light back to the receiving detector or CCD in this case. A Zeiss Axiophot light microscope is used in conjunction with a Coolsnap DF digital camera. A 100X magnification, 0.075 NA objective is used. Linearly polarized light and a light intensity of seven on a scale of one to ten on the Zeiss Axiophot are used. All images contain a calibrated scale at the upper right hand corner.

The three samples used in these experiments are the lightly, partially and heavily coated samples used in each of the coverage experiments. These samples are placed onto the stage using a 2.5X lens, numerical aperture 0.075. A polarizer is placed into the light path and an image for each of the ten areas on each sample is recorded using the Coolsnap DF digital camera. There are two images for each area recorded, one is with a zero degree stage rotation and one is with a 45^{o} rotation of the stage as shown in Figure 49.

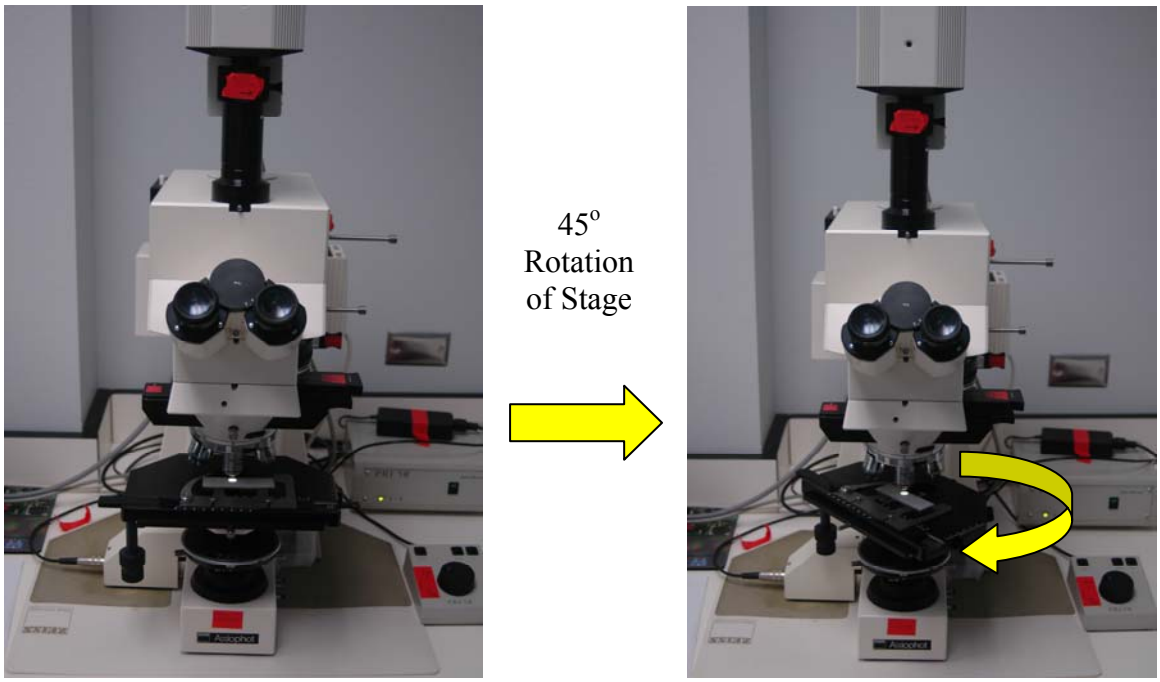

Figure 49: Zeiss Axiophot 45^{o} rotation of stage for polarized light microscopy image acquisition.

The two images produce notably different light intensities. It is important to note that each sample and angle of stage rotation is recorded with the same light source intensity. The difference between maximum and minimum extinction is 45^{o}. The TIF files recorded by the digital camera are then exported and processed using imageJ, available through the NIH. The ten images from each sample are imported into imageJ as a stack and a plugin[21] makes it possible to record information on an area in each image with the same region of interest area size for each sampling area. imageJ has the capability to measure specific parameters of the region of interest selected. Specifically, a mean grey count value for each image is analyzed for an area of ninety seven square pixels. The mean grey count measuring routine within imageJ allows 1024 grey values to be assigned to each pixel, as this is a ten bit image. The routine then adds the grey values of each pixel within the selected region of interest and calculates the mathematical mean of the grey count value in this selected region. The grey count value is then recorded for the zero and forty five degree rotations for each sample area. This process is repeated for each sample with the same light intensity.

Experimental Error

The experimental error in this experiment is kept to a minimum through careful experimentation practices and a proven design test setup. Some errors in the data that could result are due to the light intensity from the light source between each sample and the location of region of interest chosen for each sample area.

The first variable, light intensity is noted in every sample taken and is not changed throughout the duration of the experiment. If the light intensity did change during the experiment, the grey count values may differ between sample areas or samples. Therefore may not be able comparable from sample area to sample area or even sample to sample. However, since the light intensity did not change, there is no error attributed to this variable.

The second variable that could cause error in this experiment is the location of the region of interest chosen for each sample area. Each sample area appears to be uniform. If the sample area is not uniform then the region of interest location chosen within each sample area could affect the mean grey count value and make comparison between sample areas and samples difficult to correlate. However, since the sampling areas appear to be uniform, this variable does not seem to raise cause for error in the results.

DISCUSSION AND RESULTS

Thickness

Eddy Current Measurement

The results of the eddy current measurement test show that thicknesses are determined to be either zero or one micron based on the results displayed on the Defelsco Positest DFT LCD screen. A summary of the measurements recorded from each sample is listed in Table 6 -9.

Table 6: Eddy current measurements using the Defelsko Positest DFT for the sample shown in Figure 10.

Test Point	Thickness (µm)
A	0
B	-2
C	0
D	0
E	1
F	0
G	1
H	1
I	0
J	0
K	2
L	2

Table 7: Eddy current measurements recorded using the Defelsko Positest DFT for heavily coated ZE41A sample.

Test Areas	Thickness (µm)
1	0
4 – 8	0
10	0

Table 8: Eddy current measurements recorded using the Defelsko Positest DFT for partially coated ZE41A sample.

Test Areas	Thickness (µm)
7	0
1	-1
3	0

Table 9: Eddy current measurements recorded using the Defelsko Positest DFT for lightly coated ZE41A sample.

Test Areas	Thickness (µm)
3	0
7	0
5	0

Since the results of the eddy current measurement experiment provide data that is between zero and one and the error range of the Defelsko Positest DFT is ±0.1 mils + 3% error or ± 2 microns + 3% error, a thickness measurement cannot be determined.

Optical Light Microscopy

The results from the optical microscopy experiment are shown in Figure 23, Figure 24, Figure 25 and Figure 26**.** These images show that the conversion coating cannot be distinguished from the ZE41A substrate. The expected coating thickness of 0.4 to 1 micron is not resolvable with the resolution limit of a 100X, 0.95 numerical aperture dry lens objective due to possible aliasing.

Scanning Electron Microscopy

The scanning electron microscope experiment yielded the results shown in Figure 50 and Figure 51. These images do not clearly show the coating as the coating cannot be distinguished through color or structure from the magnesium alloy. This is the most significant factor that makes it difficult to find the thickness in these cross-sectional views.

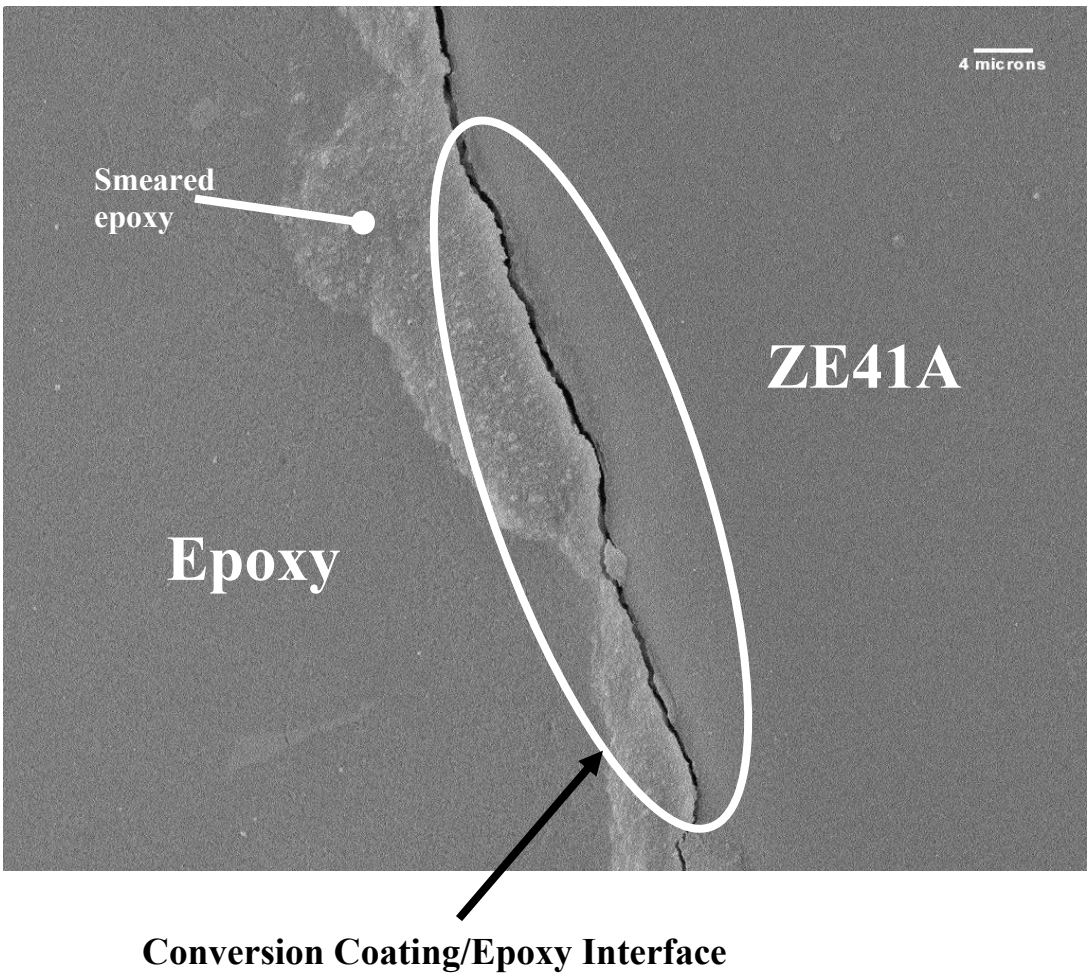

Figure 50: Cross-sectional view of ZE41A, environmentally friendly conversion coating and epoxy mounting structure. Image acquired at 1.5 Kv and 300X magnification.

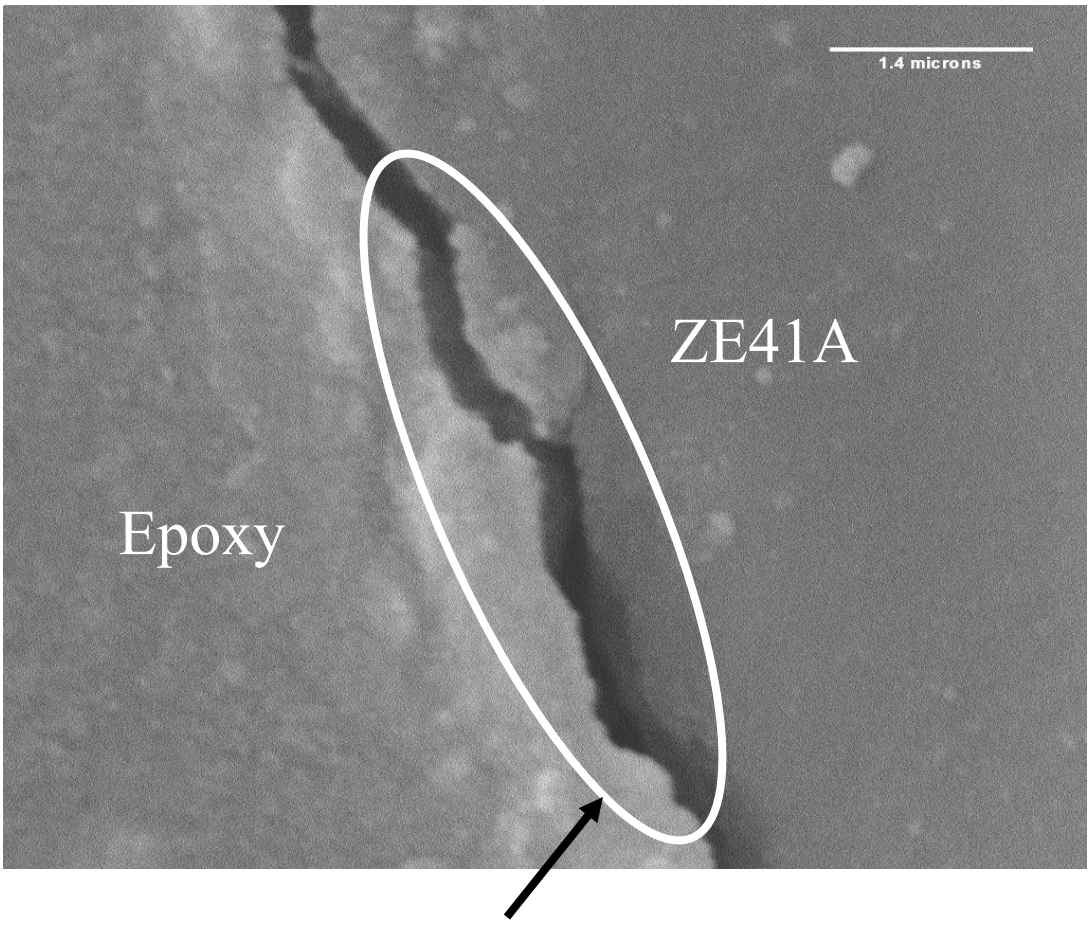

Figure 51: Cross-sectional view of ZE41A, environmentally friendly conversion coating and epoxy mounting structure at 15kV and 300X magnification.

Transmission Electron Microscopy

The results from the TEM experiment performed showed that the environmentally friendly conversion coating is approximately 0.5 to 0.8 microns in thickness as shown in Figure 52.

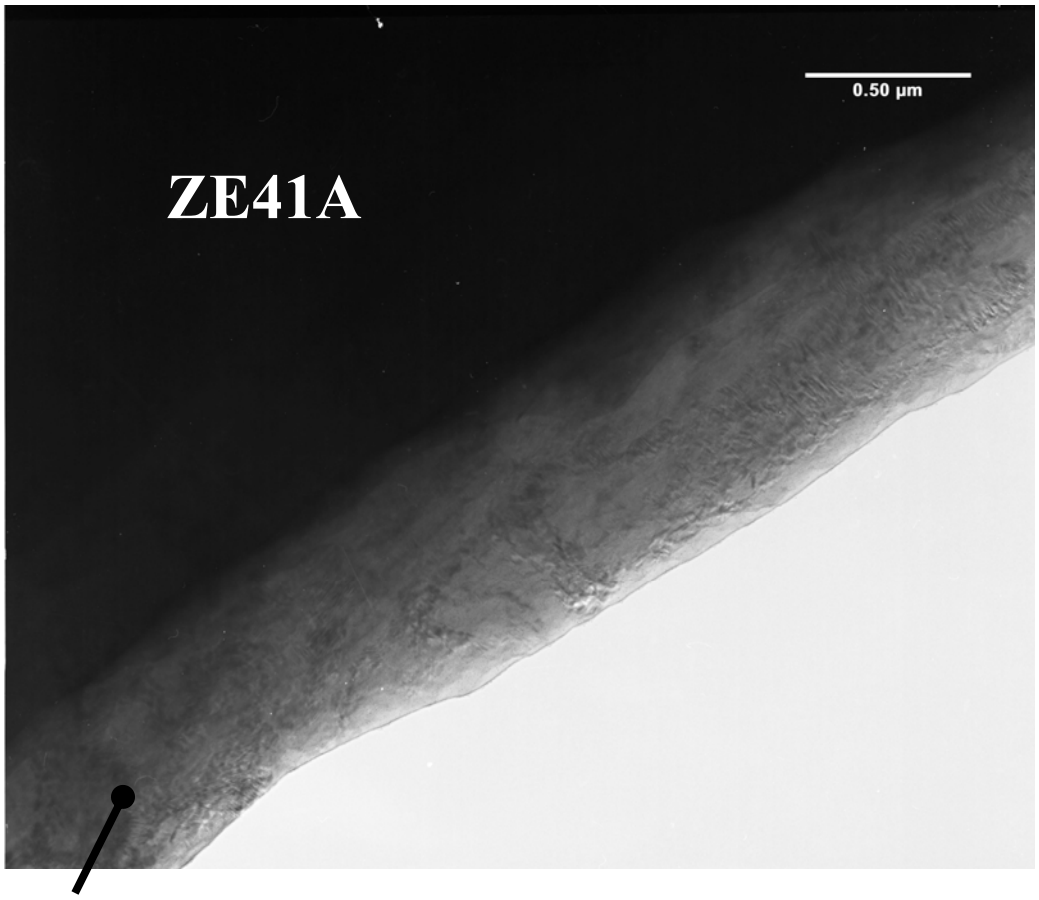

Figure 52: TEM image of ZE41A and coating cross-sectional view at 30K X magnification.

The environmentally friendly coating is clearly seen and distinguished from the ZE41A substrate in Figure 52. The ZE41A is clearly not electron transparent while the environmentally friendly coating is. EDS data could not be acquired for this particular sample for chemical identification as the detector malfunctioned during data acquisition so definitive coating identification cannot be made.

Confocal Microscopy

The three dimensional stack of the images acquired using the Olympus FV1000 are shown in Figure 53. Since three micron steps were the maximum resolution available through the microscope setup, aliasing in the image shown in Figure 53 did occur since the step is expected to be approximately 0.5 to 0.8 microns in thickness according to the results provided in the TEM Results and Discussion section.

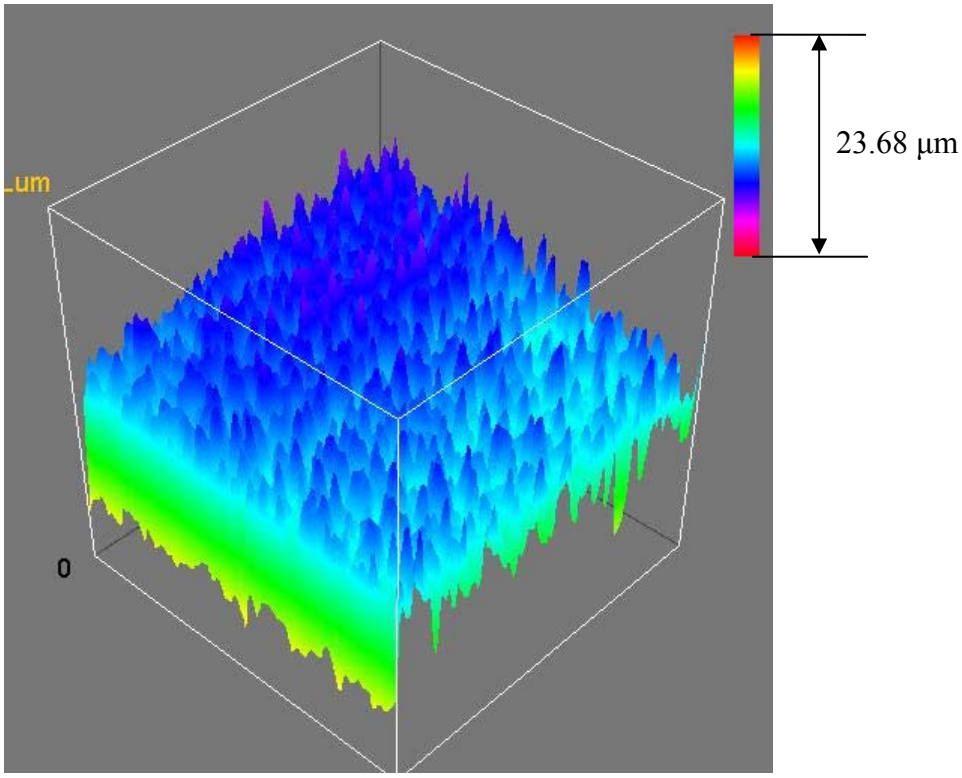

Figure 53: Confocal microscope three dimensional z-stack image of the gradual step between a coated and uncoated ZE41A sample shown in Figure 16.

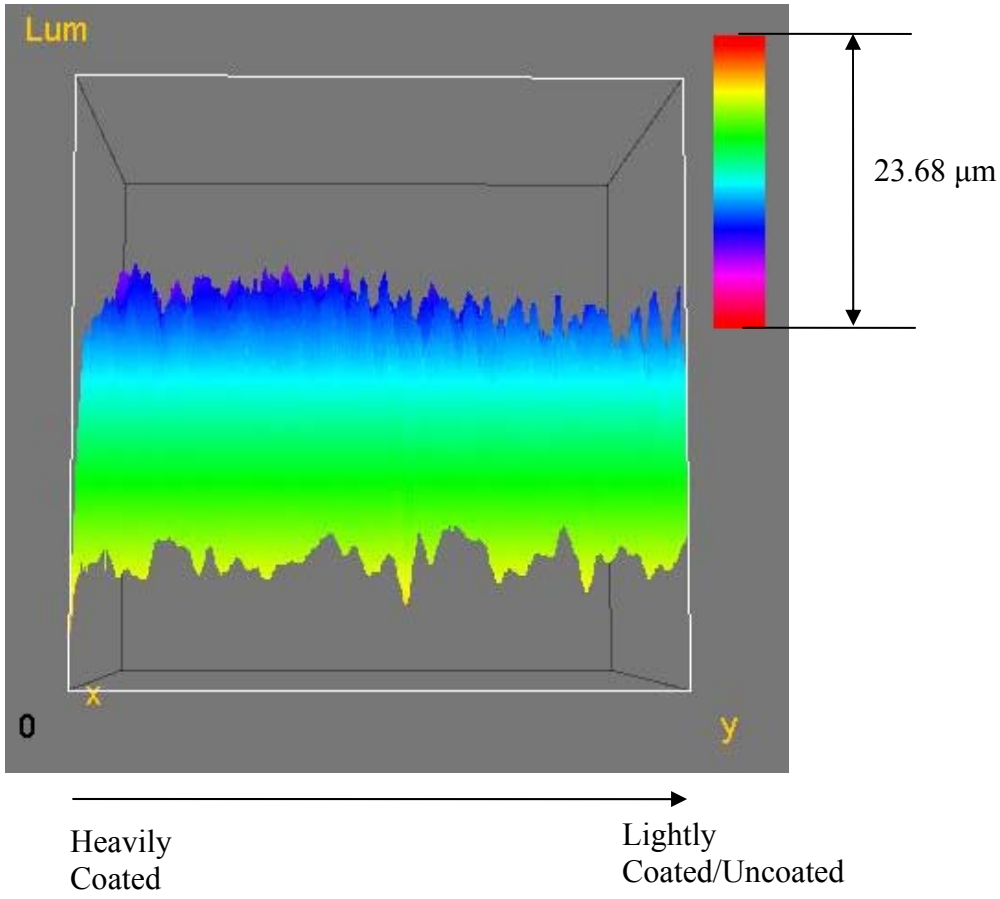

Figure 54: 3-D reconstruction of front view from slices taken with the Olympus FV1000 confocal microscope of the sample shown in Figure 16. The gradual step of the abraded result is shown on the horizontal scale at the bottom of the image. The scale bar shown on the upper right hand corner is a calibrated scale bar created using the imageJ depth coded stack function.

Coverage

Infrared Proximity Sensor

Results

The results from experiments with the Sharp GP2D12 IR proximity sensor show that a difference between a coated and uncoated ZE41A surface is shown in the digital output. These results from the test described in the Test Methods and Procedures section are shown in Figure 55 -Figure 62. The data used to develop each trend is an average of three data points collected at each linear track position and are shown in Figure 55 - Figure 62. The error is represented as the standard deviation for a series of three data points per linear track position from the three data points at each linear track position. The error bars show that if an overlap between the error bars occurs, then no distinction between the trends of overlapped data should be made. However, if no overlap in the data occurs, then a distinction between the trends in the plot can be made.

The first series of data shows the digital output of the Sharp GP2D12 IR proximity sensor as a function of distance measured on the linear positioning track for each of the coating conditions, lightly, partially and fully coated.

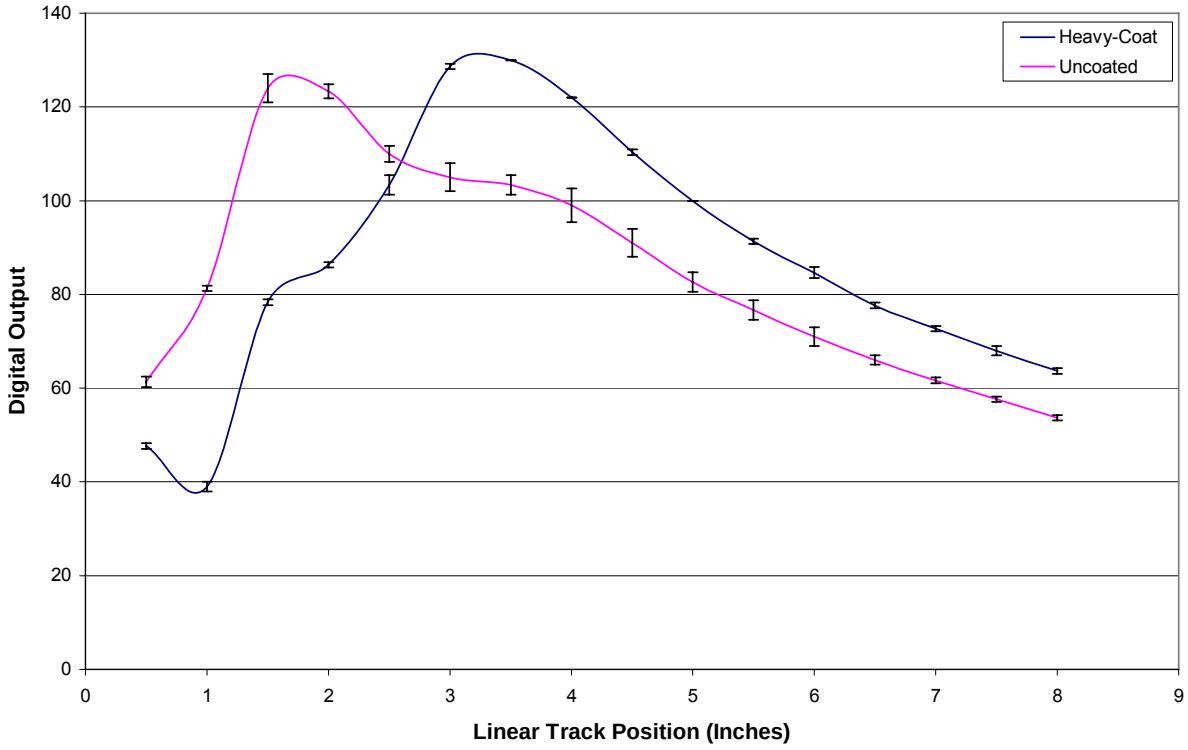

Figure 55: Sharp GP2D12 IR proximity sensor digital output as a function of linear track position for a heavily coated ZE41A magnesium alloy compared to an uncoated ZE41A magnesium alloy. Error bars shown represent greatest standard deviation from entire data series for each data set for a worst case scenario representation.

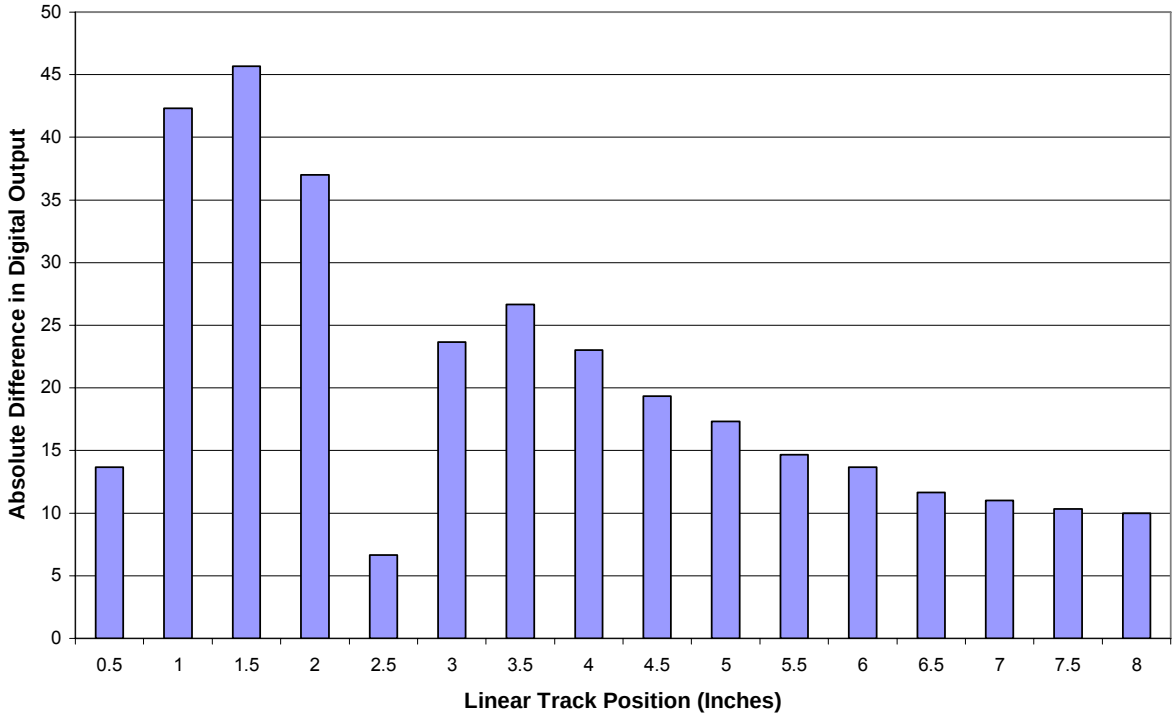

Figure 56: Difference in the Sharp GP2D12 IR proximity sensor digital output between a heavily coated ZE41A surface and an uncoated ZE41A surface.

Figure 55 shows that the IR proximity sensor digital output is distinctly different between the two coating conditions, heavily coated and uncoated. The digital output for each coating condition varies with linear track position. Upon initial observation, the digital output increases as the sensor distance increases from each coating condition. However, the data reaches approximately 1.5 inches and begins to converge. The data for each condition converges at a linear track position of approximately 2.75 inches. After the data converges, the digital output seems to reverse its logic and decrease as the IR proximity sensor is moved away from the target. It should be noted that a distinct difference in the coating is maintained after the data sets for the heavily coated and uncoated conditions converge. The data presented in Figure 55 also shows that the error

associated with each data point for each condition does not overlap with the other one another except for when both trends converge at one point. Figure 56 shows the differences of the digital output recorded from the Sharp GP2D12 IR proximity sensor between the heavily coated and uncoated ZE41A. It should be noted that the largest difference between the two trends occurs between one and two inches as measured by the linear positioning track.

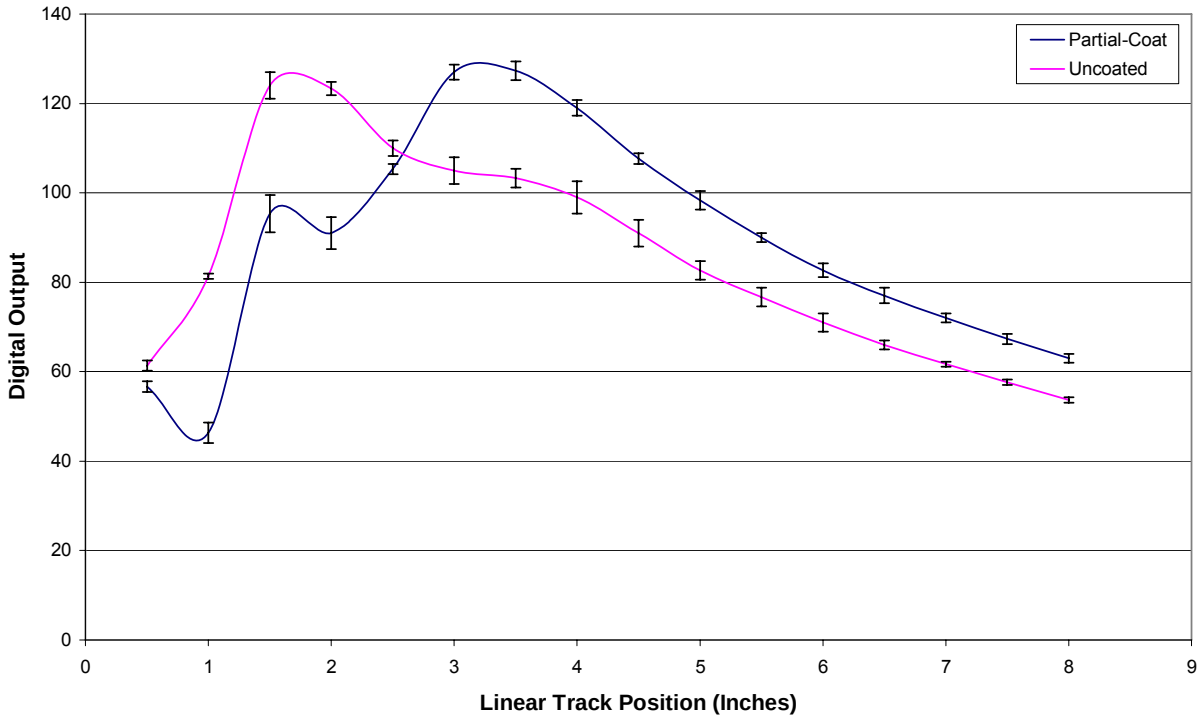

Figure 57: Sharp GP2D12 IR proximity sensor digital output as a function of linear track position for a partially coated ZE41A magnesium alloy compared to an uncoated ZE41A magnesium alloy. Error bars shown represent greatest standard deviation from entire data series for each data set for a worst case scenario representation.

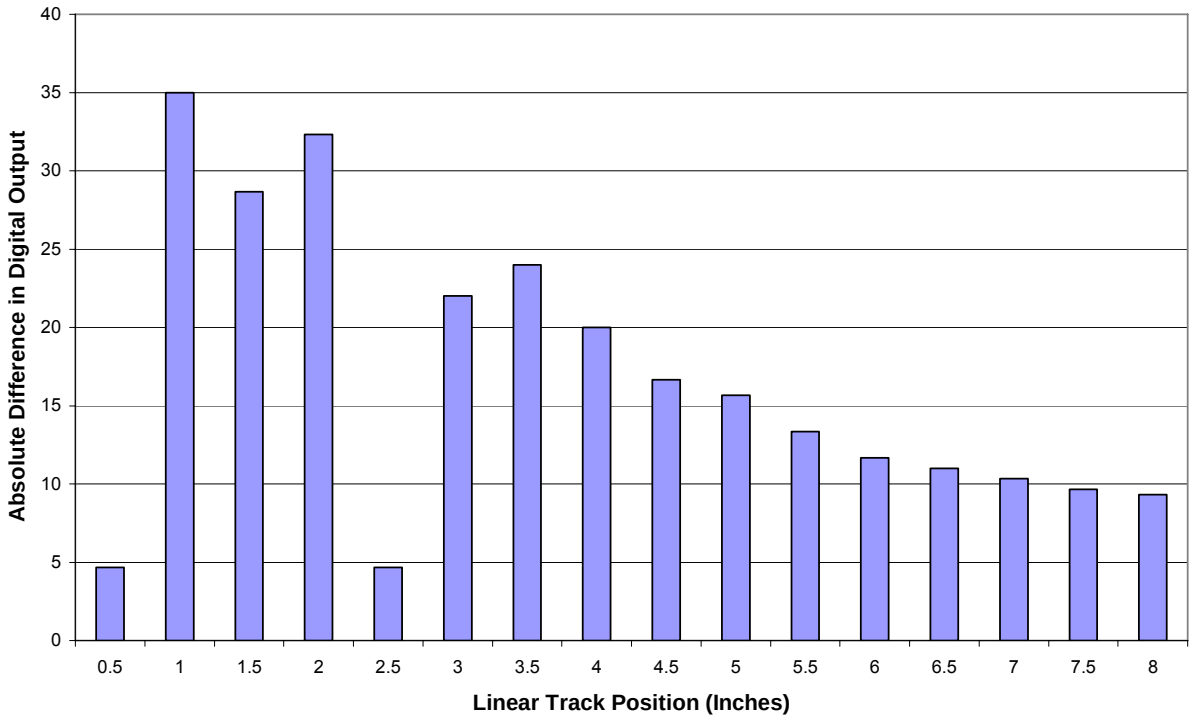

Figure 58: Difference in the Sharp GP2D12 IR proximity sensor digital output between a partially coated ZE41A surface and an uncoated ZE41A surface.

Figure 58 shows the digital output of the IR proximity sensor as a function of linear track position for a partially coated ZE41A test sample compared to the uncoated ZE41A test sample. The data in this plot shows the same general trend displayed in Figure 55. The measured signal from the partially coated surface and uncoated surface differ distinctly and then sharply converge at a linear track position of approximately 2.75 inches. The data error only overlaps at the point of convergence. The difference between the digital output observed for the partially coated surface and the digital output of the uncoated surface are shown in Figure 58.

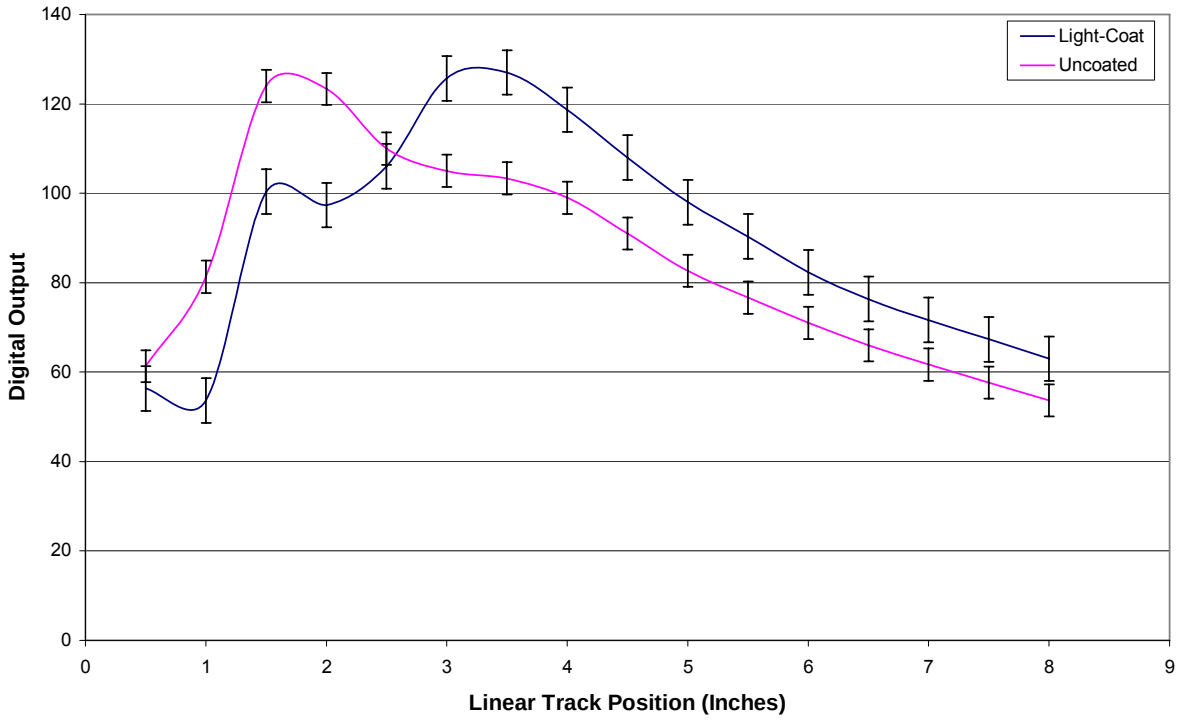

Figure 59: Sharp GP2D12 IR proximity sensor digital output as a function of linear track position for a lightly coated ZE41A magnesium alloy compared to an uncoated ZE41A magnesium alloy. Error bars shown represent greatest standard deviation from entire data series for each data set for a worst case scenario representation.

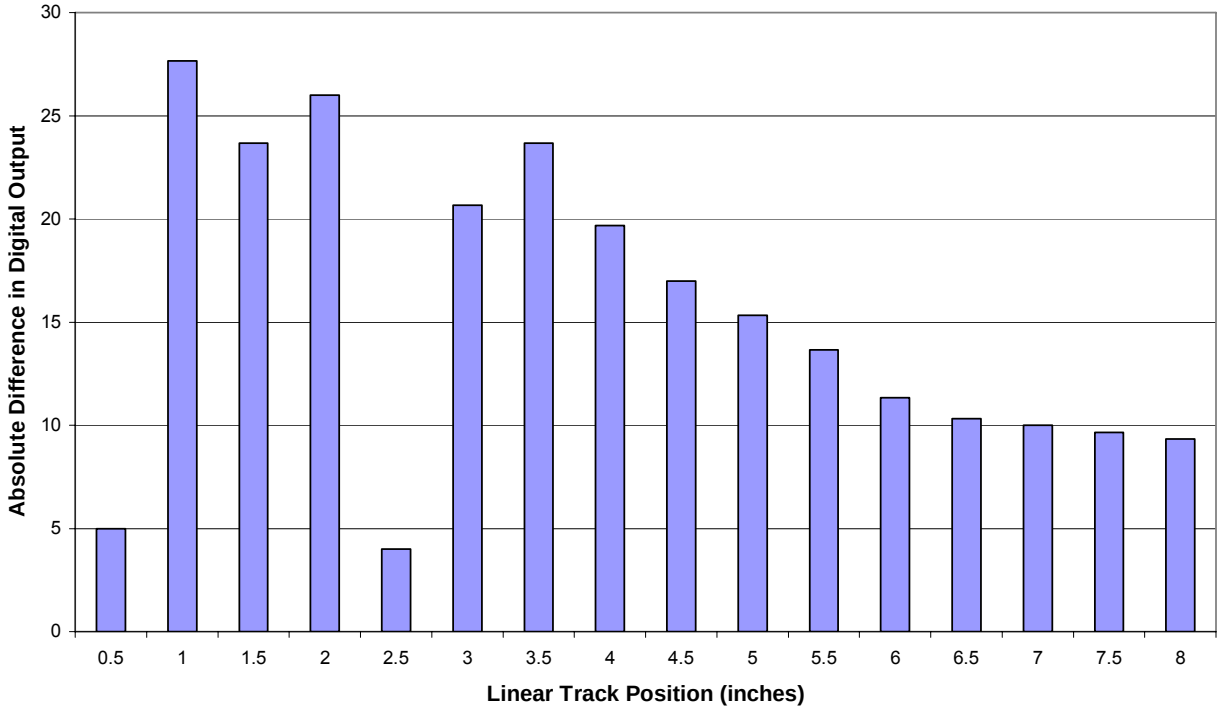

Figure 60: Difference in the Sharp GP2D12 IR proximity sensor digital output between a partially coated ZE41A surface and an uncoated ZE41A surface.

Figure 59 shows the digital output of the Sharp GP2D12 IR proximity sensor for both the partially coated and uncoated ZE41A surfaces as a function of linear track position. The same trend plotted in Figure 55 and Figure 57 is observed in Figure 59; the distinct difference in digital output between a coated and uncoated ZE41A surface. The same logic switch where the data converges and separates is also observed at a linear track position of approximately 2.75 inches. Figure 60 shows the observed difference in digital output between the partially coated and uncoated condition. It should be noted that the differences are most clear between 0.5 and 2 inches and should be noted in Figure 56 and Figure 58 as well.

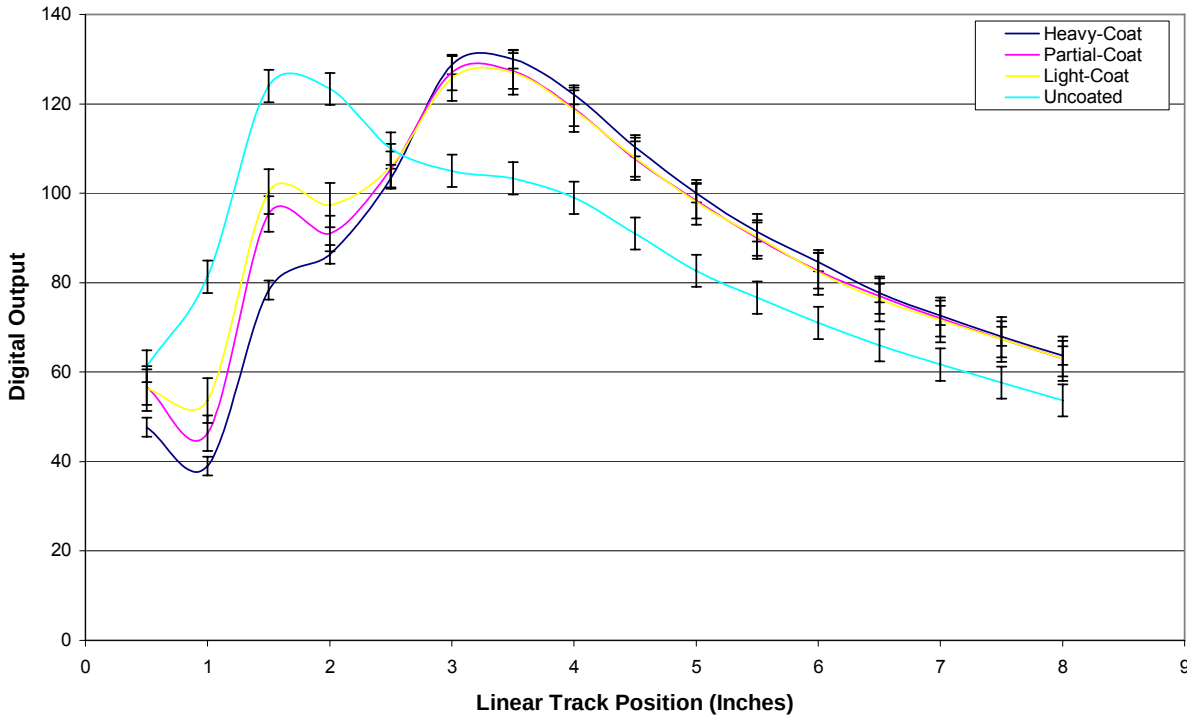

Figure 61: Sharp GP2D12 IR proximity sensor digital output as a function of linear track position comparing heavily, partially, lightly coated and uncoated ZE41A magnesium alloy ZE41A magnesium alloy. Error bars shown represent greatest standard deviation from entire data series for each data set for a worst case scenario representation.

Figure 61 summarizes the trends observed in Figure 55, Figure 57 and Figure 59. It should be noted that the trends between the different coating conditions, heavily, partially and lightly coated are very similar. There are distinct differences between these trends in that the differences between the coated and uncoated conditions vary depending on the coating condition being examined. Figure 62 shows this observation more clearly.

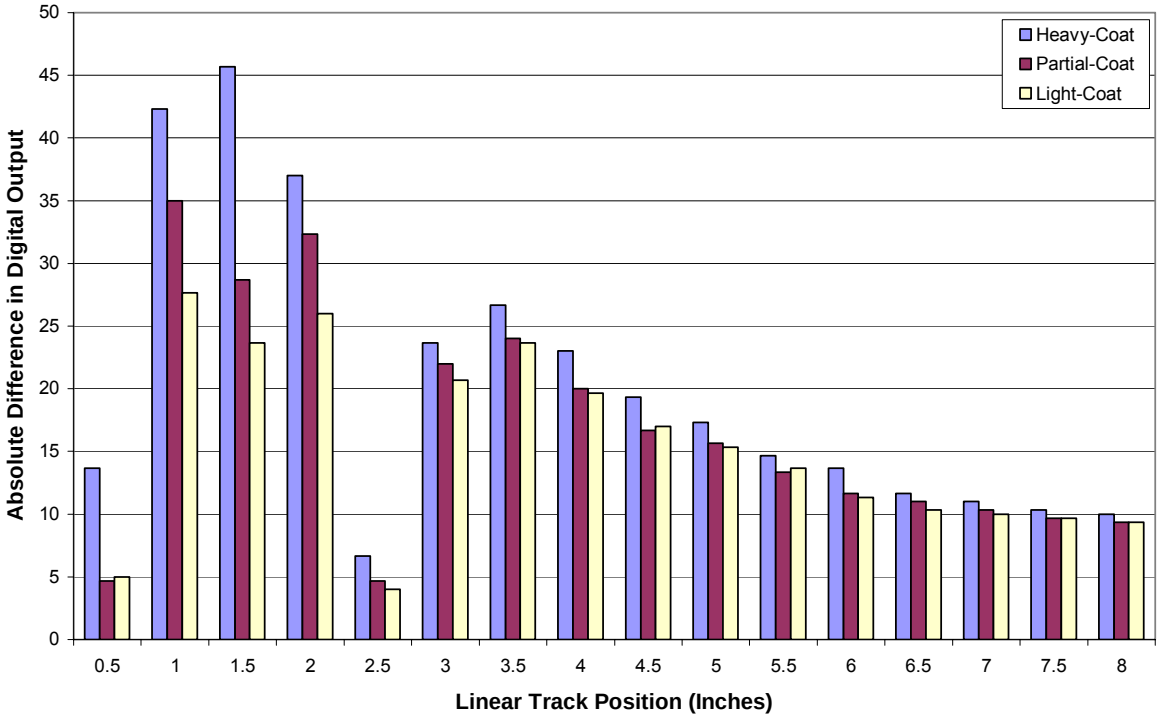

Figure 62: Comparison of differences in Sharp GP2D12 IR proximity sensor output between coated conditions of ZE41A and uncoated ZE41A.

Figure 62 shows that the differences in digital output between a heavily, partially, lightly coated comparison to the uncoated case.

In summary, the data from this experiment shows that a distinct difference between a coated and uncoated ZE41A surface can be determined. Lastly, the data presented in Figure 55, Figure 57 and Figure 59 showed that a change in logic seemed to occur at a linear track position of approximately 2.75 inches. The data indicated that digital output from the Sharp GP2D12 IR proximity sensor increased as the IR proximity sensor as the linear track position increases (the sensor is pulled away from the sample). However, at 2.75 inches the digital output indicates that as the linear track position is increased past approximately three inches, the digital output from the IR proximity sensor

decreases. The reason for this observation is known and provided with more detail in the following Discussion section.

Discussion

The discussion in this section is merely one possible explanation of the sensor operation. Since the coating and sensor both retain proprietary information, it is not possible to definitively explain the trend in the results provided. The explanation in this discussion is based on known physical parameters of the sensor, controlled variables in the test setup, laws of refraction and reflection and interpretation of the results with respect to these known parameters.

In general an infrared proximity sensor operates on the principle of triangulation. For this case, light is emitted from a diode emitter at a slight angle, γ as shown in Figure 63, toward an objective to be measured.

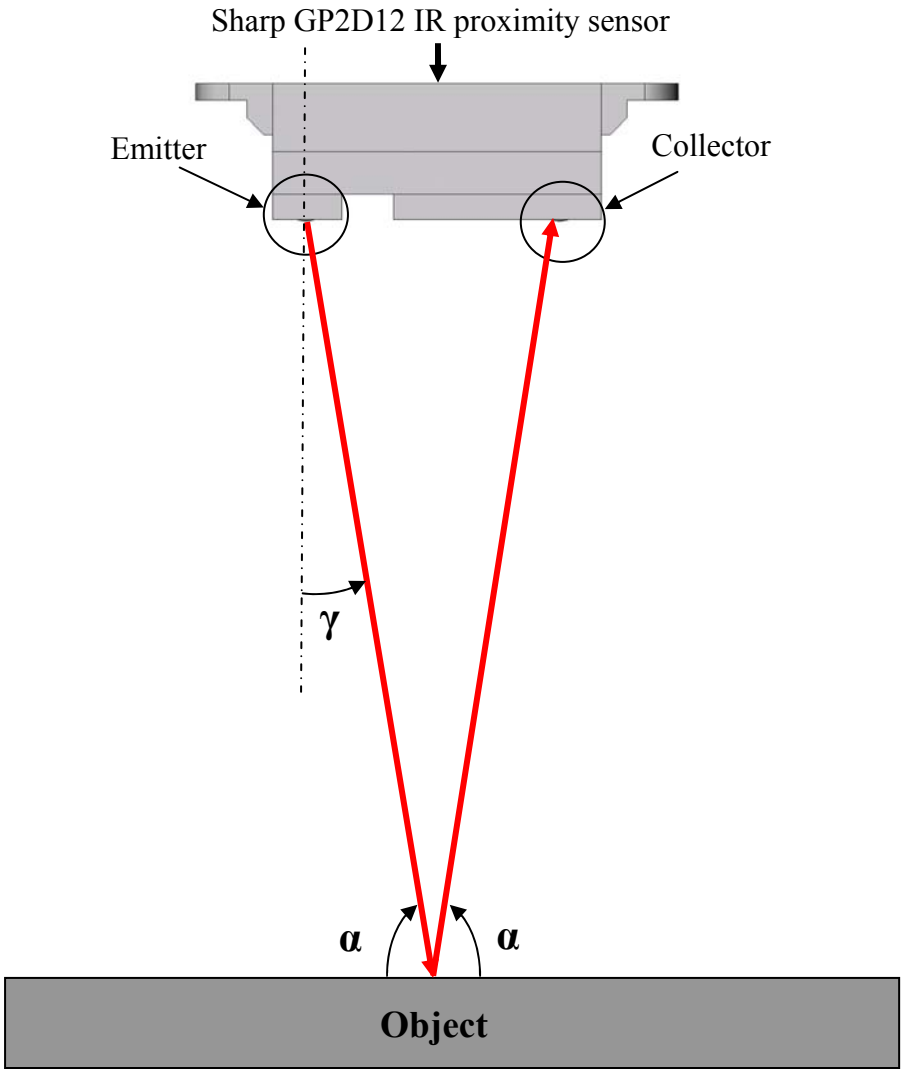

Figure 63: Emitting beam angle, γ from Sharp GP2D12 IR proximity sensor. γ is the emission angle and α is the incident angle relative to the object it interacts with.

The light is reflected from the object which it is projected onto and back to the sensing portion of the sensor assembly. In the case of the Sharp GP2D12 IR proximity sensor, light is reflected back to a PSD located on the sensor assembly as shown in Figure 63. The PSD operates on the principle of the lateral photoeffect and can be imagined as a series of resistors[22]. For illustration purposes Figure 64 details a series of the resistors

that model the behavior of the PSD portion of the Sharp GP2D12 IR proximity sensor shown in Figure 63.

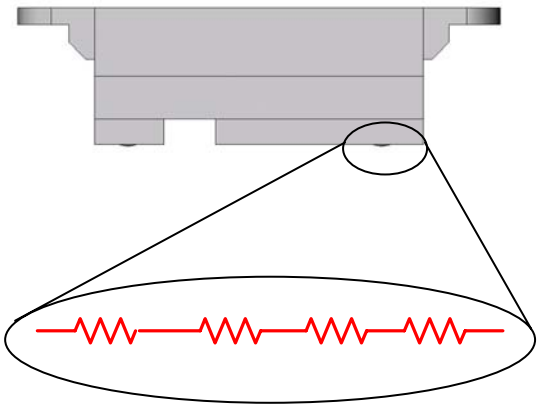

Figure 64: PSD modeled as a series of resistors.

A signal is carried through the series of resistors as light originating from the emitter and reflected off of the object comes into contact with this array at a point. The signal carried through the series of resistors changes as the location of the light along the series of resistors changes. The signal carried through the series of resistors is used as the output signal generated and delivered through the analog output conduit of the circuit. The signal carried through the circuit output conduit is directly related to the location where light interacts with the PSD. As the sensor is moved closer or further away from the object or vice versa, the point in the x direction at which the PSD receives the emitted light changes location as shown in the Figure 65

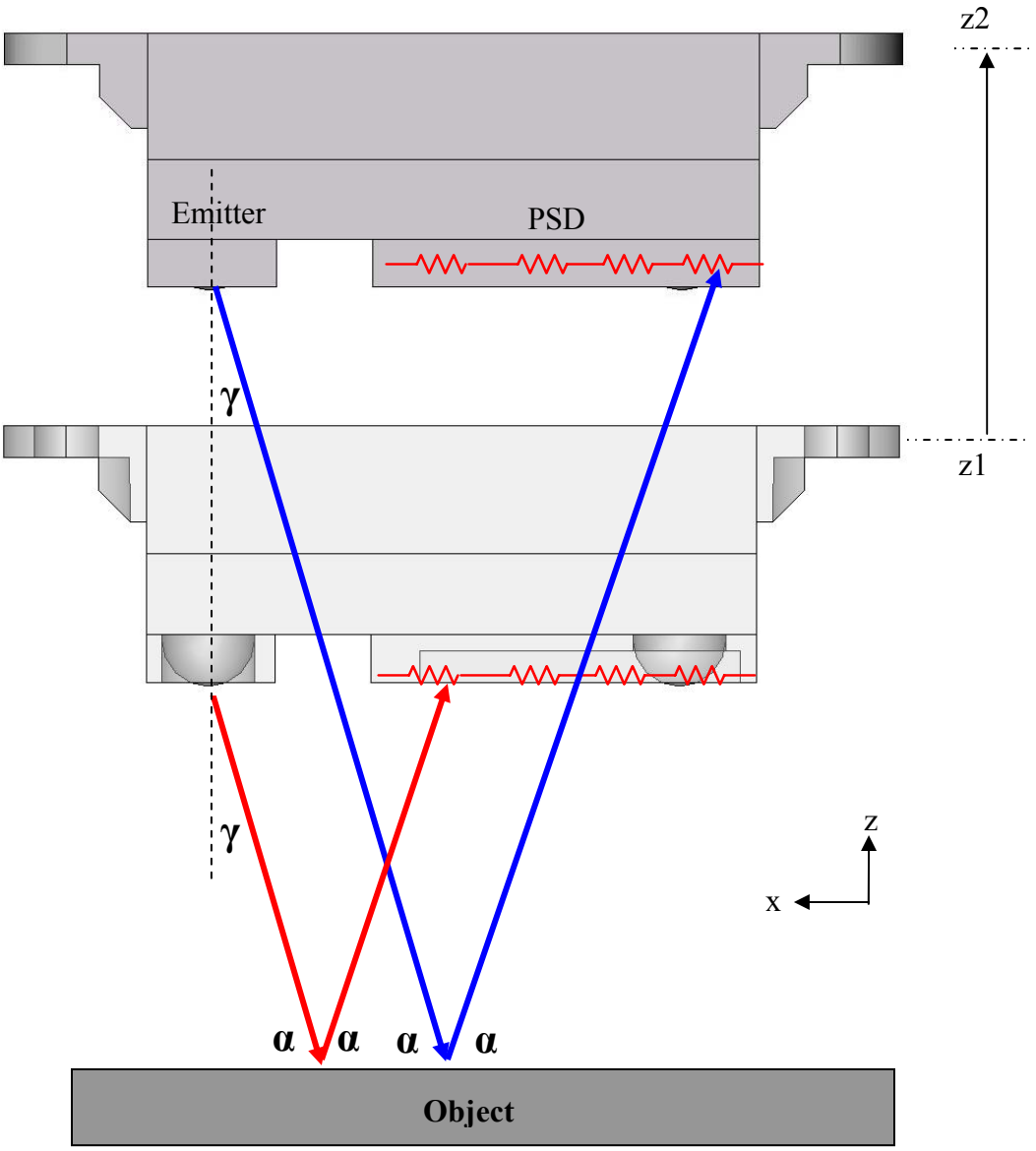

Figure 65: Illustration showing the emitted light from the emitting diode striking the PSD at two distinct positions in the x direction when moving the sensor from z1 to z2 (away from the object).

In this particular case, there is a distinct difference between the digital output measured by the IR proximity sensor for a coated and an uncoated ZE41A sample. This result indicates that the light received by the PSD is received at different locations on the

PSD. Based on the triangulation principle used in the Sharp GP2D12 infrared proximity sensor, initial logic would indicate that the sensor is measuring the distance between the coated surface and the sensor or the non coated surface and the sensor as shown in the Figure 66.

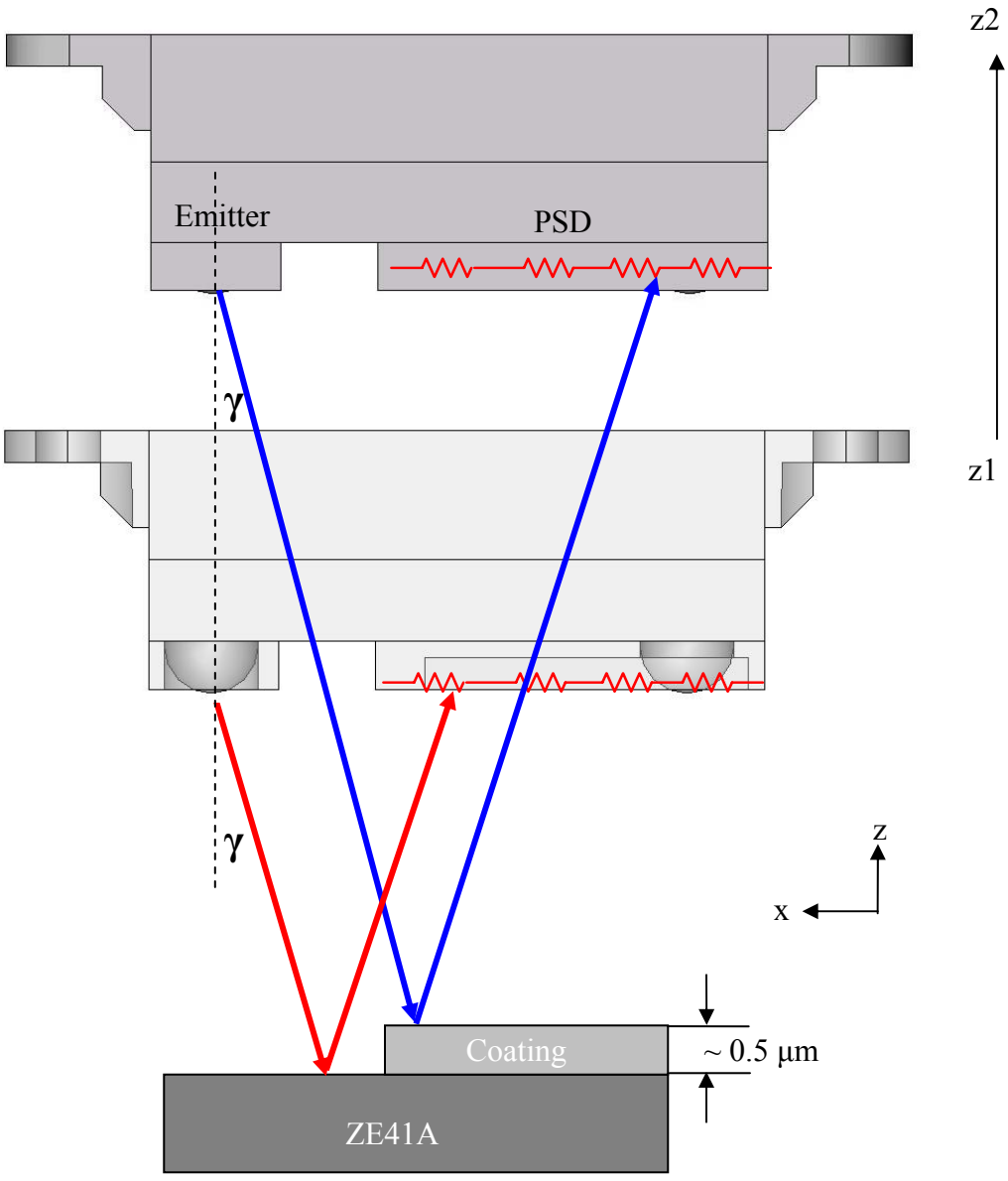

Figure 66: Figure showing traditional mentality in illustrating operation of Sharp GP2D12 IR proximity sensor in regards to the ZE41A coated samples.

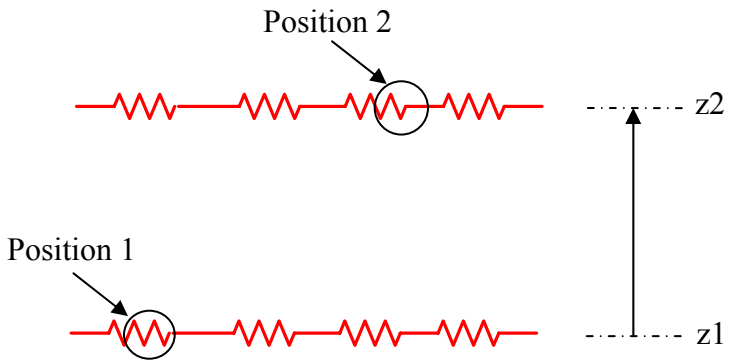

Figure 67: Detailed illustration of Figure 66 PSD showing two distinct positions where light strikes the PSD respective to z position.

Since the digital output from the Sharp GP2D12 IR proximity sensor is processed with a PIC16f877, certain limitations such as resolution apply. The PIC16f877 is equipped with a 10 bit analog to digital converter.[23] This means that there are 1024 bits that can be resolved from an analog signal. Since the Sharp GP2D12 IR proximity sensor is used to measure linear distances between 10 and 80 centimeters,[24] the smallest resolvable distance with a 10 bit analog to digital converter is 781.25 microns per bit. Sample calculation is shown below:

$$R = \frac{\Delta x}{b} = \frac{0.8\cancel{m}}{1024} * \frac{1*10^{6}\,\mu}{1\cancel{m}} = 781.25\mu$$

R = Resolution

b = Total number of resolvable bits

Δx = Functional range of sensor in meters

The data collected in the TEM experiment showed that the environmentally friendly conversion coating is approximately 0.4 to 0.6 microns in thickness. Since the Sharp GP2D12 IR proximity sensor used in conjunction with the PIC16f877 can only resolve

up to 781.25 microns per bit, it is impossible to claim that the Sharp GP2D12 IR proximity sensor used in conjunction with the PIC16f877 can resolve the coating thickness by calculating the difference in distance measurements between the IR proximity sensor and the coated sample and the IR proximity sensor and the uncoated sample. Since the data shows that a distinct difference exists when measuring the distance between the coated sample and the IR proximity sensor and measuring the difference between the uncoated sample and the IR proximity sensor and explanation must exist and is presented in the following paragraphs.

Coating transparency must be established for the following explanation of the following model. If the index of refraction for the coating is chosen to be that of SiO, ~1.6 a component known of the coating and the index of refraction of air is 1.00, the following relation can be used to calculate the reflectance of the coating.[25]

$$R = \left(\frac{n_2 - n_1}{n_2 + n_1} \right)^2 = \left(\frac{1.6 - 1.00}{1.6 + 1.00} \right)^2 = 0.05$$

$n_2 > n_1$

n_2 is the index of refraction of the coating

n_1 is the index of refraction of air

Since the reflectance of the coating is 0.05, this means that 95% of the light traveling to the coating is transmitted through the coating. This implies that the coating is fairly transparent.

In the IR proximity sensor experiment, light is reflected from the ZE41A in both the coated and uncoated conditions and sent to the PSD. Light is not reflected from the coating when the ZE41A is coated with the environmentally friendly conversion coating. This is true since the coating is transparent to the wavelength of light emitted by the

Sharp GP2D12 IR proximity sensor as shown in the FTIR data. However, light entering the coated surface is affected as general macroscopic observations with the unaided eye have shown.

Using the laws of refraction, particularly Snell's law, light striking the conversion coating surface can be said to refract at an angle that differs from the incident angle of the entering the coating. The following mathematical relationship shall be applied for this case:

$$n_a \sin\theta_a = n_b \sin\theta_b$$

n_a = refractive index of air = 1.00

n_b = refractive index of environmentally friendly coating = unknown

θ_a = incident angle = γ

θ_b = refracted angle = β

Using the laws of refraction and reflection, light striking the sample leaves the sample with the same refracted angle and incident angle and travels to the PSD where it strikes the series of resistors at a particular location as Figure 68. A signal is then output to the PIC16f877 from the IR proximity sensor quantifying the position where the light strikes the PSD.

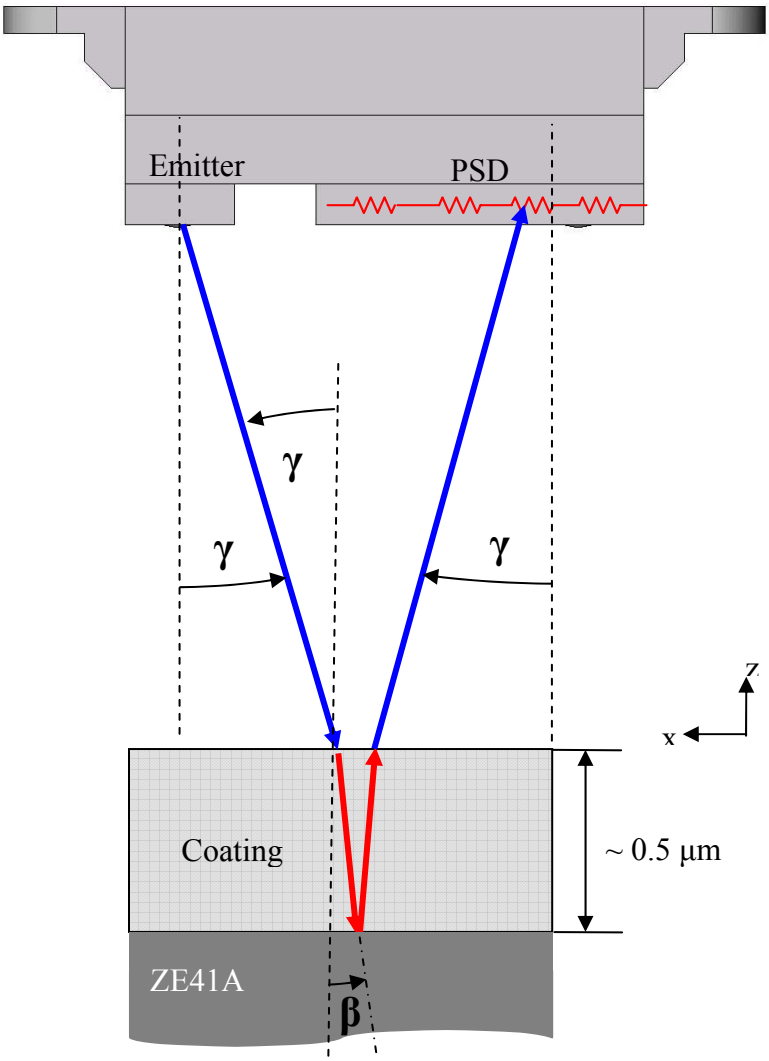

Figure 68: Illustration showing refraction occurring through the coating creating an angle β when the light with incident angle γ passes through the coating and strikes the ZE41A substrate. The blue rays indicate the non-refracted light and the red rays indicate the refracted light.

In the case of the uncoated ZE41A surface, light emitted from the diode in the Sharp GP2D12 IR proximity sensor is directed toward the sample at the same angle used in the case of the coated sample. Instead of refracting through the coating in this case, the light strikes the uncoated surface and leaves at the same incident angle that it arrived at. The comparison between the uncoated and coated cases is illustrated in Figure 69.

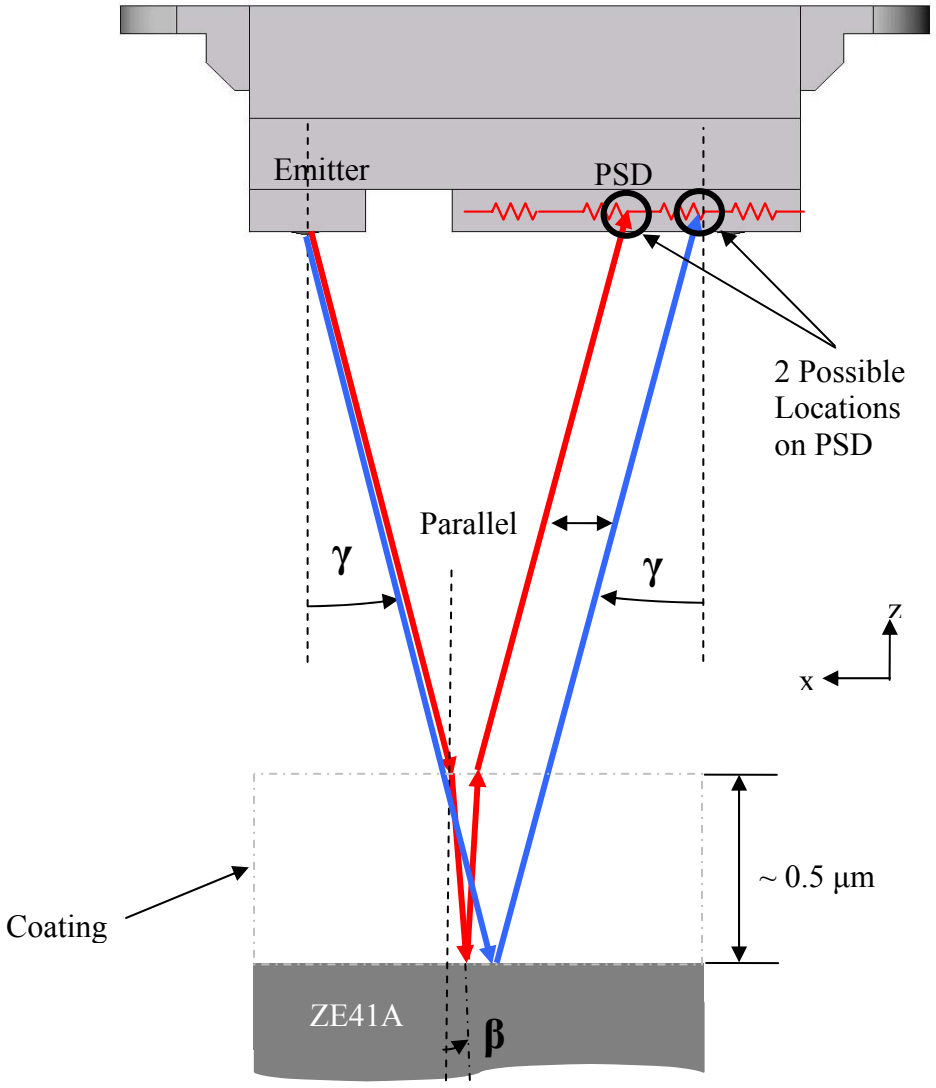

Figure 69: Illustration of the difference of light striking location on the PSD between an uncoated and coated case. The red ray indicates the light behavior for the coated case where the coating is represented by the gray dashed line. The blue ray indicates the light path in the uncoated case.

When comparing the two scenarios shown in Figure 69, the light reflected to the PSD in the coated case, shown with red ray strikes the PSD further to the left on the PSD when compared to the light reflected in the uncoated case represented by the blue rays. Since the incident angle is the same in both cases because they are controlled by the fixed angle of the emitter in the IR proximity sensor, the two rays yield parallel results. When

comparing this model to a portion of the data actual data, the model represents the general trend exhibited by this data. The data tested for correlation with the model is shown in Figure 70.

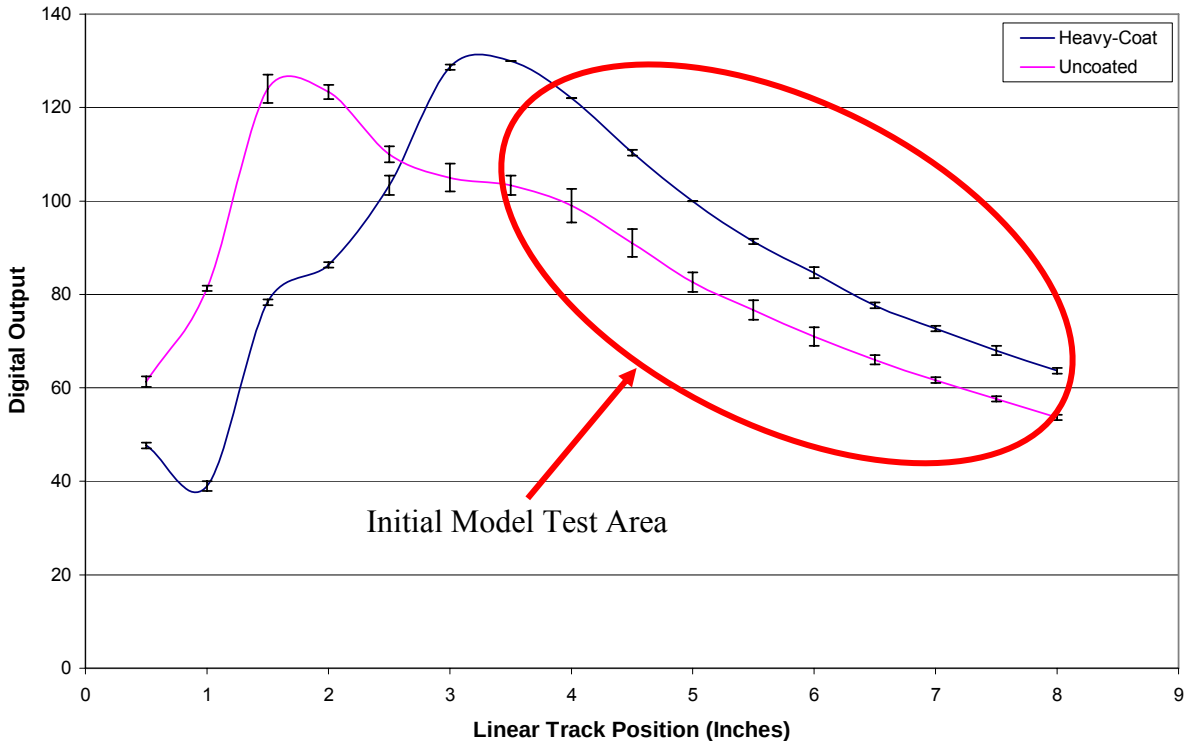

Figure 70: Data used in initial correlations with model circled in red.

The features exhibited by both the model and data are that the linear distance between the striking positions on the PSD remain fairly parallel between the coated and uncoated cases. The digital output of each data set also become smaller as the sensor is pulled away from the test coupon. Based on the model, the striking location on the PSD moves to the right with respect to Figure 67 for each case, coated and uncoated as the sensor moves further away from the test coupons. Using this logic, the digital output should decrease as the light striking location moves to the right on the PSD. The data

highlighted in Figure 70 support this model. However, the entire trend of data in Figure 55, Figure 57 and Figure 59 cannot be explained by this limited application of the model. As a seemingly un-related measurement of the IR projection onto the sample is made at linear track positions greater than three inches where the model predicts the data, a new discovery is made. The size of the IR projection onto the test coupon seems to become smaller at a distance greater than two to three inches. The IR projection spot size at a linear track position greater than two to three inches is 0.15 by 0.175 inches. When the sensor is less than two to three inches, the spot size increases. Data from Figure 55, Figure 57 and Figure 59 at a linear track position of two to three inches also corresponds to a crossover point in the data. Based on the model used to explain the data in Figure 70, the uncoated series yields lower values of digital output when compared to the coated series. However, the data at linear track positions less than two to three inches show that the uncoated series yields higher values of digital output when compared to the coated series in Figure 70. This means that a complete logic switch occurs at a linear track position between two and three inches. Since data about the sensor cannot be attained, a physical reason for this logic switch is explored by implementing the phenomena observed in Figure 71.

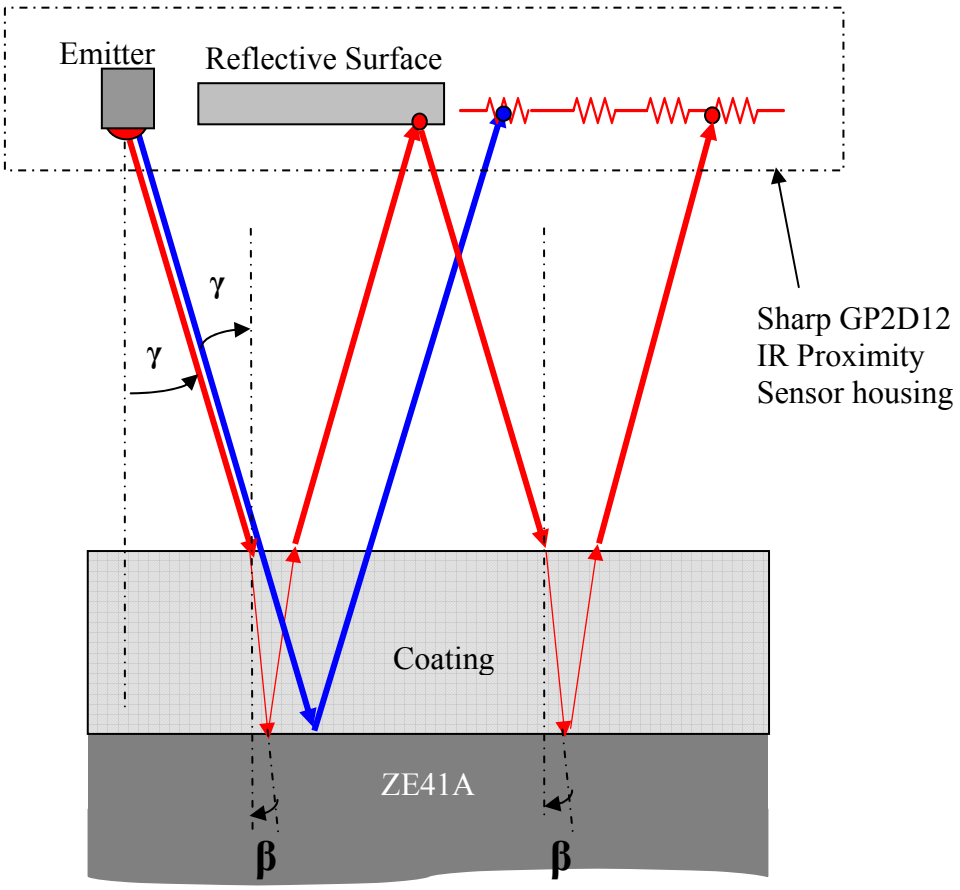

Figure 71: Illustration of light (red ray) refracting through the coating, reflecting off of a reflective surface at the sensor, refracting through the coating again and reflected back to the PSD.

Figure 71 shows a model representing possible light paths taken for the coated and uncoated IR proximity sensor measurements at a linear track position of less than two to three inches. The red ray represents the path taken by the light in the coated case. A reflective surface is included in this model on the IR sensor housing. In this model, the light ray is emitted from the emitting diode at angle γ and refracts through the coating at angle β. The light ray leaves the coating at the incident and refracted angles and strikes the surface of the reflective surface on the IR proximity sensor housing. The light then reflects back to the test coupon surface and refracts through the coating and returns to the

sensor at the PSD where it terminates. The blue light ray represents the light path in the uncoated surface. This light path only involves reflection off the ZE41A surface and return to the sensor at the PSD. In this model, the light ray that reflects off the uncoated surface is farther to the left and the light ray that refracts through the coated surface and reflects off the ZE41A and returns to the PSD is farther to the right. Is result is in direct contradiction to the model in Figure 68 in that the light reflecting off the ZE41A is further to the right on the PSD when compared to the refracted light through the coating. However, the model in Figure 71 does correlate well to the data in Figure 55, Figure 57 and Figure 59 for linear track positions less than two to three inches in that the uncoated digital output is greater than the coated samples digital output implying that the uncoated light ray is striking the PSD further to the left than the coated light ray. It should also be noted that the positions where the light ray in the coated and coated scenarios keep a relative constant distance between each other indicating that light paths remain fairly parallel. It should be noted that the distance between the positions at which the light strikes the PSD for each coating case at linear track positions less than two to three inches is not as linear in trend as the distance between the two light striking positions on the PSD for linear track positions greater than two to three inches. This occurs because the final position of light ray in the coated case depends on the first contact by light ray and the second contact point after reflection off the reflective surface from the IR proximity sensor housing. The point of contact on the PSD relative to the leftmost point of the PSD (x_r) for the light ray passing through the coating increases as a function of four times the light path distance (l_r) through the coating times the sine of β. The point of contact on the PSD relative to the leftmost point on the PSD (x_{ur}) for the light ray being reflected in the

uncoated surface increases two times the distance of the light path (l_{ur}) from the emitter to the ZE41A surface. Applying Snell's Law and the above statements, the following relationships are made.

$x_r = 4*l_r*\cos(\beta)$

$\beta = \theta_b$

$\theta_b = \sin^{-1}((n_a)/(n_b)\sin(\theta_a))$ – Snell's Law

$\theta_a = \gamma$ where γ is a manufactured angle in the Sharp GP2D12 IR proximity sensor

$x_{ur} = 2*l_{ur}*\sin(\gamma)$

Unknowns in these relations which can be found experimentally are n_b and θ_a. Once these two variables are determined, the relationships for x_r and x_{ur} are determined. X_r and x_{ur} can then be used to correlate a relationship between data in Figure 55, Figure 57 and Figure 59 to produce a mathematical relationship of digital output as a function of linear track position when the models in Figure 69 and Figure 71 are combined and applied to these relations. The philosophical difference between the two models is that the model represented in Figure 71 represents the light path for a linear track position of less than two to three inches and the model in Figure 68 represents the light path for coated and uncoated samples at linear track positions greater than two to three inches. Therefore, if the two models are combined, they correspond closely to the data.

Because the reflected light from the coated surface to the PSD is projected onto a distinctly different position on the PSD from the reflected light to the PSD in the uncoated surface, a distinct difference in data output is observed. This difference is not due to a difference in distance from the PSD to the coating or uncoated surface but due to a difference in the refractive index of air relative to the coating.

Fourier Transform Infrared Spectroscopy

Results

The results produced from the FTIR/ATR experiment are shown below.

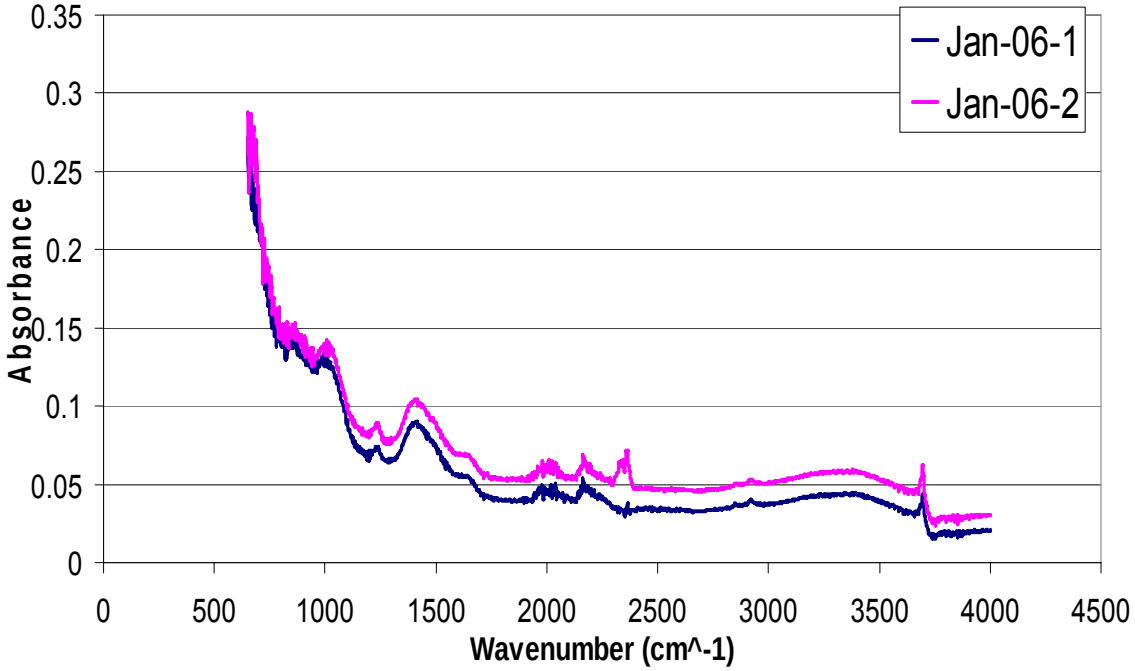

Figure 72: FTIR/ATR results for well coated magnesium alloy ZE41A recorded in January, 2006.

Discussion

These data are taken from a sample analyzed during January, 2006. They indicate that light is adsorbed at 3695 cm^{-1}. This could indicate magnesium hydroxide is present in the sample.[26] Magnesium hydroxide is a known component for in the coating therefore, the coating is indicated by the data.

Raman Spectroscopy

Results/Discussion

The results produced from the Raman experiment are shown for four different samples. The first sample is the sample used in the acquisition of the IR data shown in the previous section. The data from this sample are recorded in January, 2006 and in May, 2006. Initially, the data collected in January did not match the data collected in May, but different samples are used in each experiment. Therefore, more data is collected from January's sample in May to reaffirm that the data is consistent. One parameter is changed between January's collection and May's collection as a physical parameter of the instrument is changed, the objective used. In January, a 100X magnification objective is used and in May, a 50X lens magnification with a 0.55 numerical aperture is used. The 50X magnification data collected is indicated by the legend in the upper right hand corner of the data set in Figure 73. This data is noisier than the data collected with the 100X magnification objective because light from the atmosphere can interact with the sample more in the 50X case. On a separate experiment, Figure 73 shows the effect of using a 633 nanometer wavelength excitation for this same sample with a 50X lens magnification.

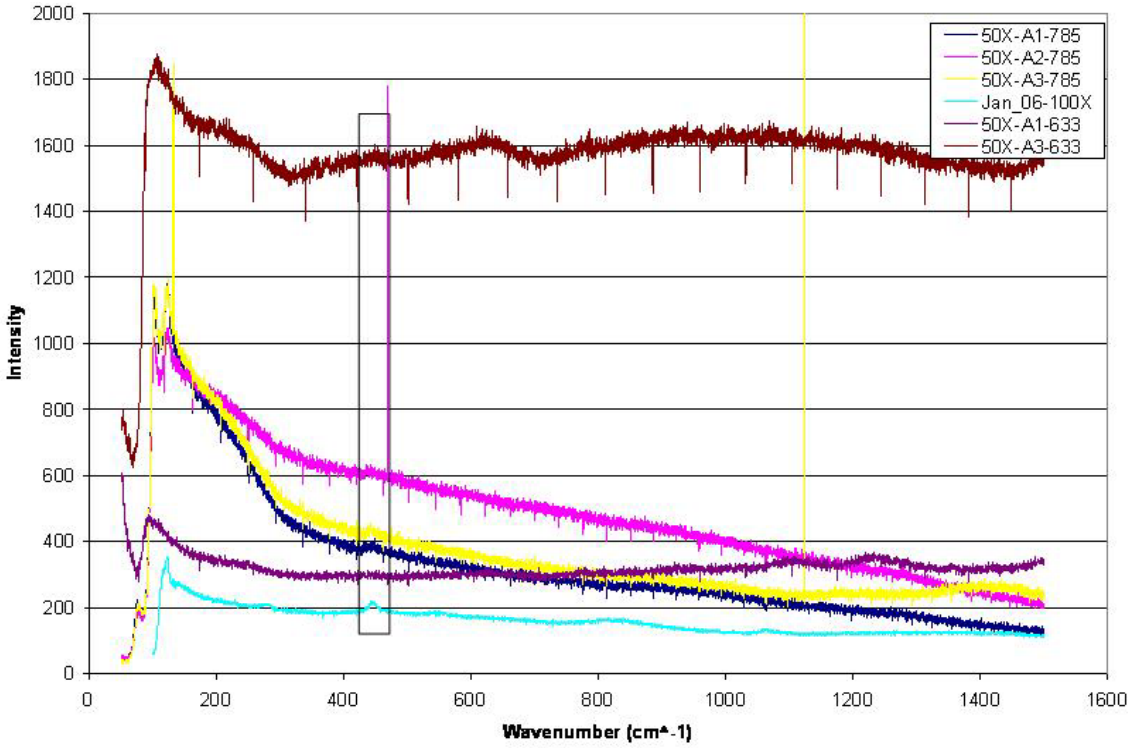

Figure 73: Raman spectra for well coated ZE41A sample recorded in January and in May 2006. Excitation frequencies of 633nm and 785nm are used.

The data collected in January, labeled, Jan_06-100X shows that there is a distinct shift at 444 cm^{-1} indicating a remote chance that magnesium oxide is possible at this area. Literature shows that magnesium oxide peaks have been observed at 441 cm^{-1}.[27] The data collected with the 50X objective also shows that peaks at 444 cm^{-1} are present but not as strongly as seen in the 100X objective data. This similarity between the 50X and 100X objective data is noted with a rectangular box as shown in Figure 73. Two of the three data sets gathered with the 633 nanometer excitation laser also show that a faint peak occurs at 444 cm^{-1}. This shows that the data for the well coated sample are consistent and can possibly be identified as magnesium oxide.

The next set of results is provided from the experiments conducted with the three samples used in each quality coverage evaluation method, heavily, partially and lightly

coated conditions with an excitation wavelength of 785 nanometers. The data is presented with charts that are separated by area and then by coating condition for ease of interpretation. The first series of data displayed is the data from area one on the heavily coated sample. This data shows that there are four possible distinct shifts at 1381 cm^{-1}, 1494 cm^{-1}, 1519 cm^{-1} and 1598 cm^{-1}. The peak closest to a published match with a possible component in the coating, magnesium carbonate is 1494 cm^{-1}. Magnesium carbonate is published at 1446 cm^{-1} so may not be the best possible match for this peak but is the closest found through literature research that matches a possible compound in the coating with published wavenumbers of these compounds.[28] The data for each location in area one on the heavily coated sample are summarized in Figure 74.

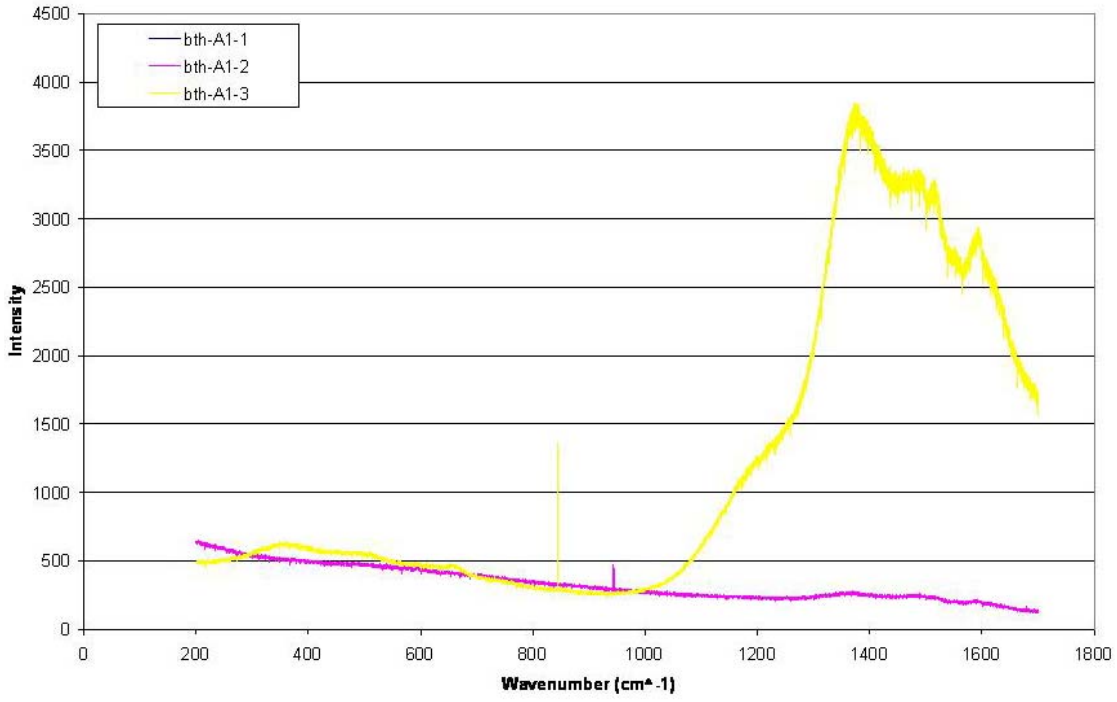

Figure 74: Raman spectra of the heavily coated ZE41A sample at area 1 as referenced in Figure 11.

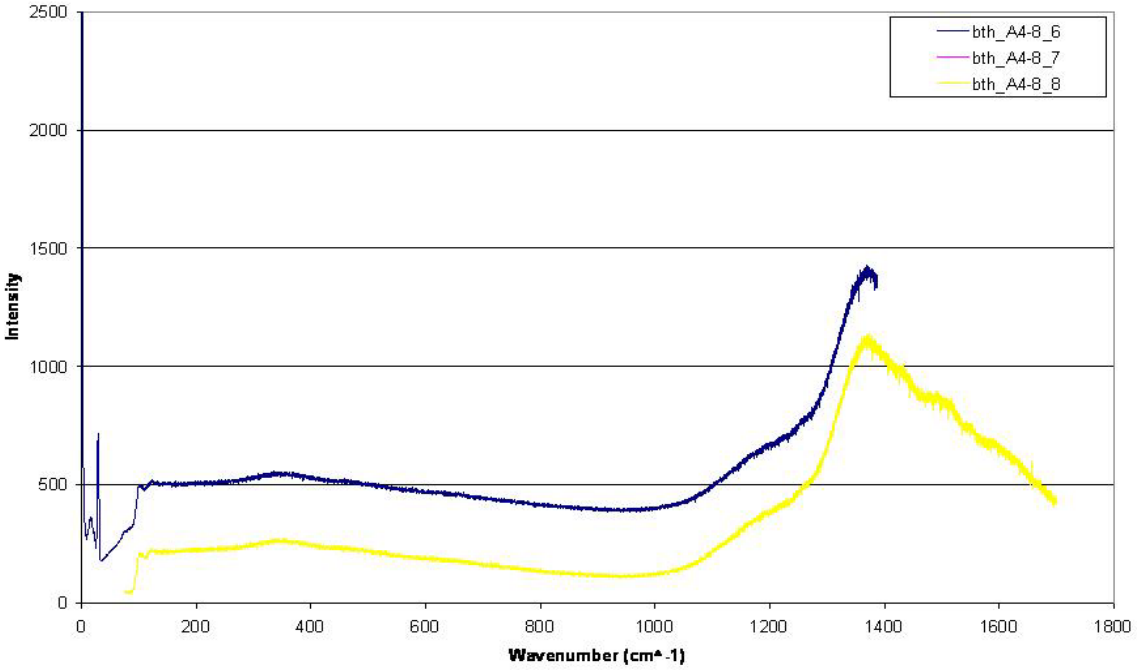

Figure 75: Raman spectra of the heavily coated sample shown in Figure 11 between areas 4 and 8.

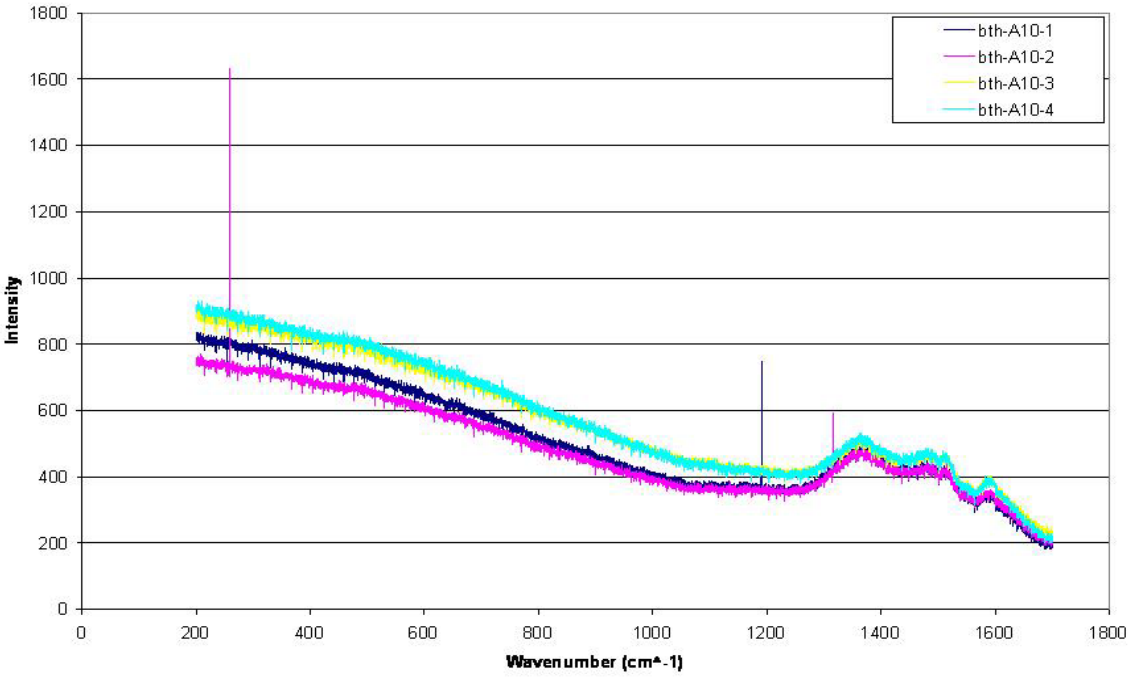

Figure 76: Raman spectra of heavily coated sample shown in Figure 11 for area 10.

The wavenumbers 1381 cm^{-1}, 1494 cm^{-1}, 1519 cm^{-1} and 1598 cm^{-1} are a common thread between each spectra from each area on the heavily coated sample. The intensities of these shifts are also approximately in the same interval.

The next set of results corresponds to different areas sampled on the partially coated sample. These samples are excited with a 785 nanometer wavelength laser through a 50X lens magnification. The results shown in Figure 77 show that a distinct shift lays at 1381 cm^{-1} but saturates the detector in two of the five data points. The detector is known to be saturated when the signal received by the detector is so intense that it cannot resolve data above an intensity of 60,000. Saturation of the detector is not observed in the heavily coated sample. Another difference between this sample and the heavily coated sample is that the partially peaks at 1494 cm^{-1}, 1519 cm^{-1} and 1598 cm^{-1} are not clearly resolved in this data set. An additional peak not seen in the heavily coated data is observed at 385 cm^{-1}.

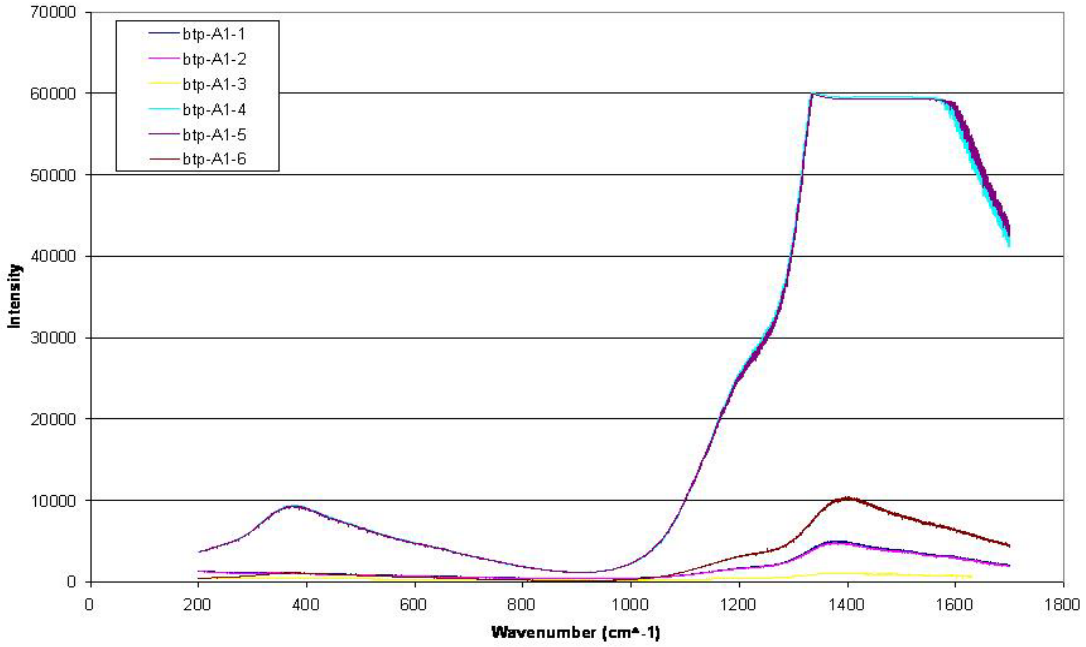

Figure 77: Raman spectra of partially coated sample shown in Figure 12 at area 1.

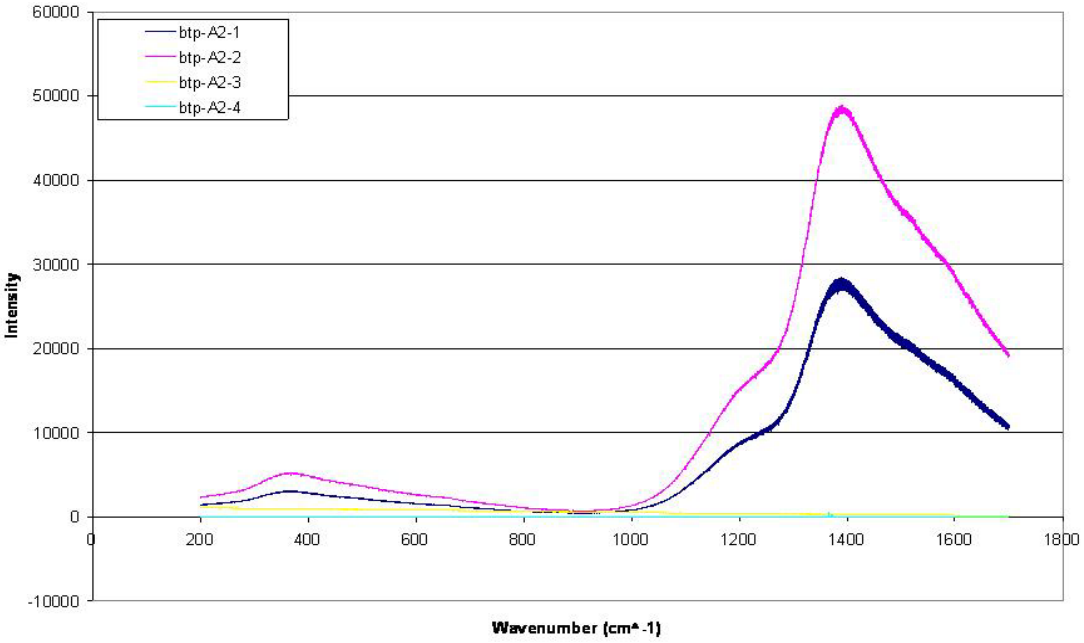

Figure 78: Raman spectra of partially coated ZE41A sample shown in Figure 12 for area 2.

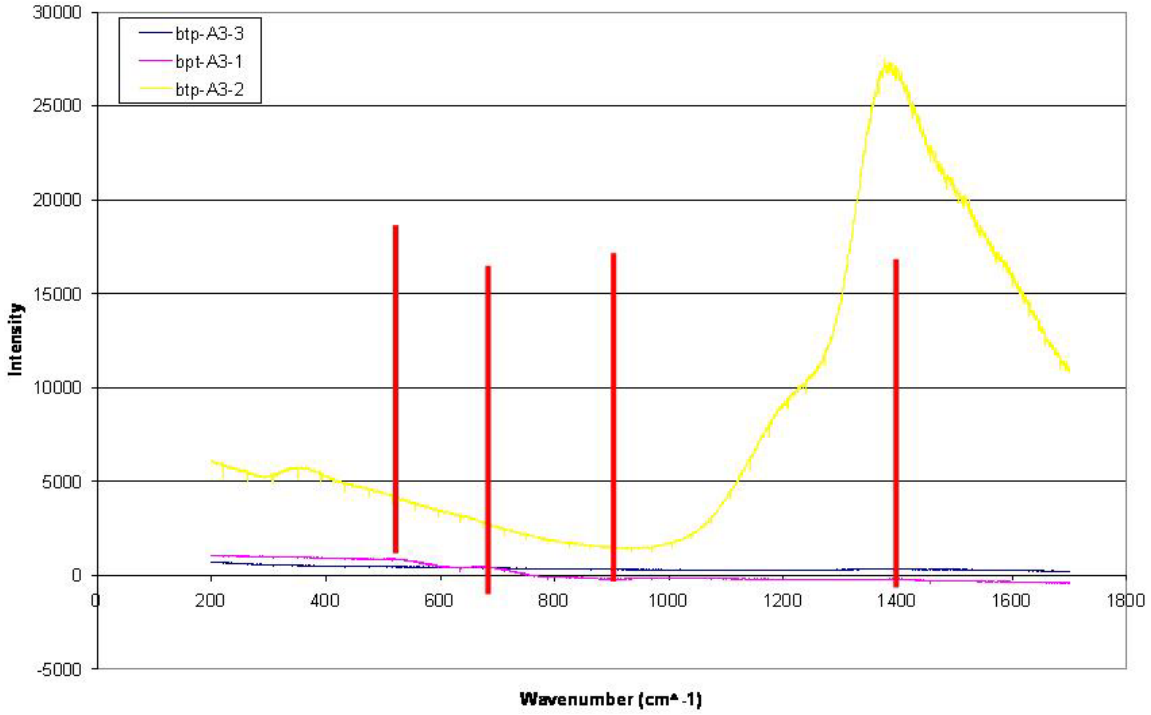

Figure 79: Raman spectra for the lightly coated ZE41A sample shown in Figure 12 for area 3.

The results shown for areas two and three in Figure 78 and Figure 79 also indicate that there could be a very strong shift at 1381 cm^{-1} and 385 cm^{-1}. It is also important to note that when the shift at 1381 cm^{-1} has a relatively strong intensity, the shift at 385 cm^{-1} is also relatively notable in intensity indicating that these two shifts are characteristic of the compound being activated.

The next set of data shown in Figure 80 corresponds to the lightly coated sample at area 1. This data shows that there is a notable shift at 1381 cm^{-1}. The intensity of this shift is in the same range of intensity as shifts seen in the heavily coated sample. One of the locations in this area also shows that a shift at 385 cm^{-1} is notably present.

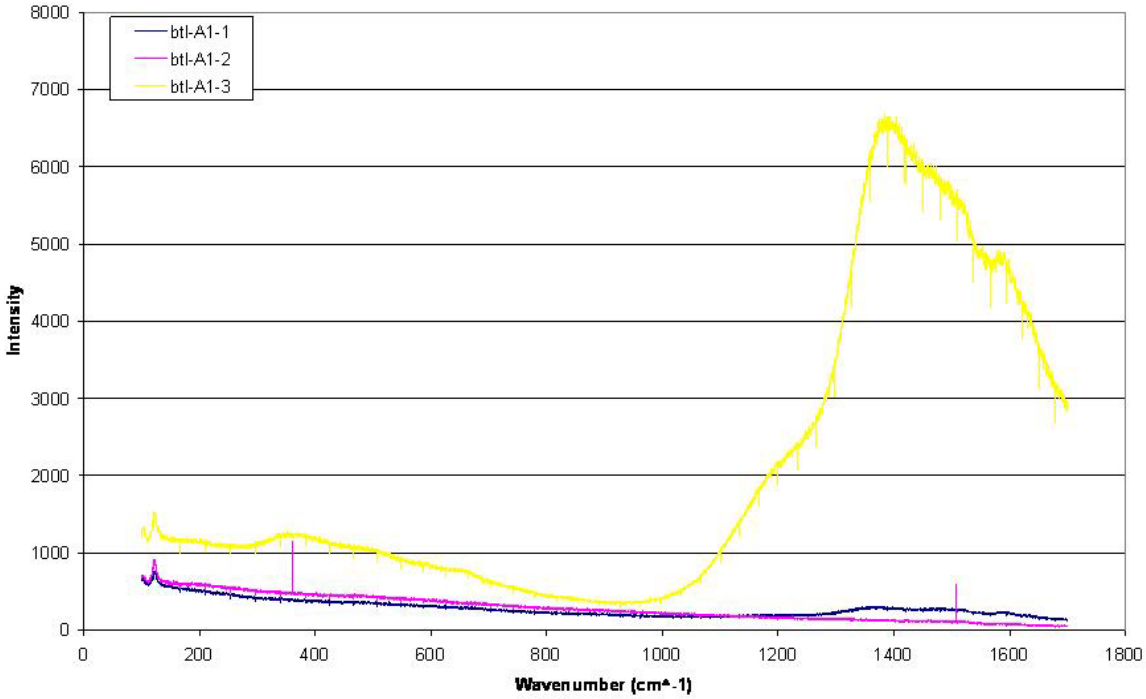

Figure 80: Raman spectra for the lightly coated ZE41A sample shown in Figure 13 at area 1.

The data shown in Figure 81 corresponding to area three on the lightly coated sample do not show a strong correlation to a majority of the data seen in the heavily, partially and other lightly coated data. However, there is one location within area three that does show a small shift at 1381 cm^{-1}. The intensity is also relatively small and in the same order as some shifts observed in the heavily, partially and lightly coated sample data.

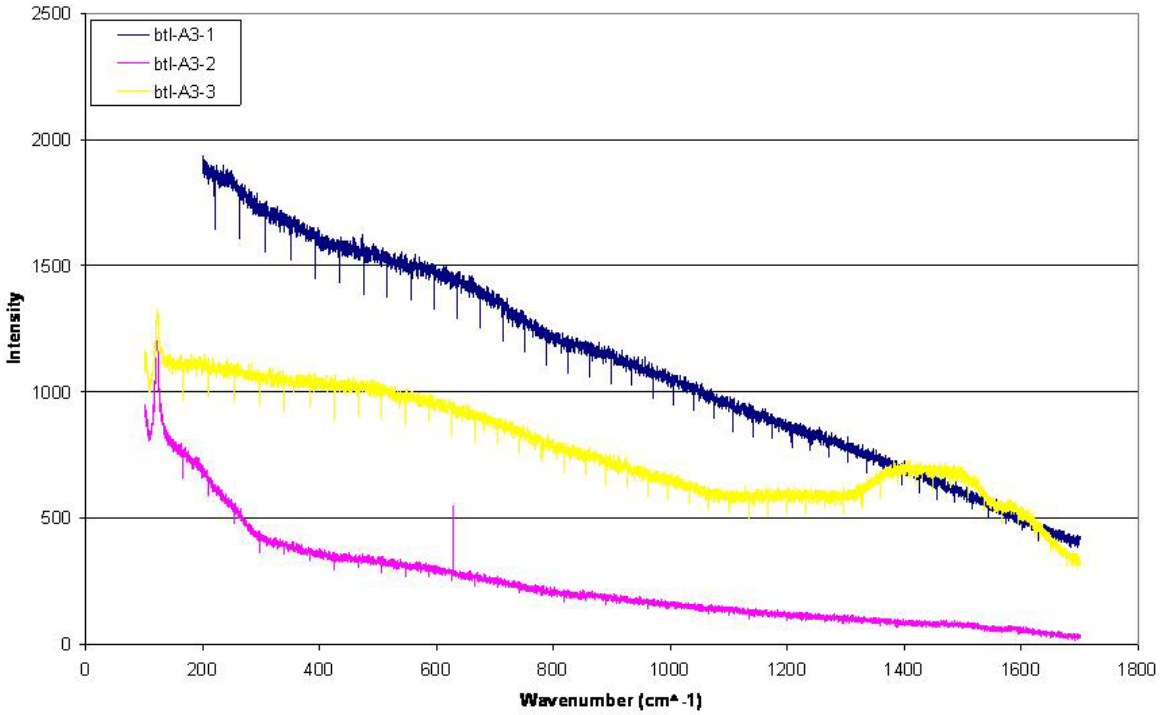

Figure 81: Raman spectra for the lightly coated sample of ZE41A shown in Figure 13 at area 3.

The data shown in Figure 82 corresponds to various locations in area 7 on the lightly coated sample. The shifts are strongly present at 385 cm^{-1} and 1381 cm^{-1}. It should also be noted that two the shifts observed at 1381 cm^{-1} saturate the detector meaning that the molecule causing this shift is strongly related to the shift seen at this wavenumber.

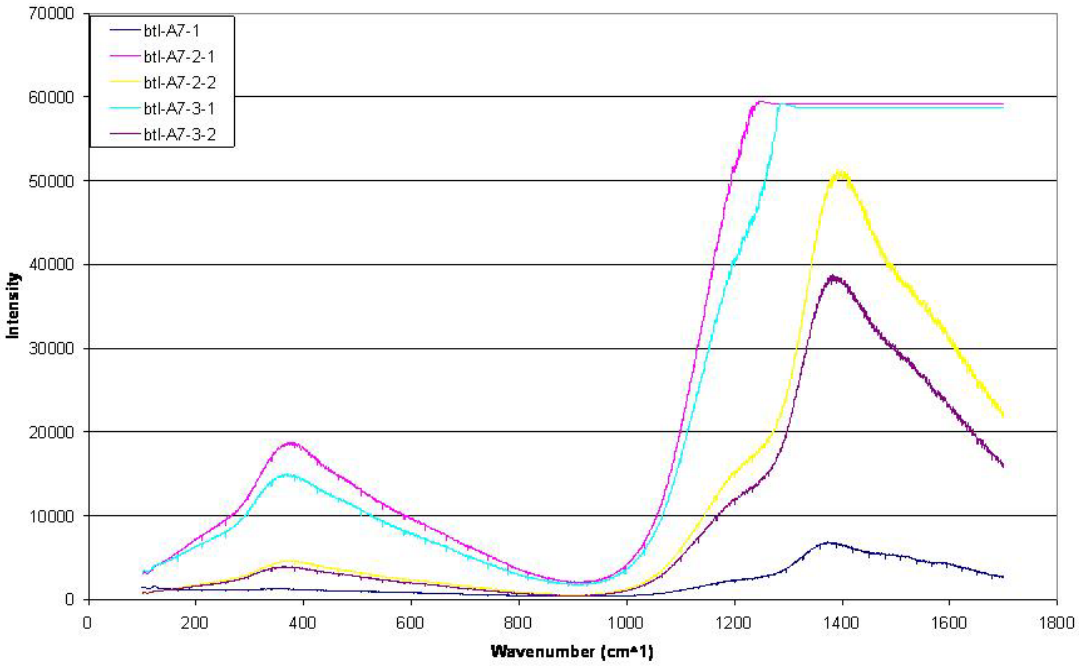

Figure 82: Raman spectra for the lightly coated ZE41A sample shown in Figure 13 at area 7.

Polarized Light Microscopy

Results/Discussion

The results from the polarized light microscopy experiment showed that there is a distinct difference between the image acquired with a linearly polarized filter in the vertical position and the sample rotated forty five degrees relative to the vertical position with regards to grey count value. This data is summarized in Figure 83.

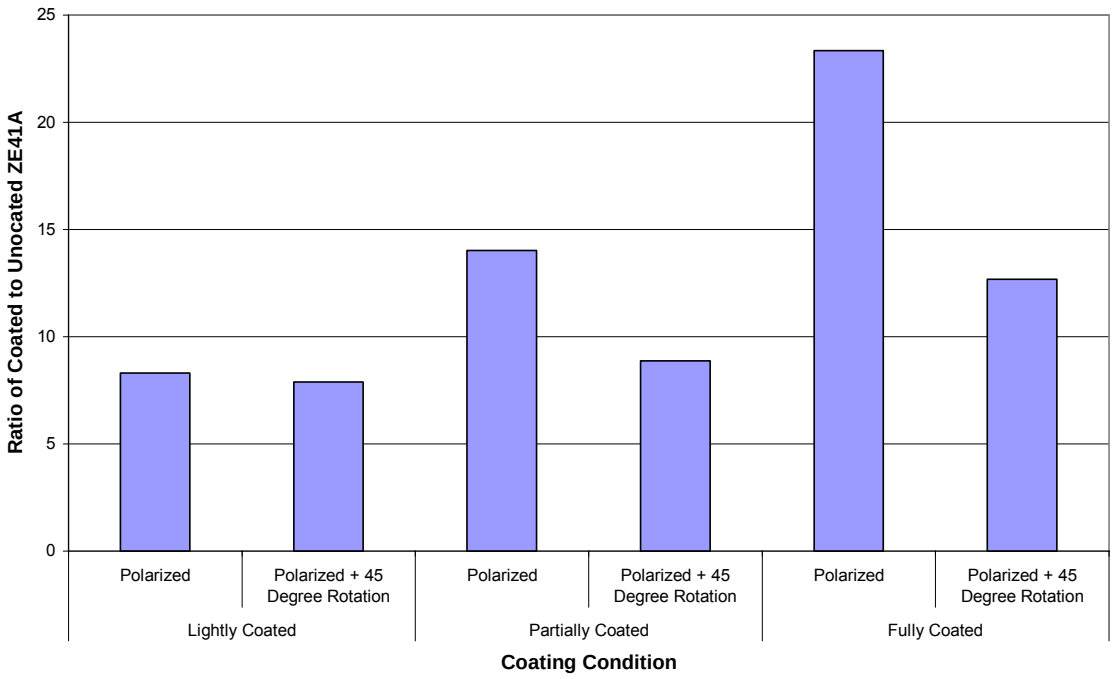

Figure 83: The ratio of mean grey count value calculated using imageJ for each coated sample to an uncoated sample in a vertical and forty five degree rotation of the sample with respect to the polarizing filter.

An ancillary observation shows that there is a distinct difference between the three different sample coating conditions, lightly, partially and heavily coated are distinguishable from one another using linearly polarized light in the vertical position. No rotation is necessary to distinguish a lightly coated sample from a heavily coated sample. These distinctions are clear both visually and quantitatively through grey count counting using imageJ. Randomly chosen images for each sample are shown below in Figure 84, Figure 85 and Figure 86.

2.5 X Magnification: 0°

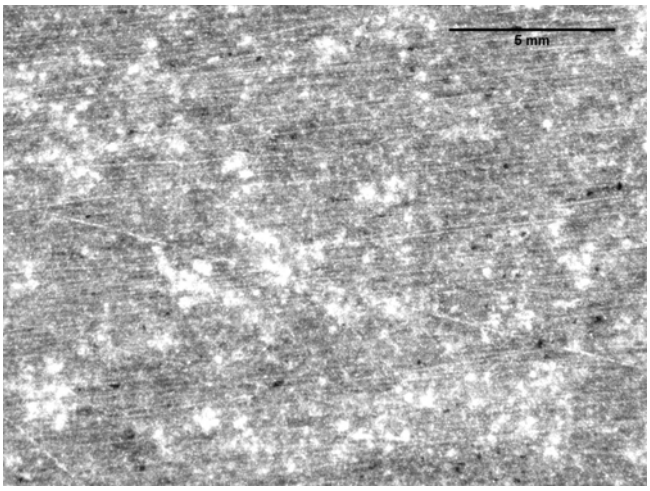

45° Rotation

2.5 X Magnification: 45°

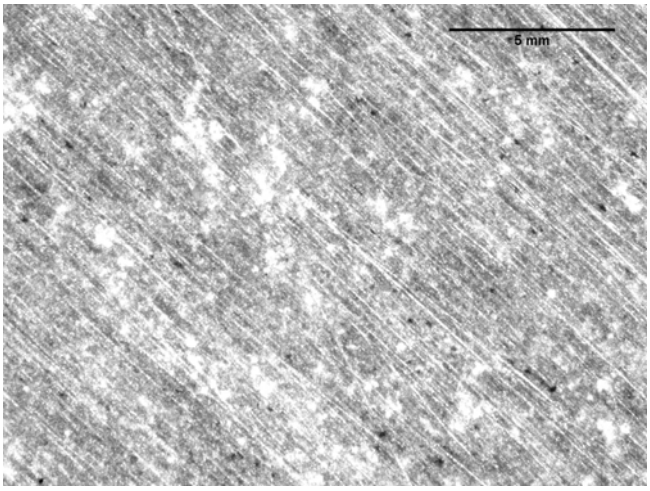

Figure 84: Heavily coated sample under linearly polarized light at 2.5X lens magnification and 0.075 NA. A calibrated scale is included in the upper right hand corner of the image.

2.5 X Magnification: 0°

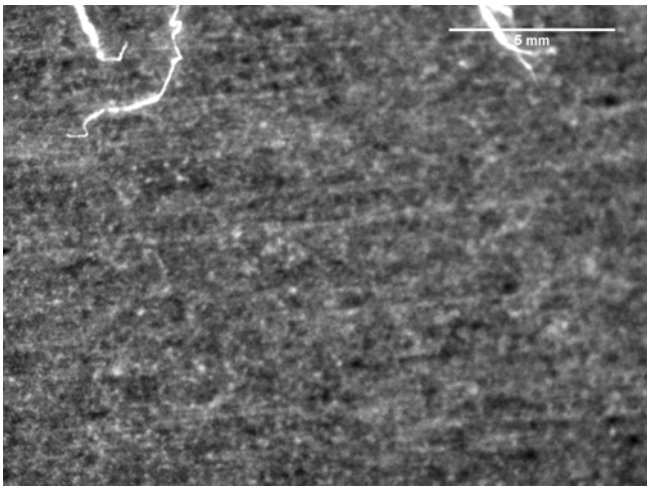

45° Rotation

2.5 X Magnification: 45°

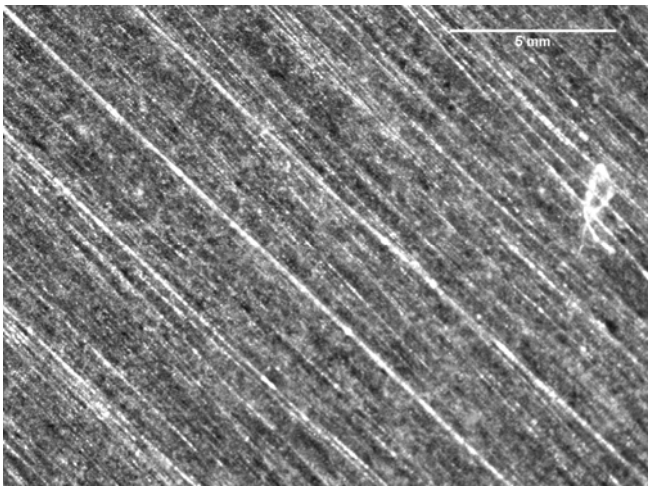

Figure 85: Partially coated sample under linearly polarized light at 2.5X lens magnification and 0.075 NA. A calibrated scale is included in the upper right hand corner of the image.

2.5 X Magnification: 0°

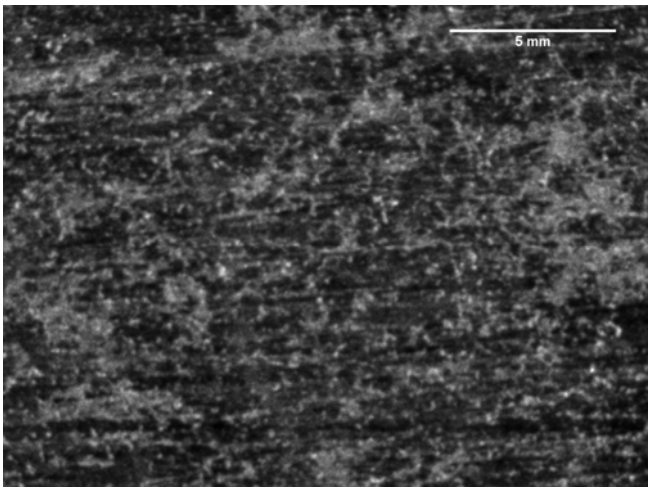

45° Rotation

2.5 X Magnification: 45°

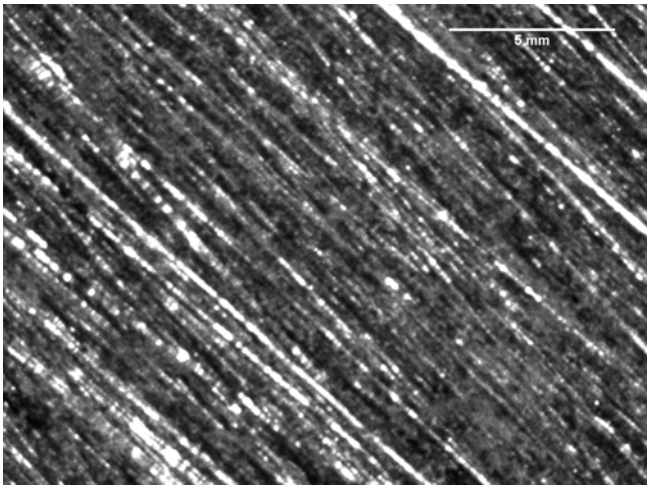

Figure 86: Lightly coated sample under linearly polarized light at 2.5X lens magnification and 0.075 NA. A calibrated scale is included in the upper right hand corner of the image.

CONCLUSIONS

Thickness versus Coverage

The governing set of requirements, MIL-HDBK-693A used when designing with magnesium alloys does not specifically state that a specific coating thickness is required for conversion coatings on magnesium alloys. However, this standard does state that the conversion coating coverage is of paramount importance to ensure that the coating protection scheme for the magnesium alloys is maintained. Because coating coverage is most important in ensuring that the coating protection system is not breached, then nondestructive evaluation techniques determining coverage quality is the area of focus for this research.

Infrared Proximity Sensor

The Sharp GP2D12 IR proximity sensor does detect a difference between an environmentally friendly coated and uncoated ZE41A surface. Different coating conditions, lightly, partially and heavily coated ZE41A surfaces are also distinguishable from one another. The physical phenomenon detected by the sensor can possibly be attributed to the change in refractive index between coated and uncoated conditions and not the change in distance from the sensor to the coated and uncoated ZE41A surface.

Fourier Transform Infrared Spectroscopy

The FTIR data acquired in the ATR mode helps to give a fingerprint that distinguishes a coated surface from an uncoated surface because of specific Raman bands identified in the data presented. This gives the coating a specific signature that can be

detected on any surface. However, equipment used to perform this task is sensitive and costly. Therefore, simpler field versions must be developed for this purpose.

Raman Spectroscopy

Raman spectroscopy data show that a distinct signature of the coating can be measured. Chemical species in the data correspond to chemical species that are included in the preparation and treatment processes involved with the coating process. Therefore, Raman spectroscopy is a reliable method that can be used to determine if a coating is present on the surface of a ZE41A sample. However, the instrumentation used to collect this data is costly and sensitive to ambient conditions. The information delivered by this instrument is also much greater than the information needed for this application.

Polarized Light Microscopy

Polarized light microscopy in conjunction with image processing software such as imageJ provide results that show a difference between environmentally friendly coated and uncoated samples of ZE41A using mean gray count values from a 10 bit image. This method even shows a distinct difference between lightly, partially and fully coated ZE41A samples and is easily employed in the field with the use of proven technology.

FUTURE WORK

Infrared Proximity Sensor NDE

Future development of the Sharp GP2D12 IR proximity sensor involves the collection of more data over flat and curved surfaces. More data must also be collected at smaller linear track position intervals so that a more accurate model can be developed. This particular sensor may not be the solution that should be employed but using an infrared emitter and a PSD with more controlled experiments should be continued so that an optimal method using this technique can be developed.

Packaging should be developed for such a device so that the distance from the part being examined and the emitter, PSD setup is held at a constant optimal distance when measurements are taken. The sensor should also include an on board power source and packaged microcontroller so that it can be made into a mobile device.

System Development for FTIR NDE

More data must be collected on the FTIR and compared to published literature so specific chemical information can be matched with chemical species that are known to exist in the coating or ZE41A. More research in already existing field portable FTIR units must be conducted to determine the modifications that are necessary for application to this particular coating and substrate.

System Development for Raman NDE

More data must be collected on the Raman spectroscope so that known chemical information on the coating or ZE41A can be compared more closely with published

literature. More research must also be conducted in the use and existence of portable Raman spectroscope instruments. The research must show the feasibility of integration of existing hardware for this field application.

System Development for Polarized Light Microscopy NDE

More data for curved surfaces must be taken for the polarized light microscopy method. Components in service with non-machined surfaces or sand cast surfaces must be examined so more data can be correlated between these coated and uncoated forms of ZE41A. Hardware to implement a handheld field unit must also be selected and tested for prototype development.

REFERENCES

[1] U. S. Public Health Services, Toxicological Profile for Chromium, Agency for Toxic Substances, Report No. ASTDR/TP-88/10 (1989).

[2] Sikorsky, in *Jane's All the World's Aircraft* (Jane's, Alexandria. VA, 2004-2005 p. 762-769.

[3] Department of Defense, Military Specification: Environmental Engineering Considerations and Laboratory Tests, Report No. MIL-STD-810F (Washington. DC, 2003).

[4] Department of Defense, HH-65A, Report No. CGTO 1H-65A-2-1 (Washington, DC. 2006).

[5] H. B. Michael, A. Avedesian, *ASM Specialty Handbook - Magnesium and Magnesium Alloys* (ASM International, Materials Park, OH, 1999).

[6] *K.U. Kanier, ed.Magnesium - Alloys and Technologies*; (Wiley-VCH, Geesthacht, Germany, 2003).

[7] Japan Steel Works LTD. http://www.jsw.co.jp/en/mg_f/mg_mg_f/mg_mg_chare.htm, (last accessed February 7, 2006).

[8] R. S. Busk, *Magnesium Products Design* (Mercel Dekker, Inc, New York, 1987).

[9] *L. A. Abel, R. T. Kiepura, P. Thomas, H. F. Lampman, N. D. Wheaton. eds. Metals Handbook - Tenth Edition - Properties and Selection: Nonferrous Alloys and Special Purpose Materials*; *Vol. 2* (ASM International, USA, 1990).

[10] *J. H. Johnson, R. T. Kiepura, D. A. Humphries. eds. ASM Handbook - Corrosion: Formerly Ninth Edition, Metals Handbook*; *Vol. 13*, (ASM International, USA, 2001).

[11] D. A. Jones, *Principles and Prevention of Corrosion*, 2nd ed. (Prentice Hall, Englewood Cliffs, NJ, 1996).

[12] J. D. Hanawalt, C.E. Nelson, J.A. Peloubet, in *Corrosion Studies of Magnesium and Its Alloys*, (American Institute of Mining and Metallurgical Engineers, Philadelphia, PA, 1941).

[13] Department of Defense, Military Specification: Magnesium Alloy, Processes for Pretreatment and Prevention of Corrosion on Magnesium Alloys, Report No. MIL-M-3171C (Washington, DC, 1998).

[14] Department of Defense, Military Specification: Coating, Aliphatic Polyurethane, Chemical Agent Resistant, Report No. MIL-C-46168D.

[15] R. B. Griffin, J. Cunningham, R. Kestler, V. Lin, C. Matzdorf, et al. Joint Test Protocol and Fatigue Test Plan, Report No. 050211 (Corpus Christi Army Depot Internal Documentation, Corpus Christi, TX, 2004).

[16] R. B. Griffin, D. Zuniga, C. Bollfrass, O. Dibua, M. Ijaz, Corrosion of Rotor Gear Box Housings, (Texas A&M University - Academic Center for Aging Aircraft Report, College Station, TX, 2006).

[17] Department of Defense, MIL-HDBK-693A: Magnesium and Magnesium Alloys, Report No. MIL-HDBK-693A (Washington, DC, 1998).

[18] D. J. Hagemaier, *Fundamentals of Eddy Current Measurement* (The American Society for Nondestructive Testing, Columbus, OH, 1990).

[19] R. French, personal communication, Sharp Electronics, Camas, WA (2006).

[20] D. W. Mayo, F. A. Miller, R. W. Hannah, *Course Notes on the Interpretation of Infrared and Raman Spectra* (John Wiley & Sons, Hoboken, 2004).

[21] ROI Importer Plugin for imageJ, http://rsb.info.nih.gov/ij/plugins/path-writer.html, (W. Rasband, 2004).

[22] R. B. Emmons, Solid-State Electronics **10,** 505-506 (1967).

[23] PIC16F87X Data Sheet (Microchip Technology, Chandler, AZ, 2001).

[24] Sharp GP2D12 Infrared Proximity Sensor Data Sheet (Sharp Electronics, Mahwah, NJ, 2006).

[25] X. P. V. Maldague, *Theory and Practice of Infrared Technology for Nondestructive Testing* (John Wiley & Sons, New York, 2001).

[26] R. O. Kagel, R. A. Nyquist, *Handbook of Infrared and Raman Spectra of Inorganic Compounds and Organic Salts*, Vol. 4 (Academic Press, Inc., San Diego, 1971).

[27] S.C. Chang, M. A. Luegers, S. R. Bare, The Journal of Physical Chemistry **96** (1992).

[28] H. N. Rutt, J. H. Nicola, Journal of Physics C: Solid State Physics **7** (1974).

VITA

David Zuniga was raised in Pecos, Texas where he graduated from Pecos High School. He enrolled Texas A&M University in the Department of Mechanical Engineering and received his Bachelor of Science in Mechanical Engineering in May, 2002. Upon completion of his degree, he worked with Lockheed Martin Aeronautics Company in Marietta, Georgia for approximately a year and a half and left the company to pursue an interest in biomedical applications of mechanical engineering with a team of medical physicists at MD Anderson Cancer Center in Houston, Texas.

David Zuniga
1508 Cowan
Pecos, TX 79772